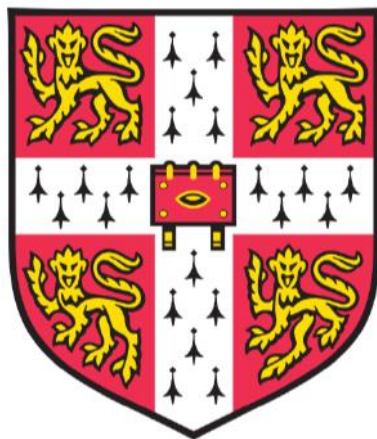


# Quantum-confined Inorganic-organic Lead Halide Perovskite



Xinyu Bai

Department of Physics  
University of Cambridge

*A dissertation submitted for the degree of  
Doctor of Philosophy*



*For Fengxiang Li and Handong Bai*



## DECLARATION

This dissertation is the result of my own work and includes nothing which is the outcome of work done in collaboration except as specified in the text. It is not substantially the same as any that I have submitted, or, is being concurrently submitted for a degree or diploma or other qualification at the University of Cambridge or any other University or similar institution except as specified in the text. I further state that no substantial part of my dissertation has already been submitted, or, is being concurrently submitted for any such degree, diploma or other qualification at the University of Cambridge or any other University or similar institution except as specified in the text. This thesis is does not exceed 60000 words.

Xinyu Bai



# Abstract

Title: Quantum-confined Inorganic-organic Lead Halide Perovskite

Name: Xinyu Bai

Inorganic-organic hybrid perovskites have been regarded as one of the most distinctive next-generation luminescence materials due to their advanced properties. This thesis describes our study of confining inorganic-organic hybrid perovskites with nanoporous gallium nitride (GaN) matrix and with polyaromatic hydrocarbon compounds.

We demonstrate a solution-processed method for infiltrating methylammonium lead bromide perovskite ( $\text{MAPbBr}_3$ ) into the nanoporous GaN matrix. The GaN matrix prevents perovskite from light-induced degradation for five hours in the ambient atmosphere. Besides, the porous GaN also protect perovskite from degradation after one year of exposure to the ambient atmosphere. We then investigate the confinement effect of the nanoporous GaN on  $\text{MAPbBr}_3$  perovskite via transient photoluminescence and transient absorption characterisation. The spatial confinement leads to enhanced charge carrier interaction, revealed as a blue shift in photoluminescence and a higher radiative recombination rate for  $\text{MAPbBr}_3$  perovskite inside nanopores. The enhanced charge carrier interaction also results in a larger electron-hole binding energy. As a result, the dominant radiative recombination process in  $\text{MAPbBr}_3$  nanocrystals at room temperature is the exciton recombination. Considering the solution-processed synthesis method, the remarkable stability in the ambient environment and the promising light-emitting performance, we propose that the perovskite/GaN matrix could offer a route

to producing composites of interest for use in optoelectronic devices for various applications.

Additional, we demonstrate a solution-processed method to synthesis two-dimensional (2D) perovskite thin films with 2,6-dimethylammoniumnaphthalene (DMAN) and bis(propargyl ammonium iodide) anthracene (BPAIA), respectively. We successfully synthesized DMAN lead iodide perovskite and BPAIA lead iodide perovskite. However, the characterisation demonstrates that the synthesized BPAIA perovskite is not pure. Molecular modelling suggests a large repulsion between BPAIA molecules exists in the organic spacer layer of the 2D perovskite, resulting in the photoluminescence broadening. The DMAN lead iodide perovskite shows a structural character of the Dion-Jacobson perovskite and has an excitonic character, making it a candidate for lighting applications

# Acknowledgements

I am extremely grateful to all the amazing people who made my PhD journey in Cambridge exciting and memorable.

I am sincerely thankful to my supervisors, Prof. Richard Friend and Dr Dan Credgington, for allowing me to join this journey and for their continual support, guidance, resources, feedback, patience, and encouragement throughout my PhD.

Thank you so much for sharing your valuable experience and knowledge with me generously. I am particularly grateful to Dr Sam Stranks for being an extremely warm-hearted and helpful advisor. I am very thankful to Prof. Alex Webb, my college tutor, for his support, encouragement, and advice during my most challenging time in Cambridge.

I am fortunate to collaborate with many brilliant people during my PhD. I would like to thank Prof. John Anthony and his group at the University of Kentucky for synthesizing impressive new materials for me. I would like to thank Prof. Rachel Oliver and her group at the University of Cambridge for generously supplying gallium nitride samples and for all the inspiring discussions we had. I would like to thank Dr Sian Dutton for all her suggestions and advice.

I am deeply grateful to members of the Optoelectronics group. Thank you so much to all of you for being so generous and helpful throughout my exciting PhD journey. I am hugely grateful to Dr Miguel Anaya, Dr Florian Auras, Dr Linsong Cui, Dr Krzysztof Galkowski, Dr Sanyang Han, Dr Mengxia Liu, Dr David Palecek, Dr Amita

Ummadisingu, and Dr Zhilong Zhang for lending me your time, effort and expertise. I would like to thank my co-workers Alan Bowman, Yu-Hsien Chiang, Bluebell Drummond, Jiale Feng, Qinying Gu, Kangyu Ji, and Darcy Unson for their support. I am particularly grateful to Linjie Dai for all the discussion and quarrelling about science and life throughout the four years. My research would not have been so smooth without you, but my life would definitely be much easier. Thank you so much for helping me look for my samples in rubbish bins at midnight in the lab.

I would like to thank Richard Gymer, Roger Beadle, Alex Crook, Zina, Jennie Nelson, William Mortimer, Egle Bunkuteand and all the other members from the Kapitza Hub during these years. I could not imagine how messy my life would be without your support in the group.

I am very grateful to the China Scholarship Council and the Cambridge Trust for the funding to support me to complete my PhD.

I would like to thank all my friends in the Optoelectronics group, Churchill College, Cambridge and China, for your firm support and encouragement during my PhD. Thank you so much for all the pleasure we enjoyed together, and for being there through all the highs and lows of life. I will cherish all the laughs and tears we had together forever. Finally, I would like to express my sincere gratitude to my family. Thank you so much for your unconditional love and constant support. Thank you so much, Mom and Dad, for everything. Without the courage and strength you give me, I would never make it so far.

# Content

Chapter 1	Introduction.....	1
Chapter 2	Background.....	5
2.1	Semiconductor Photophysics .....	7
2.1.1	Origin of the Bandgap.....	7
2.1.2	Interaction of Light with Semiconductor.....	11
2.1.3	Thermalisation and Recombination Process.....	14
2.1.4	Charge Carriers .....	21
2.1.5	Quantum Wells.....	24
2.2	Inorganic Organic Lead Halide Perovskite .....	29
2.2.1	History of Perovskite .....	29
2.2.2	Structure of Organic-inorganic Metal Halide Perovskite .....	30
2.2.3	Properties of Perovskites.....	31
2.2.4	Two-dimensional Perovskites .....	32
2.2.5	Perovskite nanocrystals.....	36
2.2.6	Moisture Stability of Metal Halide Perovskites.....	42
2.2.7	Photobrightening and Photodarkening in Lead Halide Perovskites	44
2.3	Gallium Nitride.....	46
2.3.1	Properties of Gallium Nitride (GaN) .....	46
2.3.2	Forming Nanoporous GaN.....	47
2.3.3	Yellow band emission of GaN .....	48
Chapter 3	Experimental Methods .....	51

3.1	Sample Preparation.....	53
3.1.1	Chemicals.....	53
3.1.2	Infiltration of MAPbBr <sub>3</sub> Perovskite into Porous GaN.....	53
3.1.3	Preparation of MAPbBr <sub>3</sub> Thin Film.....	55
3.1.4	Preparation of Bis(propargyl ammonium iodide) anthracene (BPAIA) Lead Iodide 2D Perovskite.....	56
3.1.5	Preparation of 2,6-dimethylammoniumnaphthalene (DMAN) Lead Iodide 2D Perovskite.....	56
3.1.6	Sample Encapsulation.....	57
3.2	Structural and Morphology Characterisation .....	57
3.2.1	X-ray diffraction (XRD) .....	57
3.2.2	Scanning electron microscope (SEM) .....	59
3.3	Spectroscopy .....	60
3.3.1	Steady-state absorption .....	60
3.3.2	Steady-state photoluminescence (PL).....	60
3.3.3	Photoluminescence quantum efficiency (PLQE).....	61
3.3.4	Hyperspectra microscopy.....	63
3.3.5	Time-resolved Photoluminescence Spectroscopy.....	63
3.3.6	Transient Absorption (TA).....	67
3.3.7	Microscope TCSPC .....	69
Chapter 4	Infiltration of Perovskite into Nanoporous Gallium Nitride.....	71
4.1	Background and Motivation.....	73
4.2	Results and Discussion.....	75

4.2.1	Morphology of the Nanoporous GaN Matrix .....	75
4.2.2	Optical Properties of the Nanoporous GaN Matrix .....	78
4.2.3	Infiltration of MAPbBr <sub>3</sub> into Nanoporous GaN.....	87
4.2.4	Elemental Study of the MAPbBr <sub>3</sub> /GaN system.....	88
4.2.5	Infiltration of MAPbBr <sub>3</sub> into the Nanoporous GaN with APTES Treatment .....	93
4.2.6	Estimation of the Infiltration Degree of MAPbBr <sub>3</sub> in the 8 V etched Nanoporous GaN .....	96
4.2.7	Protective Effect of the Nanoporous GaN on MAPbBr <sub>3</sub> .....	99
4.3	Conclusion and Future Work.....	104
Chapter 5 Confinement Effect of the Nanoporous GaN on Methylammonium Lead Bromide Perovskite.....		107
5.1.1	Background and Motivation .....	109
5.2	Results and Discussion.....	111
5.2.1	MAPbBr <sub>3</sub> /GaN Sample Preparation .....	111
5.2.2	Templating Effect of Nanoporous GaN on MAPbBr <sub>3</sub> Perovskite .	112
5.2.3	MAPbBr <sub>3</sub> Nanocrystals Size Distribution in Nanoporous GaN ....	117
5.2.4	Charge carriers recombination in MAPbBr <sub>3</sub> in 8 V etched GaN...	127
5.3	Conclusion and Future Work.....	135
Chapter 6 Synthesis of Two-dimensional Perovskite with Polyaromatic Hydrocarbon Compounds .....		137
6.1.1	Background and Motivation .....	138
6.2	Results and Discussion.....	141
6.2.1	Properties of Bis(propargyl ammonium iodide) anthracene (BPAIA)	

6.2.2	Structural Study of the Synthesized Mixture .....	143
6.2.3	Optical Properties of the Synthesized Mixture .....	144
6.2.4	Morphology of the Synthesized Mixture .....	148
6.2.5	Local photoluminescence of the Synthesized Mixture .....	151
6.2.6	Force-field Modelling of the BPAIA 2D Perovskite.....	153
6.2.7	Synthesis of 2D DJ Phase Perovskite with 2,6-dimethylammoniumnaphthalene (DMAN).....	155
6.2.8	Structural Study of the 2D (DMAN)PbI <sub>4</sub> Perovskite.....	155
6.2.9	Optical Properties of the (DMAN)PbI <sub>4</sub> Perovskite.....	157
6.3	Conclusion and Future Work.....	159
Chapter 7	Conclusions and Future Work.....	161
Chapter 8	References.....	165

# Chapter 1 Introduction

Global climate changes have been observed since the early 20<sup>th</sup> century. The climate changes are primarily driven by human activities, especially fossil fuel burning, which increases the greenhouse gas level in the Earth's atmosphere. The heat-trapping greenhouse gas raises the average surface temperature of Earth, resulting in global warming.<sup>1</sup> 2020 was the hottest year on record globally, which has risen more than 2 degrees Fahrenheit since 1880s.<sup>2</sup> Attributed to climate change and ocean acidification, in the last 50 years, the world has lost 68% of the monitored population of mammals, birds, amphibians, reptiles and fish.<sup>3</sup> Meanwhile, the global energy crisis remains a significant problem for humans. By 2030 there is still about one billion people without access to electricity.<sup>4</sup> Therefore, in addition to looking for new ways to generate electricity renewably, reducing electricity usage can also contribute to sustainable development.

As more than 33% of the global electricity consumption is used for lighting, there is an excellent opportunity to save more energy using more efficient and low-cost lighting. Light systems used before are very inefficient. The efficiency of the tungsten filament bulb is about 5%, and the efficiency of the fluorescent lamp is about 25%.<sup>5</sup>

As an alternative to traditional lighting, light-emitting diodes (LEDs) provide significant energy savings. It was predicted that the widespread usage of LEDs in 10

years could save more than \$1 trillion on energy costs and meet the energy demands equal to a billion barrels of oil in 10 years.<sup>6</sup> Therefore, the emission of carbon dioxide can be substantially reduced. Since the discovery of electroluminescence by Henry Joseph Round in 1907<sup>7</sup>, LEDs based on various semiconductor materials have been developed, including group-IV, II-VI and organic emitters. In 2014, the first methylammonium lead iodide perovskite LED with an external quantum efficiency of 0.76% had been reported.<sup>8</sup> Following this success, perovskite LEDs have developed rapidly in the past seven years, and external quantum efficiency of 23.4% has been reported in 2021.<sup>9</sup> Their wide colour range, high colour purity, excellent brightness and low power usage have made them promising candidates for the next generation of lighting materials.

The inorganic-organic lead halide perovskite has become a leading contender for optoelectronic devices, such as photovoltaics<sup>8</sup>, LEDs<sup>9</sup>, transistors<sup>10</sup>, lasers<sup>11</sup> and water splitting cells<sup>12</sup>. However, organic-inorganic hybrid perovskites still face challenges, such as poor stability in the ambient atmosphere and low charge carriers binding energy. This thesis aims to offer a potential solution to these problems via confining perovskite with matrix and functional organic materials.

Chapter 2 describes the theoretical concepts and background knowledge related to physics discussed in the following chapters.

In Chapter 3, we introduce the experimental techniques we used to acquire results.

Chapter 4 describes a solution-processed method to infiltrate methylammonium lead

iodide (MAPbBr<sub>3</sub>) into the nanoporous GaN matrix. We also demonstrate the protective effect of the GaN matrix on MAPbBr<sub>3</sub> perovskite.

Chapter 5 investigates the confinement effect of the nanoporous GaN on MAPbBr<sub>3</sub> perovskite following the study in Chapter 4. We show an enhanced interaction of the charge carriers in MAPbBr<sub>3</sub> inside the nanoporous GaN matrix, revealing different recombination dynamics from the bulk MAPbBr<sub>3</sub> perovskite.

In Chapter 6, we demonstrate a solution-processed method to synthesize two dimensional (2D) perovskite with bis(propargyl ammonium iodide) anthracene (BPAIA) and 2,6-dimethylammoniumnaphthalene (DMAN). We show that the repulsion between the BPAIA is so large that a stable 2D perovskite structure is challenging to achieve. However, the DMAN lead iodide perovskite has the potential to be a candidate light emitting material.

Chapter 7 summarises critical results from Chapter 4, Chapter 5 and Chapter 6. We also include a brief discussion about the potential future research.



## Chapter 2 Background

This chapter introduces the background theory underlying the research in this thesis.

We start with a description of the fundamental photophysics of semiconductors. We first describe the origin of bandgap in semiconductors and then move on to the linear interaction between light and inorganic semiconductors. We then look into the charge carrier recombination mechanism in inorganic semiconductors, especially the confinement effect on these processes. Finally, we introduce the fundamental physics of organic-inorganic hybrid perovskite and gallium nitride, which are materials we investigate in the following chapters.



## 2.1 Semiconductor Photophysics

This thesis focuses on the photophysics of semiconductors. This section introduces the bandgap theory of semiconductors and the linear optical interaction between visible light and semiconductors.

### 2.1.1 Origin of the Bandgap

To understand the interaction between light and matter, we must understand the electronic band structure of the solid first. The origin of the bandgap can be explained by considering the atomic orbitals in the crystal lattice. When atoms are brought together to form a solid, the wavefunctions of atoms overlap, leading to the splitting of the electrons' eigenenergy. When a huge number of atoms pack together in crystals, each atomic orbital splits into a significant amount of energy levels, which are so close together that they can be effectively considered as a continuum band of allowed energy levels.<sup>13</sup> The highest occupied band is named the valence band (VB), while the lowest unoccupied band is called the conduction band (CB).<sup>14</sup> Valence bands are completely filled at  $T=0$  K, while conduction bands are completely empty. The energy gap between the CB and VB is called the bandgap ( $E_g$ ), and the value of the bandgap determines whether a material is a conductor, semiconductor or insulator.<sup>15</sup>

Conductors have one or more partially filled CB at  $T=0$  K. Semiconductors have one or more completely filled VB separated from a completely empty CB with an energy

gap  $E_g$  ( $0 \text{ eV} < E_g \leq 4 \text{ eV}$ ). As for the insulator, the energy gap is larger than 4 eV.

Bandgaps of semiconductors applied in optoelectronic devices are generally in ultraviolet, visible and infrared regions in the electromagnetic spectrum.<sup>15</sup>

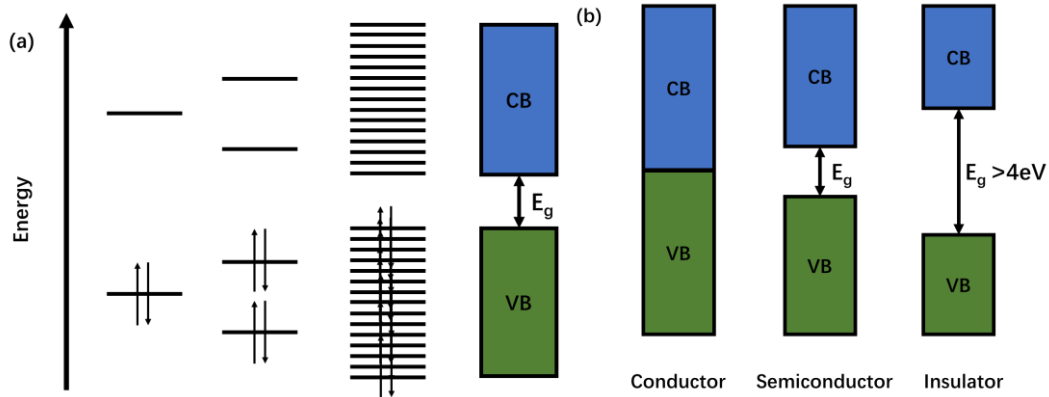


Figure 2-1 Diagrams of the origin of the bandgap. (a) A diagram reveals how continuum bands in crystals form from the discrete allowed energy levels in an isolated atom. (b) A diagram of band structures of conductors, semiconductors and insulators.

As for lead halide perovskite, the valence band maximum arises from the 6s orbital of the lead atom and the 5p orbital of the iodine atom. The conduction band minimum is from the 6p orbitals of the lead atom.<sup>16</sup>

The band theory can also be explained with quantum mechanics by solving the many-body Schrodinger equation for the periodic crystal structure:

$$\left( \frac{-\hbar^2}{2m} \nabla^2 + V(r) \right) \psi = E\psi, \quad (2.1)$$

where  $m$  is the electron mass,  $V(r)$  is the spatially dependent electronic potential,  $\psi$

is the electron wavefunction, and  $E$  is the energy of the electron. However, it is impossible to solve the many-body equation directly, as there are about  $10^{23}$  interacting outer electrons per cubic centimetre.<sup>17</sup> Therefore, we use the Born-Oppenheimer approximation (or adiabatic approximation) to simplify the equation. The Born-Oppenheimer approximation suggests that as the ions in the lattice are much heavier than the electrons, the electronic motion ( $\sim 10^{15} \text{ s}^{-1}$ ) is much faster than the ionic vibration ( $\sim 10^{13} \text{ s}^{-1}$ ). In this case, we regard ions as stationary relative to electrons, and the Hamiltonian is rewritten into:

$$H = H_{ions}(R_j) + H_e(r_i, R_{j0}) + H_{e-ion}(r_i, \delta R_{j0}), \quad (2.2)$$

where the  $H_{ions}(R_j)$  is the Hamiltonian for the ionic motion (ionic potential and the time-averaged adiabatic electronic potentials),  $H_e(r_i, R_{j0})$  is the Hamiltonian for the electron with the ions in the stationary position, and the  $H_{e-ion}(r_i, \delta R_{j0})$  gives the changes in electronic energy due to the displacement  $\delta R_{j0}$  of the ions from their equilibrium positions,  $R_j$  is the position of the  $j$ th ion core,  $r_i$  is the position of the  $i$ th valence electron.  $H_{ions}(R_j)$  and  $H_{e-ion}(r_i, \delta R_{j0})$  give us information about the vibrational and electron-phonon reaction in crystals, and the information about bandgap mainly comes from  $H_e(r_i, R_{j0})$ .<sup>17</sup>

The electronic Hamiltonian can further be simplified with the mean-field approximation assuming that every electron in the crystal lattice is experiencing the same average periodic potentials ( $V(r)$ ).<sup>18</sup> The equation can then be rewritten as

$$H_{1e}\psi_k(r) = \left(\frac{p^2}{2m} + V(r)\right)\psi_k(r) = E_k\psi_k(r), \quad (2.3)$$

where  $H_{1e}$  is the one-electron Hamiltonian,  $E_k$  is the corresponding energy eigenvalues, and  $\psi_k(r)$  is the wavefunction. According to Bloch's Theorem, the equation can be expressed in the form of

$$\psi_k(r) = u_k(r) \exp(i\vec{k} \cdot \vec{r}), \quad (2.4)$$

where  $u_k(r)$  is the periodic function with the periodicity of the crystal lattice, and  $\exp(i\vec{k} \cdot \vec{r})$  is a plane wave with wavevector  $\vec{k}$ . In the case of a crystal lattice, the  $V(r)$  of the electron is also periodic, as the atomic cores are regularly spaced at a distance of  $a$ . Therefore, the plane waves at the Brillouin zone boundaries  $\pm \frac{\pi}{a}$  undergo Bragg reflection. As a consequence, standing waves with higher charge density either at the atomic cores,

$$|\psi(-)|^2 \propto \sin^2\left(\frac{\pi x}{a}\right) \quad (2.5)$$

or in between the atomic cores

$$|\psi(+)|^2 \propto \cos^2\left(\frac{\pi x}{a}\right) \quad (2.6)$$

forms in one-dimension  $x$ . According to this result, wavevectors can have different energy depending on the high charge density position; thus, bandgap forms.<sup>18</sup>

When the minimum of the conduction band and the maximum of the valence band of a

semiconductor are at the same wavevector, this semiconductor has a direct bandgap. If the conduction band's minimum and the valence band's maximum are at different wavevectors, this semiconductor has an indirect bandgap. When the photoexcitation process happens, the indirect bandgap semiconductor needs to absorb or emit an additional phonon to conserve momentum.<sup>19</sup>

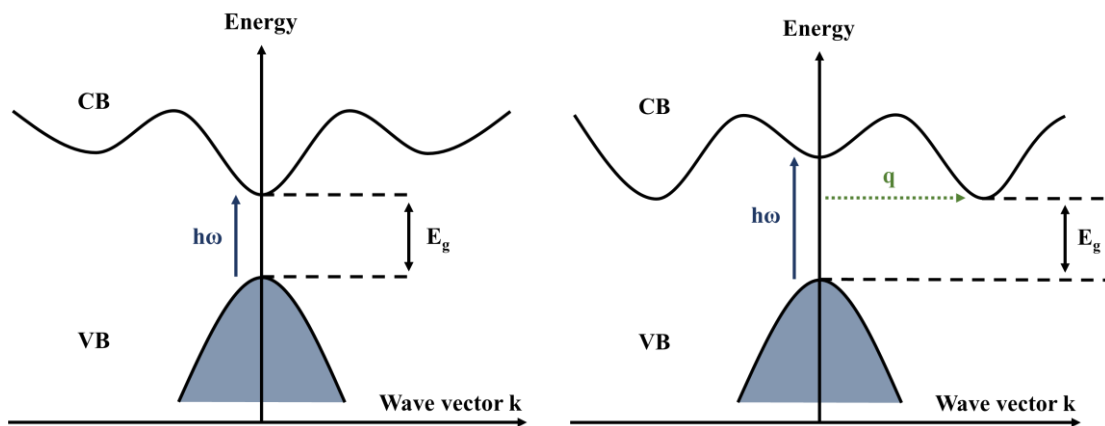


Figure 2-2 The representation of direct bandgap and indirect bandgap in k-space.

In this section, we present the band theory in the semiconductor. Based on these theories, we will move on to the next section to discuss the interaction between light and semiconductors.

## 2.1.2 Interaction of Light with Semiconductor

When light shines onto a semiconductor, it could be reflected by the semiconductor, interact with the semiconductor, or transmitted through the semiconductor. There are several types of interaction of light with semiconductors, including absorption, scattering and refraction, etc.<sup>19</sup> In this section, we focus on the absorption process.

Various models describe the absorption process, such as the classical dipole oscillator model and Fermi's golden rule.

The classical oscillator model assumes that in the semiconductor, every negatively charged electron and positively charged nuclei pair behaves as a classical electric dipole, of which the electric dipole moment is proportional to their separation. When the incident light exerts an alternating electric field on the electron-nuclei pair, it leads to the dipole oscillation. As the mass of the nuclei is significantly larger than the electron, only the electron will interact with the electric field of light. When the frequency of the incident light matches with the electron's natural resonance frequency, the electron behaves like the classical Lorentz oscillator and the light with a particular frequency is absorbed by the semiconductor.<sup>19</sup>

Fermi's golden rule, initially brought up by Dirac, describes the quantum mechanics of the light absorption process.<sup>20</sup> It reveals the transition rate from the initial state to the final state ( $|\psi_i\rangle \rightarrow |\psi_f\rangle$ ) with a perturbing interaction Hamiltonian  $H'$

$$\Gamma_{i \rightarrow f} = \frac{2\pi}{\hbar} |\langle \psi_f | H' | \psi_i \rangle|^2 \rho E_f, \quad (2.7)$$

where  $\rho E_f$  is the final state density, and  $\langle \psi_f | H' | \psi_i \rangle$  is the matrix element ( $M_{i \rightarrow f}$ ) of the perturbation Hamiltonian ( $H'$ ). The perturbation Hamiltonian ( $H'$ ) describes the dipole interaction between electron and incident light, and it can be related to the classical model<sup>19</sup>

$$H' = -P_e \cdot \varepsilon_{photon}, \quad (2.8)$$

where  $P_e$  is the electron dipole moment operator, and  $\varepsilon_{photon}$  is the electric field of the incident light. According to this equation, the matrix element, which indicates the strength of the electronic transition, only depends on the electric dipole moment of the semiconductor ( $P_e$ ) and the electric field strength of the incident light ( $\varepsilon_{photon}$ ). Fermi's golden rule depends on the first-order time-dependent perturbation theory.<sup>20</sup> When the interaction Hamiltonian oscillates at an angular frequency of  $\omega$  in an adiabatic system, the transition rate in the two-state model is proportional to:<sup>21</sup>

$$\Gamma_{i \rightarrow f} \propto |M_{i \rightarrow f}|^2 [\delta(E_f - E_i + \hbar\omega) + \delta(E_f - E_i - \hbar\omega)] \quad (2.9)$$

As a consequence, in an adiabatic system, only the transition of which the energy is the same as that of a photon  $\hbar\omega$  is allowed to happen. In other words, when the energy difference of the final state and initial state is  $\hbar\omega$ , the semiconductor is absorbing light; while the difference is  $-\hbar\omega$ , stimulated emission happens. The rapid oscillating term is neglected in this approximation.<sup>21</sup>

Optical density (OD) or absorbance is utilised to describe the quantity of light absorbed by the semiconductor. It is defined as the logarithm of the ratio between transmitted photon number through the semiconductor ( $n_{trans}$ ) and the incident photon number incident onto the semiconductor ( $n_{incid}$ ),

$$OD = -\log_{10} \left( \frac{n_{trans}}{n_{incid}} \right) \quad (2.10)$$

The absorption coefficient ( $\alpha$ ) describes the amount of light absorbed per thickness of the semiconductor. It can be calculated from the optical density of the material by dividing the OD by the thickness of the semiconductor,

$$\alpha = \frac{1}{d} OD = -\frac{1}{d} \log_{10} \left( \frac{n_{trans}}{n_{incid}} \right), \quad (2.11)$$

in which  $d$  is the thickness of the semiconductor.

### 2.1.3 Thermalisation and Recombination Process

After photoexcitation at appropriate energy under room temperature, the generated carriers will relax in the semiconductor through four overlapped temporal regimes:

- The decoherent regime ( $\sim 10$  fs)
- The thermalisation regime ( $\sim 0-500$  fs)
- The cooling regime ( $\sim 0.5-50$  ps)
- The isothermal regime ( $> 1$  ps)

The decoherent regime

A coherent population of free charge carriers is generated immediately after photoexcitation. At this regime, the system is coherent, as there is a well-defined

relationship between the phase of the exciting electromagnetic field and the photoexcited free carrier distribution. The distribution of coherent carriers is determined by the electromagnetic field of the incident light. This non-thermal distribution is rapidly destroyed within a few tens of femtoseconds due to the scattering of free carriers.<sup>22</sup>

### The thermalisation regime

The excitation generated charge carriers' thermalisation is via the carrier-carrier scattering, including electron-electron, electron-hole, and hole-hole scattering.<sup>23</sup> It is mediated by the Coulomb interaction. It happens in the first ~500 fs after excitation. The relaxation process is extremely fast. Taking  $\text{CH}_3\text{NH}_3\text{PbI}_3$  as an example, the thermalisation process lasts below 10 fs to 85 fs, depending on the carrier density and the excess energy above the bandgap.<sup>23</sup> The thermalisation results in a spectral broad thermalised Fermi-Dirac distribution,

$$n_i = \frac{1}{e^{\frac{\epsilon_i - \mu}{k_B T}} + 1} \quad (2.12)$$

where  $n_i$  is the average number of electrons/holes in state  $i$ ,  $\epsilon_i$  is the energy level of state  $i$ ,  $\mu$  is the Fermi level,  $k_B$  is the Boltzmann constant, and  $T$  is the temperature of electrons/holes.<sup>24</sup> Then, electrons and holes will reach a “quasi-equilibrium” state separately. In this state, electrons will be thermally equilibrated with other electrons, and holes with other holes, while the temperature of the carriers ( $T_C$ ) is higher than the

lattice ( $T_L$ ). These carriers are referred to as hot carriers.<sup>24</sup>

### Cooling Regime

In the cooling regime, the hot carriers scatter with phonons that are quantum of lattice vibration<sup>25</sup>, lowering their temperature and reaching equilibrium with the lattice. In ionic crystals like perovskites, the most critical scattering process is the polar interaction, which is the interaction between electrons and long-wavelength longitudinally polarised optical (LO) phonons.<sup>26</sup>

The carrier cooling process includes two steps in lead halide perovskite.<sup>27,28</sup> In the first step in the first  $\sim 2$  ps, hot carriers cool down rapidly by interacting with longitudinal optical phonons<sup>29,30</sup>, with the cooling rates varying from 230 fs to 770 fs depending on the carrier density ranging from  $6 \times 10^{17} \text{ cm}^{-3}$  to  $6 \times 10^{18} \text{ cm}^{-3}$ .<sup>27</sup> At higher carrier density, the cooling rate decreases as the carriers reabsorb the longitudinal optical phonons and undergo reheating. This phenomenon is known as the hot phonon bottleneck effect and is commonly observed in inorganic semiconductors.<sup>27,31,32</sup> After the first  $\sim 2$  ps, carriers slowly cool down with interacting with delayed longitudinal optical photons or lower energy acoustic and optical phonons.<sup>27</sup>

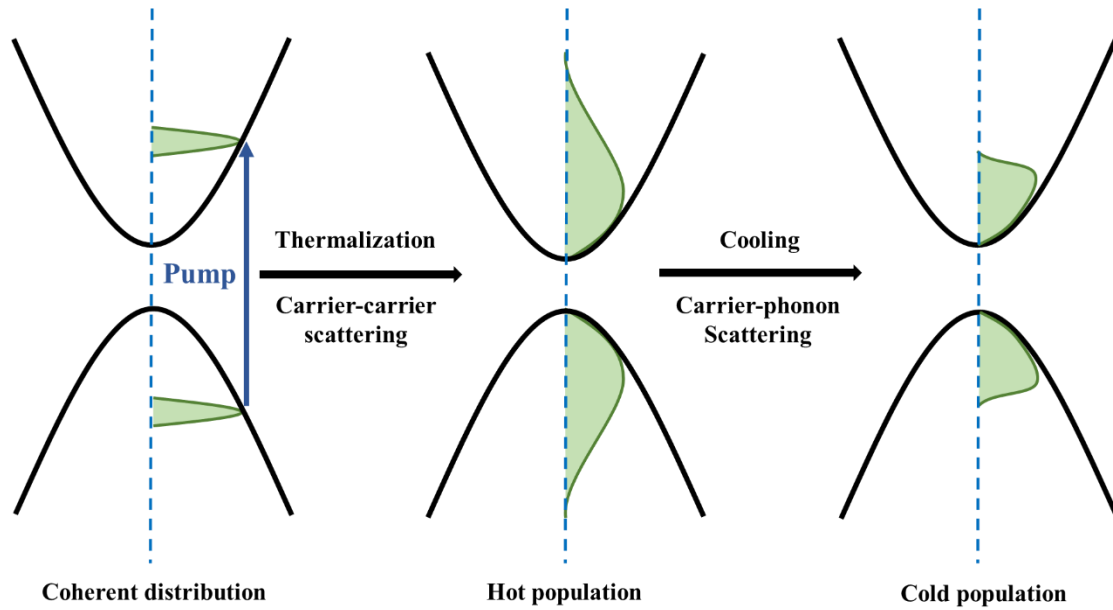


Figure 2-3 The representation of the thermalisation regime and cooling regime.

### The isothermal regime

In the isothermal regime, photoinduced carriers have the same temperature as the lattice. Charge carriers relax back to the ground state via recombination processes.<sup>28</sup> In general, there are four principal types of intrinsic recombination, including both radiative and non-radiative processes.<sup>33,34</sup>

### Geminate recombination

Geminate recombination happens if the photoexcited carriers contain bound excitons and electron-holes pairs. It is a radiative recombination process. In this case, the recombination rate  $\Gamma$  only depends on the density of excitons,

$$\Gamma_G = \alpha n, \quad (2.13)$$

in which  $\alpha$  is a constant and  $n$  is the density of excitons.

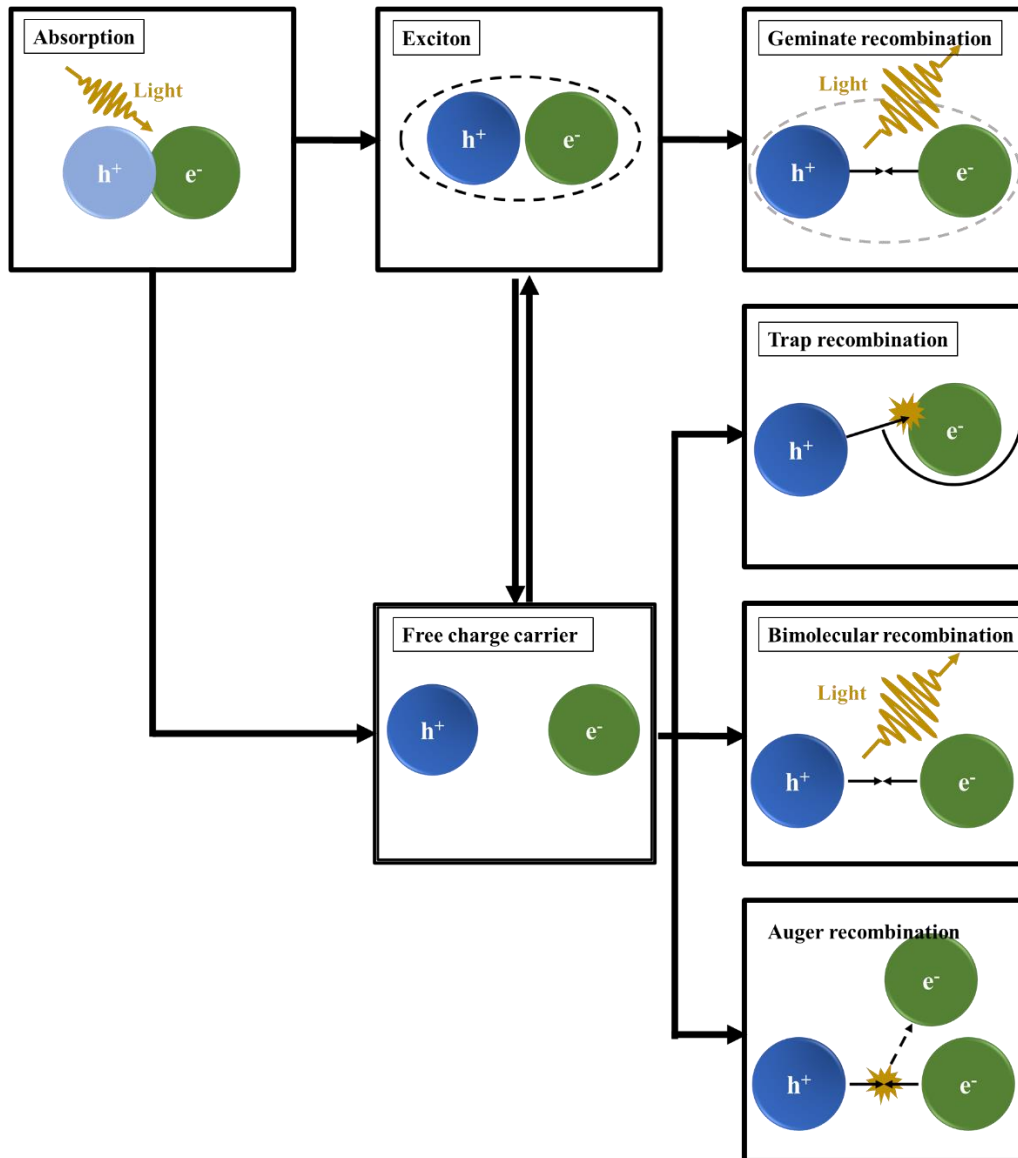


Figure 2-4 A diagram of the photophysical processes in semiconductors after photoexcitation.

#### Auger recombination

Auger recombination is a process involving three carriers. The energy generated from the recombination of an electron and a hole excites another carrier to its excited state

rather than emitting a photon. Then the excited carrier thermalises back to the bottom of the conduction band. Therefore, the Auger recombination rate is linearly proportional to the density of each of the charge carriers. Auger recombination usually happens at a high carrier density. It results in radiative efficiency loss; therefore, it is an unwanted recombination process.

### Shockley Read Hall (SRH) Recombination

The crystal defects in semiconductors, such as dislocations, impurities and disorders introduce trap or defect states. In Shockley Read Hall recombination free charge carriers are “captured” by the defects<sup>14</sup>, as defects are more localised than free charge carriers. Electrons and holes will lose their energy separately through the non-radiative process. The Shockley Read Hall recombination rate can be expressed as,

$$\Gamma_{SRH} = \frac{np - n_i^2}{\tau_n(p + p_t) + \tau_p(n + n_t)}, \quad (2.14)$$

in which  $n_i$  is the intrinsic carrier density,  $\tau_n$  and  $\tau_p$  is the capture lifetime of electrons and holes by defects, and  $n_t$  and  $p_t$  are the density of electrons and holes when their quasi-Fermi levels reach the trap energy level separately.

### General recombination rate equation

The charge carrier recombination process in semiconductors is the sum of various competing recombination mechanisms, including both radiative and non-radiative

recombination processes, depending on the photoexcited charge carrier density  $n(t)$ .

The general recombination rate can be expressed as<sup>33,35</sup>,

$$\Gamma_{sum} = k_1 \cdot n(t) + k_2 \cdot n(t)^2 + k_3 \cdot n(t)^3, \quad (2.15)$$

in which  $k_1$ ,  $k_2$  and  $k_3$  are the recombination rates of the first, second and third-order recombination rate constant. The first order recombination is the dominant recombination process in inorganic semiconductors with high trap densities<sup>35</sup> or heavily doped. If the major photoexcited particles are bound excitons, the dominant recombination process is the first order recombination<sup>36</sup>. In addition, when charge carriers are dielectrically or spatially localized, the dominant recombination process is also geminate recombination.<sup>37-39</sup> The second order recombination is the dominant process when the dominant charge carriers are free electrons and holes in inorganic semiconductors. The third order recombination is dominant when the carrier density in inorganic semiconductors is high or when the semiconductor is heavily doped.<sup>36,40</sup>

In bulk lead halide perovskite, the dominant recombination mechanism at low photoexcitation densities below  $\sim 10^{16} \text{ cm}^{-3}$  is the first order recombination. At medium photoexcitation around  $10^{16}$ - $10^{18} \text{ cm}^{-3}$ , the dominant recombination mechanism is the second-order recombination, and at high photoexcitation densities above  $10^{18} \text{ cm}^{-3}$  is normally the third order recombination<sup>40</sup>.

The photoexcited carrier dynamic can be investigated using the measurement of

transient absorption (TA) and transient photoluminescence (TPL). Both are time-resolved spectroscopic techniques. The detailed measurement process will be described in Chapter 3.

Photons are emitted through the radiative recombination process. The efficiency of radiative recombination is essential for the performance of optoelectronic devices. It can be quantified by the photoluminescence quantum efficiency (PLQE)<sup>41</sup>,

$$PLQE = \frac{k_{rad}}{k_{rad} + k_{non-rad}}, \quad (2.16)$$

where  $k_{rad}$  is the radiative recombination rate and  $k_{non-rad}$  is the non-radiative recombination rate. It can be measured with the integrating sphere method described in Chapter 3.

## 2.1.4 Charge Carriers

In the ground state of the system, the semiconductor's valence band is completely full, while the conduction band is completely empty. When energy is put into a two-bands system, a negatively charged electron in the valence band will be promoted to the upper conduction band, leaving a positively charged hole in the lower band. These two types of particles are equal but with opposite charges. The free electron can move freely into other states in the conduction band with minimal energy change, and so is the hole in the valence band. The electron and hole can be regarded as quasiparticles. These quasiparticles only exist in crystals. They can annihilate via the recombination process

when the electron falls back to the valence band and recombine with the hole.<sup>42</sup> This is the recombination process we have discussed in Section 2.1.3.

As the electron and hole have opposite charges, they will be attracted to each other via Coulombic force. This bounded state of an electron-hole pair is called an exciton. Excitons commonly exist in insulators and semiconductors. It is an electrically neutral quasiparticle.

Depending on the bonding strength, excitons can be classified into Frenkel exciton and Wannier-Mott exciton. Frenkel excitons are tightly bounded electron-hole pairs, and they usually localise within one or two unit cells. They are typically found in ionic crystals. Very weakly coupled electron-hole pairs are known as Wannier-Mott excitons. They can spread over several unit cells due to the large dielectric constant of the media.

Exciton bound states lie below the energy gap of the semiconductor. The exciton binding energy is subtracted from the energy needed to create a free electron and hole.<sup>42</sup>

The dimensionality of the semiconductor will influence the binding energy, the Rydberg series and the oscillator strength of excitons. Although the motion of the electron-hole pair is restricted to a two-dimensional plane, the interaction is still in three-dimensional space.<sup>43</sup> Therefore, the wave vectors of exciton in the three-dimensional and two-dimensional systems are  $k_{3d}$  and  $k_{2d}$

$$k_{3d} = \sqrt{k_x^2 + k_y^2 + k_z^2} \quad (2.17)$$

$$k_{2d} = \sqrt{k_x^2 + k_y^2}, \quad (2.18)$$

the oscillator strength  $f(n_B)$  increases with the reducing of dimensionality

$$f(n_B)_{3d} \propto n_B^{-3} \quad (2.19)$$

$$f(n_B)_{2d} \propto \left(n_B - \frac{1}{2}\right)^{-3}, \quad (2.20)$$

and the Bohr radius  $a_B$  decreases

$$a_B(3d) \propto a_0 n_B \quad (2.21)$$

$$a_B(2d) \propto a_0 \left(n_B - \frac{1}{2}\right), \quad (2.22)$$

in which  $n_B$  is the principle quantum number, and the quantum number reduced by  $\frac{1}{2}$  when goes from three- to two-dimensional system. Additionally, the quantisation energy needs to be considered when the dimension of the system reduces

$$E_{ex} = E_Q + \frac{-R_{y_{ex}}}{N^2} + \frac{\hbar^2 k^2}{2(m_e + m_h)} \quad (2.23)$$

In Type-I heterojunction quantum well (or multi-quantum well), quasi-two-dimensional excitons exist. The quantisation in the z-direction leads to the enhanced oscillator strength, as the overlap of the electron-hole pair is larger and the Bohr radius is smaller in the quantum well. In this case, although the motion in the z-direction is confined, the width of the quantum well is not zero ( $l_z \neq 0$ ). With the increase of the finite quantum well thickness from zero, the binding energy increases first, followed by a decrease

after a certain thickness depending on various materials.<sup>15</sup>

It is challenging to observe the excitonic effect at room temperature in many direct bandgap semiconductors due to the rapid collisions of excitons with optical photons. Although the exciton effect determines the shape and strength of the interband absorption, the peak of the bound states is challenging to resolve from the absorption.<sup>44</sup>

## 2.1.5 Quantum Wells

A heterojunction is an interface between two semiconductors with unequal bandgaps. Depending on the alignment of bandgaps, semiconductor heterojunctions can be divided into three types, type I (straddling gap), type II (staggered gap) and type III (broken gap). If the electrons and holes have their lowest energies in the same material, the heterojunction is type I. If electrons and holes have their lowest energies in different materials, the heterojunction is type II.<sup>45</sup>

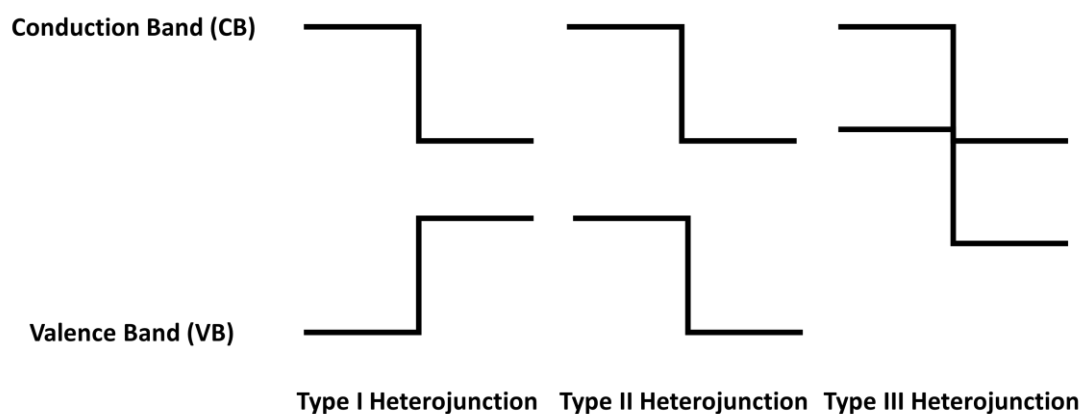


Figure 2-5 The illustration of three types of heterojunctions.

A quantum well is a type of heterojunction of semiconductors that join together at the

atomic level. It is constructed of one thin layer of material surrounded by two layers of barrier materials. Both electrons and holes are confined in the well about 100 Å width. The energy states in the quantum well are quantised. The allowed states correspond to standing waves in the direction perpendicular to the layers.<sup>15</sup>

The barriers are infinitely high in the infinite well, and wavefunction must be zero at the quantum well walls. The eigenenergy and eigenfunction to the  $n^{\text{th}}$  solution to the Schrodinger's equation are<sup>46</sup>

$$E_n = -\frac{\hbar^2}{2m} \left( \frac{n\pi}{l_z} \right)^2 \quad n = 1, 2, 3 \dots \quad (2.24)$$

$$\phi_n = A \sin \left( \frac{n\pi z}{l_z} \right), \quad (2.25)$$

where  $m$  is the effective mass of the particles,  $l_z$  is the width of the well. We know from these equations that the wavefunction are sine waves. The energy levels are quadratically spaced. The spacing is larger when the well is narrower and the effective mass is smaller.

Actual quantum wells have finite height barriers. Therefore, the wave can tunnel into the barriers. The wavefunctions of the bound states are sine waves inside the quantum well, but they are exponentially decaying in the barriers. The energy levels are also lower than those calculated from the infinite well model.<sup>46</sup>

When several quantum wells are brought together, if the barrier thickness is too thick

for the wavefunction to penetrate though, this structure is known as a multi-quantum well (MQW). If the wavefunction can overlap with that of the adjacent quantum well, it is called a superlattice. If there is a significant amount of wavefunction penetrating between wells, “mini bands” are similar to the energy band arising from atoms in crystalline materials form. <sup>15</sup>

As we described in Section 2.1.2, an electron in the valence band of a bulk semiconductor can be promoted to the conduction band with the same momentum by absorbing a photon. Although the energy of the transition will be different, all the transitions from the valence band to the conduction band will have the same strength for vertical transition. Consequently, the absorption edge of the bulk semiconductor rises as a square root of energy. <sup>46</sup>

For quantum wells, in addition to the momentum selection rule, the transition only occurs between states with the same quantum number in the valence band and conduction band. This is because the absorption strength is proportional to the overlap integral of the wavefunctions, and in quantum wells, only a finite overlap between identical standing waves occurs. Electrons and holes confined in only one dimension can still move freely parallel to the layers in quantum wells. As a result, instead of discrete energy states, “subbands” of energy states form. In one particular “subband”, charge carriers can have any amount of kinetic energy due to their free in-plane motion, i.e. they can have any energy larger than the confined energy band. Therefore, the

density of states are actually steps that start at certain confinement energy levels, and the absorption edge is a series of steps, one step for each quantum number, in the quantum well.<sup>19</sup>

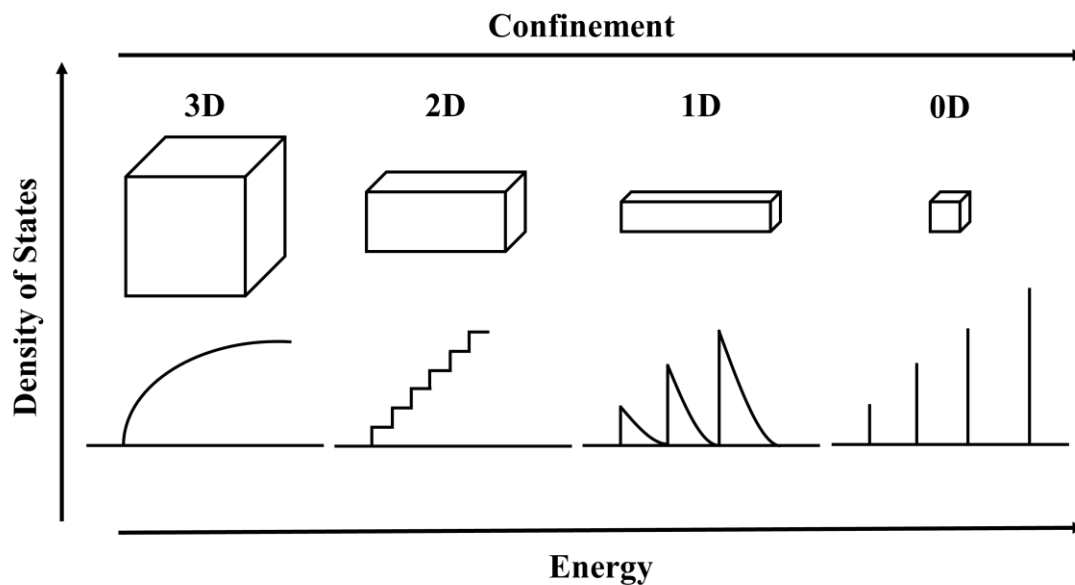


Figure 2-6 Density of states in one band of a semiconductor with different dimension.

### Dielectric confinement

When two semiconductors with different dielectric constants are brought together, charges will accumulate at the boundary of the two materials. It will change the dielectric screening of charged particles in this system, as the created electric field will penetrate the barrier material with a smaller dielectric constant. Therefore, the system's effective dielectric constant will reduce, and the Coulomb interaction between electrons and holes will be stronger, leading to larger exciton binding energy.<sup>45</sup>

### Quantum confinement

When the size of the semiconductor is of the same magnitude as the electron wavefunction's de Broglie wavelength, the electronic and optical properties of materials are different from those of the bulk material. When the confinement dimension is small enough, usually smaller than the exciton Bohr radius of the material, energy states become discrete, and the bandgap becomes size-dependent. With the decrease of the particle size, the wavelength of the emission light is blue-shifted. Additionally, the exciton binding energy will increase, leading to the enhancement of radiative recombination.<sup>47</sup> This phenomenon is known as quantum confinement. Quantum confinement can be observed in semiconductor nanoparticles. For example, a quantum dot is confined in three dimensions, a quantum wire is confined in two dimensions, and a quantum well is confined in one dimension.<sup>45</sup>

Quantum dots are zero-dimensional nanocrystals, and the energy level of the electrons and holes depends on the angular momentum quantum number  $l$  and principal quantum number  $n$

$$E_{l,n}^{e,h} = \frac{\hbar^2 \Phi_{l,n}^2}{2m_{e,h} \alpha^2}, \quad (2.26)$$

in which  $m_{e,h}$  is the effective mass of e and h,  $\alpha$  is the radius of the nanocrystals,  $\Phi_{l,n}$  is the  $n^{\text{th}}$  root of the spherical Bessel function of the order  $l$ , i.e.  $j_l(\Phi_{l,n}) = 0$ .<sup>48,49</sup>

The quantitative blueshift of the photoluminescence depending on nanocrystal size can be expressed with the Brus equation

$$E^* = E_g + \frac{\hbar^2 \pi^2}{2\mu R^2} - \frac{1.8e^2}{4\pi\epsilon_0\epsilon_r R}, \quad (2.27)$$

where  $E^*$  is the energy of the emitting photons,  $R$  is the radius of the nanoparticles and  $E_g$  is the bandgap of the semiconductor.<sup>50</sup>

### **Excitons in quantum well**

Due to the quantum well's confinement effect, excitons in the quantum well are smaller than in bulk semiconductors. Consequently, the electrons and holes are much closer and have larger binding energy than in three-dimensional cases. Therefore, the absorption strength of excitons is stronger and can easily be resolved from interband absorption even at room temperature in some cases.<sup>15</sup>

## **2.2 Inorganic Organic Lead Halide Perovskite**

### **2.2.1 History of Perovskite**

The perovskite crystal structure is a lattice structure class with the same crystal structure of calcium titanate  $\text{CaTiO}_3$  lattice. Calcium titanate was first discovered by Gustav Rose in 1839 and was named after the Russian mineralogist, who was the first characterising its mineral structure, Count Lev Aleksevich von Perovskite.<sup>51,52</sup> Organic-inorganic halide perovskites were first synthesized and characterised in the 1970s. Weber's group synthesized the first methylammonium lead halide perovskites.<sup>53</sup> In 2009, Miyasaka's group fabricated methylammonium lead bromide perovskite solar cells with 2.2%

power conversion efficiency.<sup>54</sup> Since then, organic-inorganic perovskites have received extraordinary attention due to their noble properties. They have been applied in various optoelectronic devices<sup>55,56</sup>, including solar cells<sup>54,57</sup>, light-emitting diodes<sup>58,59</sup>, lasers<sup>11,60-62</sup>, transistors<sup>63</sup> and photodetectors<sup>64,65</sup> etc. In 2021, perovskite solar cells efficiency has reached 25.2%<sup>66</sup>, and the efficiency of perovskite/silicon tandem solar cells has reached 29.5%<sup>67</sup>. Perovskite LEDs have been developed rapidly in the past seven years, and external quantum efficiency of 23.4% has been reported in 2021.<sup>9</sup>

This thesis focuses on three-dimensional and two-dimensional organic-inorganic lead halide perovskite

## **2.2.2 Structure of Organic-inorganic Metal Halide Perovskite**

The general formula of perovskite is  $ABX_3$ , where A atom normally is an organic cation, B is a metal cation, and X is an anion. In ideal three-dimensional perovskite, B cations and X anions form a network of corner-sharing  $BX_6$  octahedra, with A cations filling into the 12-fold coordinated hole of the  $BX_6$  network and balancing the charge.

The crystal structure of three-dimensional perovskite was first studied by Victor Goldschmidt in 1926.<sup>68</sup> He proposed that a three-dimensional perovskite structure can only be formed from the combination of atoms with particular sizes. The ionic radii must satisfy the following condition:

$$t_f = \frac{(r_A + r_X)}{\sqrt{2}(r_B + r_X)}, \quad (2.28)$$

where  $r_A$ ,  $r_B$  and  $r_X$  are ionic radii of A cation, B cation and X anion,  $t_f$  is the Goldschmidt tolerance factor. Normally the tolerance factor should be between 0.75 and 1 to form a stable three-dimensional perovskite structure.<sup>69</sup> Although there is a size limitation, a number of various atomic and molecular combinations can meet this condition to form perovskite. Therefore, perovskite could be metallic<sup>70</sup>, semiconducting<sup>71</sup> and insulating<sup>72</sup> depending on its components and could exhibit a wide range of interesting properties. Typically perovskites have three types of structure: cubic structure (Pm3m), tetragonal structure (I4/mcm) and orthorhombic structure (Pnam), depending on temperature and the size of components.<sup>63</sup>

### 2.2.3 Properties of Perovskites

Organic-inorganic lead halide perovskites have exhibited excellent optoelectronic properties. Compared to silicon light absorbers, perovskites have direct bandgap and large absorption coefficients.<sup>73</sup> Therefore, photovoltaic devices based on a very thin perovskite layer can be achieved. The diffusion length of charge carriers in perovskite reaches a micrometre scale in single crystals and thin films.<sup>74,75</sup> The binding energy of excitons in perovskite is small, leading to the generation of free charge carriers at room temperature.<sup>76,77</sup> The recombination lifetime of carriers is long.<sup>60</sup> Thus, the bimolecular recombination rate is small. Also, the emission colour of perovskites can be easily tuned

by changing the compositions or changing the crystal size.<sup>58,78</sup> In addition, lead halide perovskites shows remarkable properties, such as ferroelasticity<sup>79</sup>, piezoelectricity<sup>80,81</sup> and giant photostriction<sup>82</sup>, making it possible to apply them in a wide range of fields. The band structure near the bandgap of perovskite is dominated by the atomic orbitals of lead and halide. The HOMO/LUMO level of organic moiety contributes minor to the bandgap. Primarily it provides electrostatic charge compensation. The conduction band is dominated by the lead 6p non-bonding orbitals, and the valence band is dominated by the antibonding halide 5p and lead 6s orbitals.<sup>83</sup>

## 2.2.4 Two-dimensional Perovskites

Low dimensional organic-inorganic hybrid perovskite derivatives are bulk quantum materials. Charge carriers in low dimensional perovskite are localised within ordered metal halide sheets, rods, or clusters separated by cationic lattices. Based on how the metal halide octahedra network connects, perovskites can be classified into various dimensionalities. The  $BX_6$  octahedra framework of three-dimensional perovskites connects along all the four-fold octahedral axes in a corner-shared way. Two-dimensional (2D) perovskites can be regarded as layered structures slicing off along specific crystallographic phases from three-dimensional perovskites. A superposition of three-dimensional (3D) perovskite and two-dimensional (2D) perovskite is quasi-two-dimensional perovskite  $((ABX_3)_{n-1}A_2BX_4)$ . The octahedra  $BX_6$  network of one-dimensional perovskites  $(A_3BX_5)$  only connects along one axis. It can be derived from

two-dimensional perovskites by slicing perpendicular to the inorganic sheet.

Moreover, nonconnected octahedra-based clusters can be generated by further slicing off one-dimensional perovskites. The clusters are known as zero-dimensional perovskites ( $A_4BX_6$ ). As mentioned above, the tunability of the dimensionality and the flexibility of the structure can introduce a broader family of perovskites with various physical properties to explore in the development of new optoelectronic materials.<sup>84</sup>

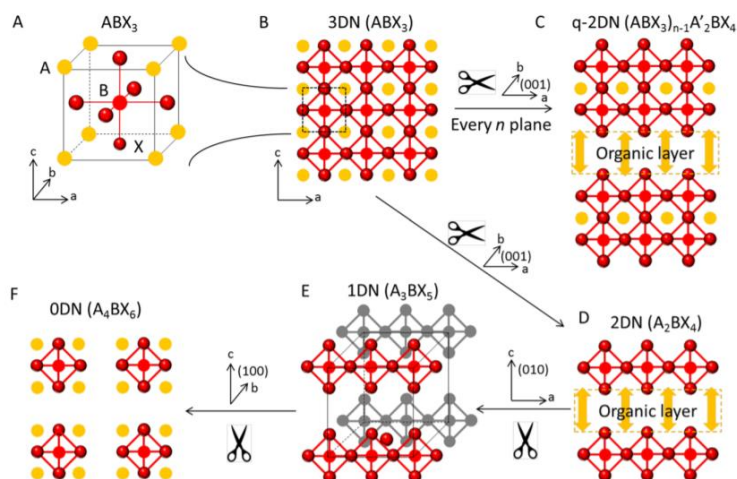


Figure 2-7 Schematic representations showing the connectivity of  $BX_6$  octahedra in low-dimensional perovskites and their formation by slicing 3D perovskite along crystallographic planes. (A) 3D perovskite unit cell. (B) 3D perovskites projected in the (010) plane (C) 3D perovskite is sliced along (100) planes to form quasi-2D perovskite; (D) 3D perovskite is sliced along the (100) plane to form 2D perovskite, presenting octahedra connection along two axes. (E) 2D perovskite is sliced along the (010) plane to form 1D perovskite, featuring octahedra networking along one axis. (F) 1D perovskite is sliced along the (001) plane to form 0D perovskite, demonstrating

isolated octahedra.<sup>84</sup>

Although Goldschmidt's tolerance factor limits the organic and inorganic composition in three-dimensional perovskites, there is no such restriction for low dimensional perovskites.<sup>85</sup> For example, there is no length restriction for the A cation in two-dimensional perovskites. However, the width of cations must fit into an area defined by the terminal halides from four adjacent corner-sharing octahedra. If the organic cation is too wide, it will lead to steric hindrance with the adjacent organic molecule. Whereas if the cation is too small, the inorganic molecules will tilt.<sup>47</sup>

The 2D perovskite layered structures form a natural multi-quantum-well system. The inorganic lead halide layers can be considered as quantum wells and the organic layers as quantum walls. This system will enhance the dielectric confinement of charge carriers and push up the binding energy to several hundred meV.<sup>86</sup> Due to the strong confinement of charge carriers, 2D perovskites are promising light-emitting materials. Additionally, the 2D perovskite quantum well thickness can be easily tuned by varying the n value, thereby changing their optoelectronic properties.<sup>87</sup> Unlike layered transition metal dichalcogenides, 2D perovskites are built up with more flexible and deformable backbones, which is suitable for soft devices.<sup>88</sup> Two-dimensional perovskites also display more excellent moisture resistance than three-dimensional perovskites and can be prepared under humid conditions.<sup>89</sup> For instance,  $(\text{BA})_2(\text{MA})_{n-1}\text{Pb}_n\text{I}_{3n+1}$  ( $n=1,2,3,4\dots$ ) 2D perovskite films synthesized via spin coating remains unchanged after being

exposed to a 40% humidity environment for two months, while the MAPbI<sub>3</sub> three-dimensional perovskite films prepared in a similar way decomposes only after a short term.<sup>90</sup>

Based on the structure of organic spacer cations, 2D perovskite can be classified into two phases, the Ruddlesden-Popper (RP) phase<sup>87,91,92</sup> and the Dion-Jacobson (DJ) phase<sup>93</sup>. The general formulas for the RP phase and DJ phase are  $A'_2A_{n-1}B_nX_{3n+1}$  and  $A'A_{n-1}B_nX_{3n+1}$  respectively (A': organic spacer cation, A: small organic cation, B: metal cation, X: halide anion), where the interlayer spacer cation A' for the RP phase is monovalent ammonium cations and the interlayer spacer cation A' for the DJ phase is bivalent ammonium cations.<sup>94-97</sup>

Typically, the RP phase perovskite has a larger interlayer distance between the adjacent lead halide layers as bilayers of spacer cations are demanded. Therefore, the layer separation varies from 1.5 times the cation's length to more than double its length, depending on their packing.<sup>98</sup> The gap between two organic spacer layers makes the layers in the RP phase perovskite relatively isolated. Thereby an excitonic emission directly from the spatial electronic confinement of the individual layer can be detected. An offset per unit cell will form in the RP phase perovskite.<sup>91</sup>

Conversely with the RP phase perovskite, the DJ phase perovskite layers stack with either perfect alignment or a minor misalignment depending on the spacer size.<sup>93</sup> Therefore, the organic cations need to fit in the inorganic framework snugly. The close

layer packing generates a weak interaction between perovskite layers, resulting in a redshift of the excitonic peak.

## 2.2.5 Perovskite nanocrystals

In addition to bulk lead halide perovskites, perovskite nanocrystals can be easily synthesized via various approaches. They also reveal promising optical and electronic properties. Different from bulk perovskites, the optical properties of nanosized perovskite crystals can be tuned due to the quantum confinement effect.<sup>99–101</sup> Meanwhile, bulk perovskites suffer from low photoluminescence efficiency due to inherent defects at surfaces, interfaces and grain boundaries<sup>102,103</sup>, while the photoluminescence of perovskite nanocrystals is promising<sup>104,105</sup>. Besides, comparing with conventional colloidal semiconductor quantum dots, perovskite nanocrystals exhibit high PLQE even without surface passivation.<sup>99</sup> Therefore, perovskite nanocrystals are widely applied in lasers, LEDs and photodetectors.

This section introduces synthesis methods and optical properties of methylammonium lead halide perovskite nanocrystals. We will focus on the in situ synthesis approaches and the quantum confinement effect on perovskites as they relate closely to the research on infiltrating methylammonium lead bromide (MAPbBr<sub>3</sub>) perovskite into the gallium nitride (GaN) matrix.

Over the past decades, researchers have developed various reliable and facile perovskite

nanocrystals synthesis approaches. These methods could generally be classified into four subcategories: 1) heat up approaches, including hot injection<sup>106,107</sup> which is the most frequently utilised method; 2) the reprecipitation approaches, including the ligand-assisted re-precipitation (LARP), which is a low-cost and widely applied synthesis method<sup>99,100,105</sup>; 3) in situ synthesis method, via which perovskite nanocrystals could be synthesized on various substrates<sup>108–111</sup>; 4) bulk to nano approaches, via which the crystal size is reduced by mechanical milling or exfoliation<sup>112,113</sup>.

Hot injection is one of the most frequently used methods in perovskite nanocrystal synthesis. High-quality perovskite nanocrystals with high PLQE have been generated via this method. In the synthesis of methylammonium lead halide perovskite nanocrystals, the hot injection method involves injecting methylamine in tetrahydrofuran (THF) with oleic acid (OA) into a vigorously stirring solution of lead halide in oleylamine (OAm) and OA mixture at high temperature in the inert atmosphere, followed with immediate quenching the reaction by reducing the temperature.<sup>114</sup> Over the last decades, different precursors and ligands have been explored to achieve better shape control and stability.<sup>115</sup> However, this tedious reaction requires high temperature and an inert environment. Consequently, the cost of mass production would be high.

LARP is another widely used approach to synthesize high-quality methylammonium

lead halide perovskite nanocrystals. Via the LARP approach, precursors of the perovskite and ligands are mixed in a good solution such as dimethylformamide (DMF) or dimethyl sulfoxide (DMSO). Then the mixture is dropped into a poor solvent (toluene or hexane), forming ligand-capped colloidal perovskite nanoparticles.<sup>105</sup> The nanoparticles size can be tuned by changing the reaction temperature. The shape control of the LARP approach is not as promising as the hot injection method.

Although the hot injection and LARP methods are a great success, especially in shape-controlled synthesis of high-quality methylammonium lead halide perovskite, synthesized nanocrystals suffer from drawbacks such as fragile surface chemistry and poor stability. Consequently, it is challenging to maintain their superior properties when developing thin films with nanocrystals or embedding nanocrystals into a solid matrix.

In situ synthesis method (synthesis on a substrate) offers a potential solution to overcome these problems. In situ synthesis is not a suitable approach to prepare conventional II-VI semiconductor quantum dots because high reaction temperature is demanded to overcome the high formation enthalpy of II-VI semiconductors. Under these circumstances, high PLQE is difficult to achieve.<sup>116</sup> However, as an ionic semiconductor, the formation enthalpy of perovskites is low, while the defect tolerance of perovskite is high.<sup>117</sup> Via the in situ growth method, perovskite nanocrystals can be directly prepared not only in a hard matrix, such as aluminium oxides<sup>109,118</sup>, MoF<sup>119,120</sup>, glasses<sup>110,111</sup> and molecular sieves<sup>121</sup>, but also in a soft polymeric matrix<sup>122</sup>. Therefore,

in situ growth approaches of perovskite nanoparticles can be applied in developing high-quality methylammonium lead halide perovskite nanocrystals for light emitting and colour conversion applications. In addition, the poor stability of perovskite nanocrystals is a significant drawback in advancing them to an actual application, while a matrix can improve the stability of perovskite nanoparticles<sup>122</sup>.

In 2012 Kojima group reported the first in situ fabrication of MAPbBr<sub>3</sub> nanocrystals on the mesoporous Al<sub>2</sub>O<sub>3</sub> substrate.<sup>109</sup> Diluted MAPbBr<sub>3</sub> solution was spin-coated on mesoporous Al<sub>2</sub>O<sub>3</sub> substrate, and 5 nm MAPbBr<sub>3</sub> nanocrystals were synthesized inside pores. The quantum confinement effect leads to an enhanced PL.<sup>109</sup> This research opens up the exploration of perovskite nanocrystal based composites. Since then, Malgras' group prepared MAPbBr<sub>x</sub>I<sub>3-x</sub> (0 ≤ x ≤ 1) perovskite nanoparticles in mesoporous silica powder simply via infusing silica powders with perovskite precursor solutions.<sup>123</sup> Pore sizes of silica powder vary from 3.3 nm and 7.1 nm. Pores were only partially filled with perovskite nanocrystals slightly smaller than the pore size. In this investigation, the quantum confinement effect depending on the size of the in situ fabricated perovskites was observed.<sup>123</sup> The band gaps of nanoparticles increase with the shrinking of crystal size, and the PL peaks of nanocrystals are blue shifting with decreasing of crystal size. The perovskite PLQE was smaller than 6%, revealing that non-radiative decay rates increased with decreasing nanocrystal size. Following Malgras's research, Dirin et al. improved the PLQE of CsPbBr<sub>3</sub> perovskite nanocrystals in mesoporous

silica to more than 50% via nanocrystal surface passivation.<sup>124</sup> Synthesized perovskite/silica powder was stable to illumination with UV- and laser light. In Demchyshyn's research in 2017, they reported the synthesis of MAPbBr<sub>3</sub> and CsPbBr<sub>3</sub> perovskite in an aluminium oxide matrix.<sup>118</sup> Pores were also partially filled with spherical-like perovskite nanocrystals in rod-like pores. Quantum confinement effect was observed as blue shifted PL peaks comparing to bulk perovskites.

As described above, in situ growth approach provides an alternative way to the conventional colloid nanocrystal synthesis method, solving the poor conductivity of ligand assistant synthesized perovskite nanocrystals. The perovskite nanocrystal size could be tuned by controlling the matrix pore size. The Quantum confinement effect was observed in former research. The PLQE of perovskite remains relatively low, and the poor stability of perovskites is still a problem waiting to be solved. Besides, the conductivity of matrixes in the former investigation is not promising, making synthesized composites difficult to be advanced in the application. Therefore in this research, we used gallium nitride that has outstanding conductivity as a matrix<sup>125</sup>. We aim to prepare a perovskite/GaN composite that can advance in situ grown perovskite nanoparticles to actual application in optoelectronic devices.

Similar to bulk perovskites, the optical band gap and PL of perovskite nanocrystals can easily be tuned across the visible light spectrum by varying their cation and anion compositions.<sup>105,113,126</sup> Beyond that, the optical properties of methylammonium lead

halide perovskite change when moving from bulk crystals to nanocrystals due to the crystal size reduction.<sup>99,118,123</sup>

It has been demonstrated that colloid perovskite nanocrystals PLQE improves significantly with respect to their bulk counterparts when the crystal size is reduced to nanoscale.<sup>105,126–128</sup> The origin of the PLQE improvement is still under investigating<sup>129,130</sup>. One possible explanation for this phenomenon is that the larger surface to volume ratio and efficient ligand passivation of colloid nanocrystals remove surface traps, leading to less non-radiative recombination. Thus higher PLQE is achieved.<sup>129</sup>

Another significant consequence of crystal size reduction is the quantum confinement effect on the optical bandgap of perovskites. The quantum confinement effect on semiconductors has been discussed in Section 2.1.5. Due to the quantum confinement effect, the optical bandgap of perovskite nanocrystals can be tuned by changing the crystal size and shape. A smaller crystal size leads to a larger optical bandgap, corresponding to a blue shift in optical absorption or emission spectra compared to their bulk counterparts<sup>118</sup>. As a result of quantum confinement and dielectric confinement effects, the PLQE of perovskite nanocrystals approaches near-unity at relatively low excitation density. At higher excitation density, the Auger recombination occurs, including biexcitons, trions and trap-assisted nonradiative recombination, resulting in a less efficient radiative recombination process.<sup>131,132</sup>

In perovskite nanocrystals, both excitons and free charge carriers contribute to the radiative recombination process after photoexcitation.<sup>133</sup> The population of excitons and free charge carriers is determined by the exciton binding energy and the initial exciton concentration.<sup>133</sup> The multiexponential PL decay dynamics of most perovskite nanocrystals suggests the existence of sub-band-gap energy levels. These energy levels arise from various defects that act as trapping centres. Carriers on shallow defect levels can relax to the ground state via the radiative recombination process, while carriers on deep defect levels can only relax non-radiatively. Surface trapping arising from the high surface to volume ratio also facilitate nonradiative recombination process, leading to low PL efficiency.<sup>134</sup> Therefore, surface defect passivation is significant in realizing the optoelectronic applications of perovskite nanocrystals.

## **2.2.6 Moisture Stability of Metal Halide Perovskites**

Halide perovskites are remarkable candidates for light-emitting devices. However, their stability remains a challenge. Perovskites decompose rapidly under moisture exposure. In the ambient environment, water can penetrate through the perovskite lattice, forming hydrated perovskite phases. In hydrated perovskite phases, the organic species are mobilized and evolve, while the lead halides are more localized than organic species. Water molecules form strong hydrogen bonding with organic methylammonium cations and build up water-cation-water chains. As methylammonium can donate a proton to water, the bonding between the methylammonium and lead halide will be weakened.

Then the methylammonium cation can readily diffuse and separate from the lead halide backbone, leading to the decomposition of perovskites.<sup>135,136</sup>

Various approaches have been investigated to prevent the moisture induced degradation process. Making a 2D perovskite offers an approach to achieve stable perovskite structures in the moisture atmosphere.<sup>91,98,137,138</sup> Large organic cation layers can protect perovskite units from exposure to the ambient environment. Mohite et al.<sup>89</sup> demonstrated promising stability of 2D RP phase perovskite devices in 2016. They revealed that unencapsulated devices maintained 60% of their initial performance after 1000 hours of AM 1.5G irradiation in air. The encapsulated devices did not show any sign of degradation after 1000 h of illumination or 1000 h of exposure to 65% room humidity at room temperature. After that, more 2D perovskites have been studied and has shown outstanding stability than their 3D counterparts.<sup>139–141</sup>

Another efficient approach is to encapsulate halide perovskite in other materials. Encapsulation materials can prevent water in the air from contacting perovskites.<sup>135</sup>

Many investigations have been carried out on encapsulating perovskite with nanoporous structures, such as titania<sup>142</sup>, alumina<sup>118</sup>, silica<sup>124</sup> and silicon<sup>118</sup>. Via these approaches, perovskites remain stable on timescales ranging from 1 day to 1.5 months. These matrixes serve as encapsulation materials and essentially prevent the ingress of water. Therefore, the stability of perovskites inside is enhanced.

## 2.2.7 Photobrightening and Photodarkening in Lead Halide Perovskites

Researchers are looking for efficient approaches to reduce the non-radiative recombination process and improve charge transport to improve perovskite's performance. One promising route is the light soaking treatment in the ambient environment, known as the photobrightening process.<sup>143</sup> The photobrightening effect depends on various factors, making it a complicated phenomenon to understand. The mechanism of the photobrightening process is not fully understood yet. One common element of mechanisms is that charge carriers originating from photoexcitation or strong oxidation can instigate photochemical reactions with oxygen and water, as well as with other ionic species (including halides, vacancies).<sup>144-147</sup> During photochemical reactions, defect states are passivated, while the nature of the defect passivation process is still under debate.

In 2014, Stanks et al.<sup>148</sup> reported the increase in PL intensity from a MAPbI<sub>3</sub> thin film under extended illumination in ambient atmosphere and the concomitant improvement of MAPbI<sub>3</sub> solar cell performance under illumination in ambient atmosphere. This result suggests that the light soaking process can influence the relative fraction of non-radiative and radiative recombination paths. However, instead of a photobrightening process, photodarkening processes have been observed on similar materials under similar conditions. Gottesman et al.<sup>149</sup> demonstrated that an encapsulated MAPbI<sub>3</sub> thin

film undergoes a reversible PL decreasing over time under white light illumination, while the PL will recover in the dark. Although these phenomena appear to contradict each other, Anaya et al.<sup>150</sup> suggested a competition between the photobrightening and photodarkening process during illumination. That is because that the photobrightening process requires oxygen and other molecules such as water. However, oxygen, water and even light will degrade perovskites at the same time. Therefore, the photobrightening and photodarkening processes strongly depends on experimental conditions.

The light brightening effect also depends on the perovskite morphology and composition. deQuilettes et al.<sup>151</sup> used scanning electron microscopy (SEM) micrographs and confocal PL microscopy images to demonstrate that perovskite thin films with better initial quality exhibit less photoinduced changes. Similarly, Tian et al.<sup>152</sup> found that the PL of smaller perovskite grains enhances faster than large grains. Therefore, the photobrightening process is more efficient in low-quality perovskites.

Photobrightening effect has also been observed in alumina matrix confined perovskite nanocrystals. Demchyshyn et al.<sup>118</sup> observed the PL intensity of MAPbBr<sub>3</sub> nanocrystals in nanoporous alumina increases by roughly 40% to its initial intensity under ambient condition and then stay stable without PL shape change. They attribute the increase in PL to the photobrightening effect. With illumination and oxygen, defect states are passivated, and the non-radiative recombination process is therefore reduced

## 2.3 Gallium Nitride

### 2.3.1 Properties of Gallium Nitride (GaN)

The III-nitride family semiconductors (gallium nitride (GaN), indium nitride (InN) and aluminium nitride (AlN)) are semiconductors with direct bandgap various from UV to visible spectrum region. The bandgap of group III-nitrides is tuneable, ranging from 0.7 eV to 3.3 eV.<sup>153</sup> GaN is highly resistant to chemicals, and it is stable at high temperatures, making GaN devices possible to operate in a harsh environment.<sup>154</sup> At room temperature, the electron mobility of GaN is more than  $1000 \text{ cm}^2/(\text{V}\cdot\text{s})$ , which is 2-5 times the mobility of silicon. The breakdown strength of GaN can reach  $\sim 5 \times 10^6 \text{ V/cm}$ , which is ten times that of silicon.<sup>155</sup> These novel properties of GaN making it a promising candidate for light-emitting diodes and lasers, especially for blue light devices<sup>156</sup>. Due to the advantages of GaN, it is also possible to make micro GaN devices with high-frequency operation and low switch loss. In 1995, Nakamura's group developed the first blue LED based on a single InGaN quantum well.<sup>157</sup> GaN can be doped with silicon or oxygen to synthesise n-type GaN and magnesium to synthesise p-type GaN.

At room temperature, GaN has a wurtzite crystal structure, a stable hexagonal structure, or a zincblende structure, a metastable cubic structure.<sup>158</sup> GaN can possibly exist in rock salt crystal structures at high temperatures and high pressure.<sup>159</sup> In this thesis, all the GaN samples have the wurtzite crystal structure.

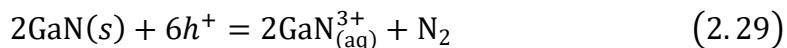
## 2.3.2 Forming Nanoporous GaN

Porous GaN can be prepared via electrochemical etching (ECE) and photo-electrochemical etching (PECE) methods.<sup>160</sup> ECE is an approach of etching a sample by applying a positive voltage with respect to a stable counter electrode in an electrolyte. PECE approach is similar to the ECE but with illumination support. These etching methods allow the formation of various pore morphologies for the surface and subsurface pores. In this thesis, all the porous GaN samples are prepared via ECE. Therefore, we will focus on introducing the ECE process in this section.

The basic setup for ECE etching includes an n-doped GaN sample to be porosified connecting to the anode, an inert counter electrode (usually platinum) connecting to the cathode, an electrolyte and an applied potential between the anode and the cathode. The electrode, electrolyte, applied potential can be adjusted to achieve the desired pore morphology. To form nanoporous GaN, the n-doped GaN is usually used as the anode due to its high conductivity and the challenge of effective p-doping. The n-doping density of the GaN layer can range from  $10^{18} \text{ cm}^{-3}$  to  $10^{21} \text{ cm}^{-3}$ . The doping density needs to be above a minimum value, as the corrosion reaction is electric field driven. Therefore, the sample needs to be conductive. The applied potential can be adjusted from 2 V to 40 V<sup>161</sup>. The electrolyte can be chosen from strong acid to strong base.

<sup>161,162</sup>

The oxidation of GaN is an electrochemical reaction driven by free holes<sup>163</sup>



The  $\text{GaN}_{(\text{aq})}^{3+}$  will then dissolve in the electrolyte. The ECE is a conductivity selective etching process, meaning only the doped GaN can be etched off while the undoped GaN will not be affected. Therefore, various porous GaN structures can be achieved via the ECE method, such as surface porosified GaN and nanoporous distributed Bragg reflector GaN.<sup>160</sup> The porous structure of GaN creates an opportunity to infiltrate perovskites inside to produce a composite material with promising optical properties.

### 2.3.3 Yellow band emission of GaN

GaN has a direct bandgap of  $\sim 3.4$  eV.<sup>164</sup> The reported conduction band offset (CBO) and the valence band offset (VBO) of GaN to bulk  $\text{MAPbBr}_3$  are  $1.39 \pm 0.12$  eV and  $0.13 \pm 0.08$  eV, respectively. Therefore, a type I heterojunction forms between GaN and  $\text{MAPbBr}_3$  perovskite.<sup>165</sup> At room temperature, the PL spectrum of GaN shows a band-edge emission at 365 nm and a broad yellow band emission at 575 nm<sup>166</sup>. The band-edge emission usually is entirely dominated by excitons at room temperature. The yellow band emission is a broad Gaussian-shaped emission and is a universal feature of GaN grown with various methods.<sup>167</sup> The yellow band emission is associated with deep-level transitions. The existence of the yellow band demonstrates the presents of defects, which have a negative effect on the carrier lifetime and the intensity of band-edge recombination. These defects arise from point defects such as Ga or N vacancies.<sup>166</sup> The vibronic structure of the yellow band reveals strong electron-phonon coupling.

However, the actual origin of the yellow band emission is being debated. Several theoretical studies proposed that transitions arise from shallow donors to deep acceptors or from deep donors to shallow acceptors.<sup>168</sup> As the pressure dependence of the yellow band is the same as the GaN bandgap, the yellow band is associated with the transition from a shallow donor state to a deep acceptor state.<sup>169</sup> However, the recombination process that originates the yellow band emission is not clear.



## Chapter 3 Experimental Methods

This chapter describes experimental methods we utilised to obtain results in Chapter 4, 5 and 6. It consists of three sections. The first section introduces sample preparation methods. The second section describes the structural and morphology characterisation techniques, including scanning electric microscopy and X-ray diffraction. The third section contains spectroscopy techniques we explored in this thesis, including steady-state absorption spectroscopy, steady-state luminescence spectroscopy, photoluminescence quantum efficiency measurement, hyperspectra microscopy, transient absorption spectroscopy, and microscope TCSPC.



## 3.1 Sample Preparation

### 3.1.1 Chemicals

Lead bromide ( $\text{PbBr}_2$ , 99.9999%), methylammonium bromide (MABr, 98%), lead iodide ( $\text{PbI}_2$ , 99.9999%), methylammonium iodide (MAI,  $\geq 99\%$ , anhydrous), (3-Aminopropyl)triethoxysilane (APTES, 99%), isopropyl alcohol (IPA, 99.9%), dimethylformamide (DMF,  $\geq 99.9\%$ ), Dimethyl sulfoxide (DMSO,  $\geq 99.9\%$ ), ethanol (anhydrous) and sulfuric acid ( $\text{H}_2\text{SO}_4$ , 95.0%-98.0%) were purchased from the Sigma Aldrich. These chemicals were utilized without further purification. Hydrogen peroxide ( $\text{H}_2\text{O}_2$ , 50w% solution in water) was purchased from Thermo Fisher Scientific. It was utilized without further purification. Bis(propargyl ammonium iodide) anthracene (BPAIA) was synthesized by John Anthony's group at the University of Kentucky. Dimethylammoniumnaphthalene (DMAN) was synthesized by Dr Forian Auras from the Optoelectronics Group at the University of Cambridge. Gallium nitride (GaN) was prepared by Dr Peter Griffin from the Cambridge Centre for Gallium Nitride. These materials were utilized without further purification.

### 3.1.2 Infiltration of $\text{MAPbBr}_3$ Perovskite into Porous GaN

There were two methods we utilised to infiltrate perovskite into a porous GaN matrix.

#### **Method 1: Infiltration of $\text{MAPbBr}_3$ into nanoporous GaN**

Porous gallium nitride (GaN) samples are prepared by collaborators from the Cambridge Centre for Gallium Nitride at the University of Cambridge.

After ultrasonic cleaned in acetone and IPA for 15 minutes separately, the GaN sample

was subjected to oxygen plasma at 50 W for 15 mins to render the surface hydrophilic. Then substrate was transferred into a nitrogen-filled glovebox, and all the deposition processes were carried out inside. Firstly, we dropped 30  $\mu$ l lead bromide ( $\text{PbBr}_2$ ) (DMF)/(DMSO) solution (1.0 M) on a GaN sample and left it undisturbed for at least one minute to soak into the porous surface. Then the sample was spun at 2000 rpm for 20 s to evaporate the solvent and a  $\text{PbBr}_2$  thin film formed. After that, the substrate was soaked in 0.1 M methylammonium bromide (MABr) isopropanol (IPA) solution undisturbed for 10-20 mins in a closed petri dish. This process is for the MABr to incorporate into  $\text{PbBr}_2$  thin film. We then use pure IPA washing off the excess MABr, following by 15-20 mins annealing at 80°C on the hotplate to crystallise perovskite.

#### **Method 2: Infiltration of $\text{MAPbBr}_3$ into APTES treated nanoporous GaN**

Nanoporous GaN substrate was ultrasonically cleaned in distilled water, acetone and isopropanol for 15 mins respectively. Then the substrate was dried at 500°C for three hours in the oven to minimise moisture inside nanopores. After cooling down to room temperature, the substrate was subjected to 15 mins oxygen plasma treatment at 50 W. We then soaked the GaN in the Piranha solution ( $\text{H}_2\text{SO}_4$  (98%):  $\text{H}_2\text{O}_2$ (30%) =3:1) for an hour, decorating the GaN surface with -OH groups. After washing off the excess Piranha solution with ethanol, the substrate was soaked in the APTES ethanol solution (v/v% = 1:10) overnight at 60°C.

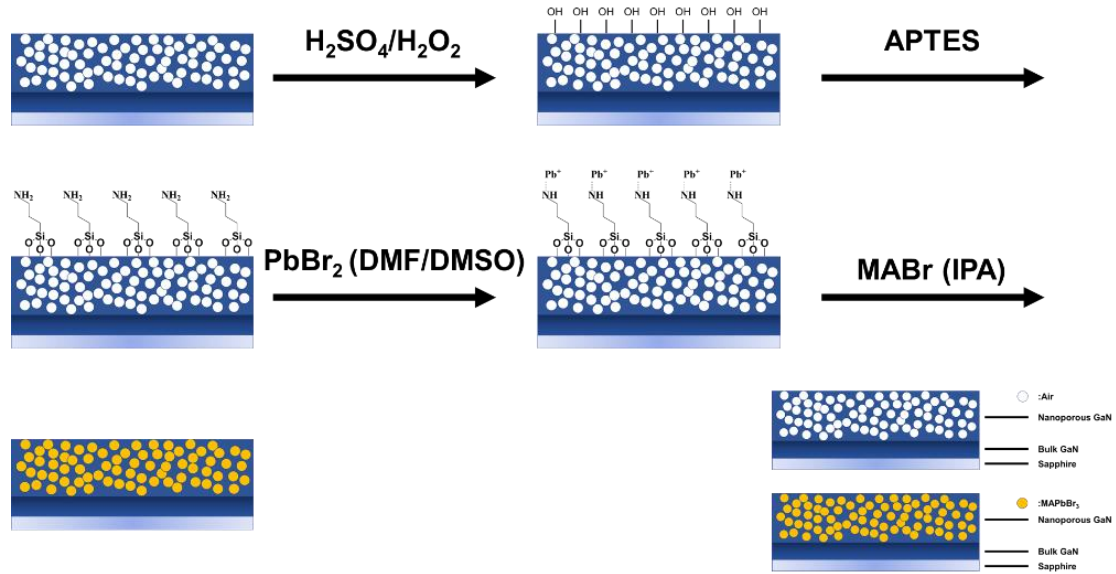


Figure 3-1 Illustration of the APTES treatment and MAPbBr<sub>3</sub> infiltration process.

Before the infiltration of perovskite, the treated substrate was cleaned with ethanol to get rid of the excess APTES at the substrate surface. The infiltration process was carried out in a nitrogen-filled glovebox to eliminate the influence of oxygen and water in the ambient atmosphere. A  $\sim 1 \text{ cm}^2$  treated substrate was soaked in 2 ml PbBr<sub>2</sub> DMF/DMSO (1 M) solution overnight. We used the DMF/DMSO solvent to wash off the excess PbBr<sub>2</sub> at the surface with a syringe and soaked the nanoporous GaN again into 2 ml MABr isopropanol (0.2 M) overnight. After another round of washing with IPA, the sample was annealed at 100°C for half an hour to crystallise MAPbBr<sub>3</sub> perovskite inside.

### 3.1.3 Preparation of MAPbBr<sub>3</sub> Thin Film

Quartz substrates were ultrasonically cleaned in acetone and IPA for 15 mins respectively. After being dried with a nitrogen gun, the substrate was subjected to 15 mins oxygen plasma treatment. MABr and PbBr<sub>2</sub> were mixed in a ratio of 1:1 in DMF

solution (0.2 M). 40  $\mu\text{L}$  solution was spin-coated on a quartz substrate at 3000 rpm for 60 seconds. Then samples were annealed at  $100^\circ\text{C}$  for 10 minutes. All precursors preparation and infiltration processes were carried out in the nitrogen-filled glovebox.

### **3.1.4 Preparation of Bis(propargyl ammonium iodide) anthracene (BPAIA) Lead Iodide 2D Perovskite**

30  $\mu\text{L}$   $\text{PbI}_2$  DMF solution (1 M) was spin-coated onto a quartz substrate at 2000 rpm for 30 seconds. Then the  $\text{PbI}_2$  thin film was annealed at  $100^\circ\text{C}$  for 15 minutes. After that, 30  $\mu\text{L}$  BPAIA DMF solution (0.4 M) was dropped onto the  $\text{PbI}_2$  thin film. After 30 minutes of undisturbed soaking at room temperature, the sample was annealed at  $100^\circ\text{C}$  for 15 minutes. All the solution preparation and sample synthesis processes were carried out in the nitrogen-filled glovebox. Via the two-step deposition method, we synthesized 2D perovskite crystals thin film with BPAIA.

### **3.1.5 Preparation of 2,6-dimethylammoniumnaphthalene (DMAN) Lead Iodide 2D Perovskite**

The DMAN was mixed with  $\text{PbI}_2$  at a 1:1 molar ratio in the DMF solvent (0.2 M). 30  $\mu\text{L}$  mixed solution was spin-coated on a quartz substrate at 5000 rpm for 60 s. Then the thin film was annealed at  $100^\circ\text{C}$  for 10 minutes. All the solution preparation and sample synthesis processes were carried out in the nitrogen-filled glovebox. Via the one-step

deposition method, we successfully synthesized 2D (DMAN)PbI<sub>4</sub> perovskite

### **3.1.6 Sample Encapsulation**

Samples for transient characterisation were encapsulated in the nitrogen-filled glovebox to reduce perovskite degradation when exposed to air and moisture. A thin glass coverslip was placed on top of the sample, and sample edges were sealed with epoxy.

## **3.2 Structural and Morphology Characterisation**

### **3.2.1 X-ray diffraction (XRD)**

X-ray diffraction is a technique to estimate the crystal structure and chemical composition of a material.

X-ray diffraction was measured with a Bruker X-ray D8 Advanced diffractometer with Cu K $\alpha_{1,2}$  radiation ( $\lambda=1.541$  Å). The incident beam slit width was 0.6 mm. Data was collected in an angular range  $2\theta$  of 5° to 55° with the angular resolution of 0.046°.

X-ray is electromagnetic radiation with a wavelength between 0.1 Å and 100 Å, which is similar to the interatomic distances in a crystal. In XRD measurement, monochromatic X-ray incidents onto the sample and interacts with atoms in the sample. The X-ray will be scattered by the material. The scattering by nuclei is negligible, as nuclei are so heavy that they hardly respond to the rapidly oscillating electromagnetic field. The electromagnetic field can interact with the electrons around the nuclei. When

electrons oscillate with the incident beam, they will re-emit the X-ray with the same wavelength and frequency as the incident beam. This process is called Thomson scattering. The intensity of the scattered radiation for free electrons  $I_{2\theta}$  depends on the power per unit solid angle scattered through a scattering angle  $2\theta$ <sup>170</sup>

$$I_{2\theta} = \frac{1}{2} \left( \frac{e^2}{4\pi\epsilon_0 c^2 m} \right)^2 (1 + \cos^2 2\theta) I_0, \quad (3.1)$$

in which  $e$  is the electron charge,  $\epsilon_0$  is the permittivity of the free space,  $c$  is the light speed,  $m$  is the electron mass,  $2\theta$  is the scattering angle, and  $I_0$  is the intensity of the incident radiation. The scattered radiation intensity of a single atom is negligible. However, the interfering X-ray scattering from multiple neighbouring atom layers is intense enough to be detected. The constructive interference of X-ray beam from neighbouring atom layers follows Bragg's law<sup>170</sup>,

$$2d\sin\theta = \lambda, \quad (3.2)$$

in which  $d$  is the distance between adjacent atom layers,  $\theta$  is half of the scattering angle, and  $\lambda$  is the wavelength of the incident X-ray beam. Due to the constructive interference of beams, the intensity of scattering X-ray is a function of  $d$ . Therefore, the structural information of the material can be extracted from the scattering angle  $2\theta$  and X-ray wavelength  $\lambda$ .

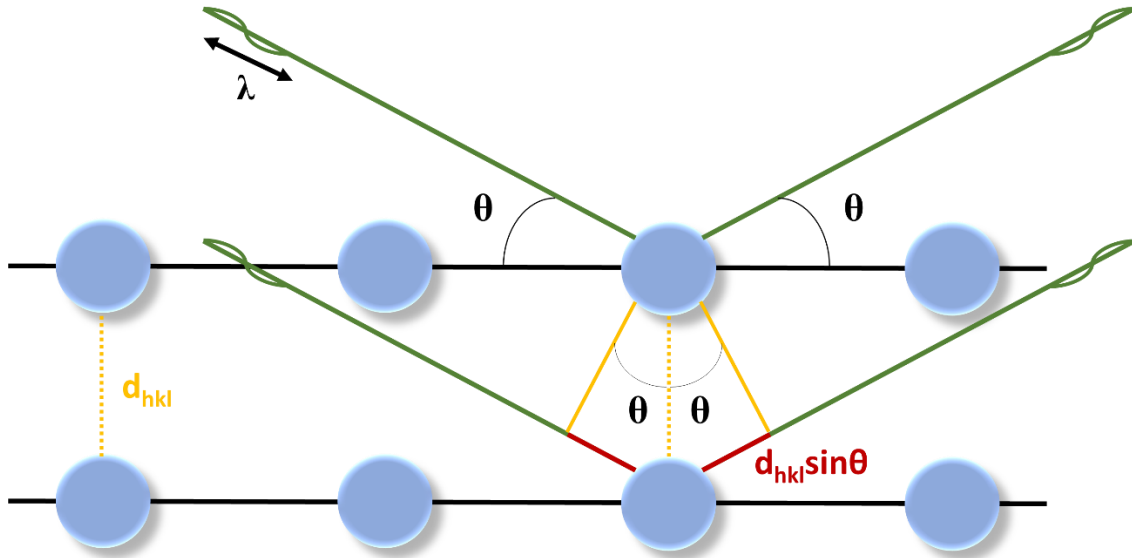


Figure 3-2 Bragg's law for constructive interference of two parallel X-rays after diffracting from the adjacent crystal planes.

### 3.2.2 Scanning electron microscope (SEM)

SEM was performed with a Zeiss LEO 1550 FE-SEM apparatus with a field-emission source operating at 2 kV acceleration voltage in the In-Lens mode. The sample was mounted onto an SEM stage with carbon tape to reduce the charge effect. Low beam voltage was utilised to minimise sample degradation caused by the electron beam.

SEM is a technique to capture the surface topography of materials at a resolution of around 10 nm. During the measurement, a fine electron beam is focused onto the material's surface and scans across the sample in a pattern of parallel lines. The electrons with energy various from hundreds eV to tens keV interact with the sample.

They are scattered elastically or inelastically by the sample. The scattered electrons are detected, and the information about the sample's surface topography could be

extracted.<sup>171,172</sup>

## 3.3 Spectroscopy

### 3.3.1 Steady-state absorption

Steady-state absorbance of samples was taken with a Shimadzu UV-3600 Plus spectrophotometer, which consists of three detectors: a photomultiplier tube (PMT) for ultraviolet and visible regions, an InGaAs detector and a cooled PbS detector for the near-infrared region. The whole wavelength range covers from 185 nm to 3300 nm with a maximum resolution of 0.1 nm.

The spectrometer detects the light intensity before and after passing through the sample and calculates the transmittance  $T$ . The transmittance  $T$  equals the ratio of light intensity after transmitting through the sample  $I_t$  and light intensity of the light beam intensity  $I_0$ .<sup>173</sup>

$$T = \frac{I_t}{I_0} \quad (3.3)$$

The Absorbance  $Abs$ , which is also known as the optical density (OD), can be calculated from the transmittance<sup>173</sup>

$$Abs = \log_{10} \frac{1}{T} \quad (3.4)$$

### 3.3.2 Steady-state photoluminescence (PL)

The steady-state photoluminescence (PL) of samples was measured with the Edinburgh Instruments FLS980 spectrofluorimeter. The spectrometer contains one R928P PMT

detector, measuring wavelength ranging from 200 nm to 870 nm with a dark count rate smaller than 50 cps at -20°C. The PL spectra were measured from 300 nm to 800 nm depending on the samples' emission wavelength. Samples were excited at various wavelengths by a 450 W xenon arc lamp depending on the absorbance of samples. The xenon arc light was focused onto a monochromator using an off-axis ellipsoidal mirror.

### **3.3.3 Photoluminescence quantum efficiency (PLQE)**

Photoluminescence quantum efficiency (PLQE) measurements were taken with the John de Mello method<sup>41</sup>. All samples were excited with a 405 nm continuous-wave (CW) laser at various power, and the emission was collected with an Andoe iDus DU490A Si detector

In 1997 John de Mello<sup>41</sup> published a paper about an improved experimental method to determine the external PLQE of materials. In that paper, he proposed to calculate the external PLQE based on three separate measurements. In the first measurement (Measurement A), laser incidents into an empty sphere, and only the laser signal ( $L_A$ ) is detected. In the second measurement (Measurement B), laser enters the sphere with the sample inside but not directly onto the sample. In this case, only a fraction ( $\mu$ ) of laser is absorbed by the sample and the leftover laser signal ( $L_B$ ) is detected.

$$L_B = L_A(1 - \mu) \quad (3.5)$$

In the third experiment (Measurement C), the laser shines directly onto the sample inside the sphere. A fraction of the laser will be absorbed by the sample, noted as  $A$ ,

while the rest  $(1-A)$  is either scatter to the interior sphere surface or reabsorbed by the sample  $(\mu)$ . The laser signal detected in Measurement C  $(L_C)$  is

$$L_C = L_A(1 - A)(1 - \mu), \quad (3.6)$$

in which

$$A = \left(1 - \frac{L_C}{L_B}\right) \quad (3.7)$$

The total detected photons in Measurement B are given by  $L_B + P_B$ . In Measurement C, the total detected photons contain both photons from the scattered laser light  $(1 - A) \cdot (L_B + P_B)$ , and the photons from the sample photoluminescence after excited by the laser  $\eta L_A A$ ,

$$L_C + P_C = (1 - A) \cdot (L_B + P_B) + \eta L_A A \quad (3.8)$$

Therefore, PLQE  $\eta$  can be written as

$$\eta = \frac{P_C - (1 - A)P_B}{L_A A} \quad (3.9)$$

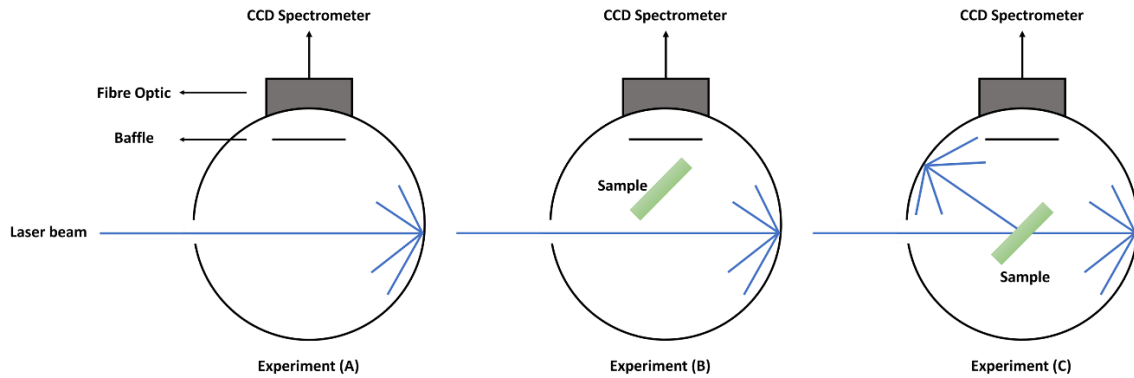


Figure 3-3 Illustration of three experiments of the PLQE measurement: (A) the empty measurement; (B) laser beam indirectly incident onto the sample; (C) laser beam directly incident onto the sample. Figures are adapted from reference (41).

### **3.3.4 Hyperspectra microscopy**

Hyperspectra images were measured using an IMA-VIS system (Photon etc.). Samples were measured using a 100× Nikon air objective and a 405 nm continuous wave laser or a 509 nm continuous wave laser with an excitation intensity of 100 mW/cm<sup>2</sup>. The spectra measurements are performed by scanning the angle of the grating relative to the emitted light from the sample to form images at each wavelength which are stacked to form a data cube. The spectra resolution is guided by the bandwidth of the holographic grating in the setup and is ~0.2 nm. For spectra measurement, we used 1 second integration time per wavelength and a step size of 2 nm across the wavelength window.

### **3.3.5 Time-resolved Photoluminescence Spectroscopy**

Transient photoluminescence spectroscopy measures the wavelength and number of photons at a certain time after excitation. In this thesis, we used two transient photoluminescence measurement techniques, time-correlated single photon counting (TCSPC) and an intensified charge-coupled device (ICCD), depending on the excitation laser power.

#### **Time-correlated Single Photon Counting (TCSPC)**

Samples were excited with a PicoQuant LDH407 laser diode at 407 nm with a repetition rate of 2 MHz at a fluence of  $7.37 \times 10^{-2} \mu\text{Jcm}^{-2}$  per pulse. The emission signal was selected with a monochromator to get the desired wavelength and detected by a Hamamastu R3809U-50 photomultiplier detector. Colour filters were utilised to remove

the scattered photons from the excitation laser. A neutral density filter was used to ensure that no more than one photon was detected in every photoexcitation cycle.

TCSPC precisely measures the timed registration of single photons repetitively.

Therefore, photoluminescence lifetime can be extracted from the result. This technique is based on the assumption that the probability distribution of emitted single photons after photoexcitation equals the intensity of all the photons emitted at various times after excitation. It uses the excitation pulse as a reference for the timing. When an optical pulse is generated, an electrical pulse correlating in time is triggered. When the sample starts emitting photons, the electrical pulse triggers a capacitor to start charging.

Photoexcited photons pass through a small aperture which only allows a maximum of one photon to pass through for every photoexcitation cycle. When a photon reaches the detector, the capacitor stops charging. The charge is then recorded. The charge is proportional to the time it takes for photons to reach the detector. After repeating the photoexcitation cycle multiple times, a histogram of counts at different time bins is built up and photoluminescence lifetime is recorded. However, TCSPC only detects photons at a specific wavelength each time.

## **Intensified charge-coupled device (ICCD)**

Samples were excited by a femtosecond laser generated from second harmonic generation (SHG) of a fundamental Ti: sapphire Spectra-Physics Solstice laser source (Wavelength 800 nm, pulse with 80 fs) with a  $\beta$ -barium borate crystal, at a repetition rate of 1 kHz. The excitation laser wavelength is 400 nm. The photoluminescence of

samples was detected by an electrically-gated intensified charge-coupled device (ICCD) camera (Andor iStar DH740 CCI-010) and a calibrated grating spectrometer (Andor SR303i). The gate used in this research is 4 ns. A 425 nm longpass filter was used to remove the scattered laser signal.

For another excitation wavelength (350 nm), TOPAS optical parametric amplifiers (OPA) was utilised as the primary pump source. TOPAS OPA generates near-IR (1100 nm-1200 nm) laser pulses, which will then be frequency-doubled, quadrupled or summed with the 800 nm fundamental laser pulses to produce narrowband laser pulses at a wavelength from 290 nm to 2000 nm.

An intensified CCD camera is used in ICCD measurement to detect the energy and number of photons emitted by samples at a particular time after photoexcitation. Compared with CCD cameras, the ICCD camera can reduce the read noise by exploiting gain while achieving a fast gate time with an image intensified tube. The image intensifier tube consists of a photocathode, microchannel plate (MCP) and a phosphor screen in a vacuum chamber. The photocathode, which is used to capture incident photons, is coated on the inside of the output window. When an incident photon hits the photocathode, a photoelectron is generated. It is then accelerated in an electric field towards the MCP. The MCP contains a 1 mm thick disk carved with a 6-10  $\mu\text{m}$  honeycomb glass channel, while each channel is coated with a resistive coating. A high voltage is applied to accelerate photoelectrons with high energy to one of the glass channels in the disc, releasing secondary electrons from channel walls. These electrons

will further be accelerated, generating an electron cloud departing from the MCP. Therefore, the original signal is amplified, and 200 gains are easily achieved. The degree of amplification is determined by the gain voltage applied across the MCP. The sensitivity of the ICCD is governed by the image intensifier tube. Consequently, the noise level is also determined by the image intensifier. The thermally generated charge in the photocathode will also be amplified, resulting in a dark current.

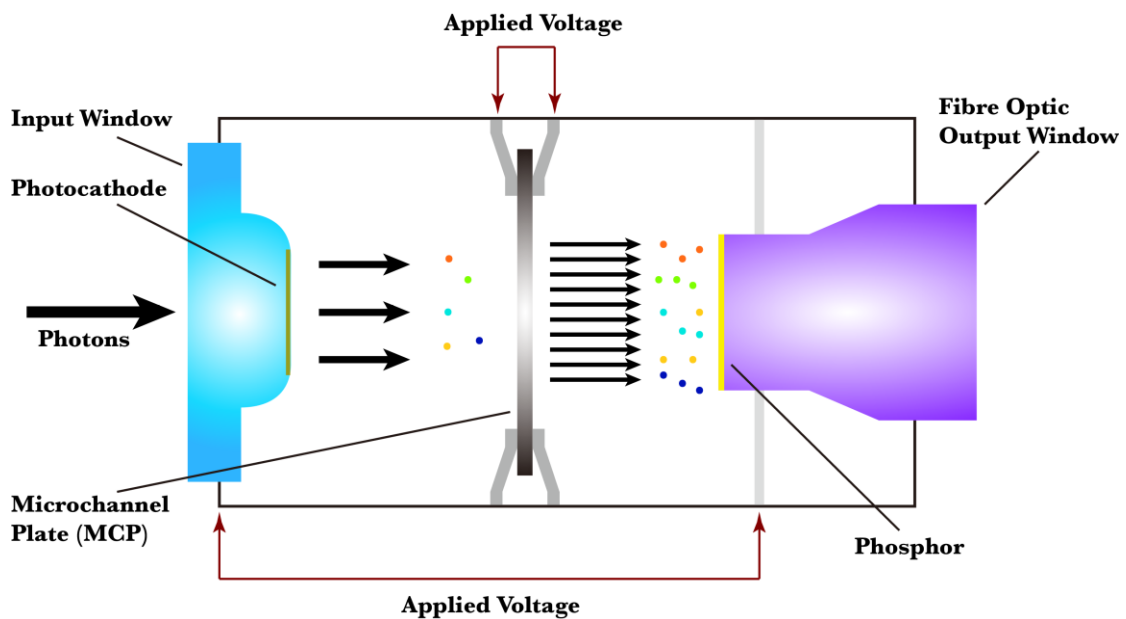


Figure 3-4 Configuration and working principle of an image intensifier tube in the ICCD. Colourful spots represent photoelectrons with different energy.-Figure kindly supplied by Dr Jiale Feng.

The optical shuttering property is the main advance of ICCD comparing to CCD. By operating at a very fast optical switch, the image intensifier can capture optical signals on a nanosecond scale. The intensifier can be gate-on or gate-off via applying negative voltage or positive charge. The minimum gate time is defined by the minimum time it

takes to switch the intensifier from off to on then to off again. The minimum gate time of the ICCD in this study is 4 ns.

### 3.3.6 Transient Absorption (TA)

Transient absorption (TA) spectroscopy is a technique to study the transmission difference of a material before and after photoexcitation as a function of time. Ultrafast TA can measure the transmission difference within a femtosecond timescale. At  $t = 0$ , a monochromatic short laser pulse arrives and excites the sample. This laser pulse is known as the pump beam. At  $t = \tau$ , a broadband laser pulse arrives at the same position as the pump. This laser pulse is known as the probe beam. A reference probe beam also incidents on to a different region on the sample, and it is used to correct the shot-to-shot probe differences. The transmission of the probe will be measured with photoexcitation ( $T_{pump\ on}$ ) and without photoexcitation ( $T_{pump\ off}$ ). The photoexcitation process is controlled by a beam chopper. The change in probe intensity is normally expressed as the differential transmission

$$\frac{\Delta T}{T} = \frac{T_{pump\ on} - T_{pump\ off}}{T_{pump\ off}}, \quad (3.10)$$

in which  $T$  is the intensity of the probe beam.

The main characters of a TA spectrum include:

The ground state bleach (GSB): When the pump beam excites species from the ground state to the excited state, the decrease in the population of species on the ground state leads to a reduction in probed absorption. Therefore, it shows as a positive signal in the

TA spectrum.

The stimulated emission (SE): The pump disturbs the electric field of an excited state, leading to a radiative emission of a photon that is difficult to be distinguished from the probe. Therefore, it shows as a positive signal in the TA spectrum.

The photoinduced absorption (PIA): The already photoexcited states lead to new absorption transitions, revealed as a decrease in  $T_{pump\ on}$ . It shows as a negative signal in the TA spectrum.

In addition to these three main characters, other photophysical processes can also be detected by the TA, such as many-body effects, electroabsorption and thermal effect etc.

TA measurement was carried out with laser beams generated from a Ti: sapphire amplifier system (Spectra Physics Solstice Ace). This output system generates  $\sim 100$  fs pulses at a repetition rate of 500 Hz centred at 800 nm, and the output power is  $\sim 3.5$  W.

The fundamental beam was split into two beam paths, the pump path and the probe path.

The 340 nm pump beam was generated in a homebuilt non-collinear optical parametric amplifier (NOPA). The 800 nm fundamental beam was sent into the NOPA to generate a 700 nm laser first, and the 700 nm beam was frequency-doubled to 350 nm in a beta barium borate (BBO) crystal (INGCRYS Laser Systems, thickness = 0.2 mm,  $\theta = 29.2^\circ$ ).

The 400 nm pump beam was generated via doubling the frequency of the 800 nm fundamental laser beam through a beta barium borate (BBO) crystal (Eksma Optics, thickness=1 mm). In the probe beam path, the fundamental 800 nm beam passed through a mechanical delay stage (Thorlabs DDS300-E/M) and then focused onto a

calcium fluoride crystal (Eksma Optics, thickness=5 mm) to generate the ultraviolet-visible broadband probe beam (330 nm-700 nm). After passing through the sample, the probe beam was collected with a monochrome line scan camera (JAI SW-4000M-PMCL, spectrograph: Andor Shamrock SR-163).

### **3.3.7 Microscope TCSPC**

The local transient PL was measured with a confocal microscope setup (PicoQuant, MicroTime 200). 405 nm and 510 nm pulsed laser diodes (PDL 828, PicoQuant, pulse width of around 100 ps) were used as the excitation source. The emission signal was separated from the excitation beam with a dichroic. After passing through a 50  $\mu\text{m}$  pinhole, the emission signal was collected with a Hybrid PMT detector connected to a Picoquant acquisition card for TCSPC (time resolution of 100 ps). An additional 520 nm longpass filter or 500 nm shortpass filter was utilised depending on the measurement. The repetition rate of the excitation source was 1MHz.

TRPL was measured using a confocal microscope setup (PicoQuant, MicroTime 200). The sample was excited with a 405 nm pulsed diode (PDL 828, PicoQuant, pulse width  $\sim$  100 ps). Signals were focused onto a Hybrid PMT detector connected to a Picoquant acquisition card for TCSPC (time resolution of 200 ps).



# Chapter 4 Infiltration of Perovskite into Nanoporous Gallium Nitride

Metal halide perovskite is one of the most promising materials for the next generation optoelectronic application due to its solution processability and excellent semiconductor properties. However, their poor chemical and structural stability in the ambient environment have hindered their application. In this chapter, we demonstrate a solution-processed method to infiltrate methylammonium lead bromide perovskite (MAPbBr<sub>3</sub>) into a nanoporous gallium nitride (GaN) matrix. The MAPbBr<sub>3</sub>/GaN composite solid preserved green light photoluminescence. We observed that the GaN matrix prevents perovskite from light-induced degradation for five hours in the ambient environment, and perovskite was stable after one-year storage in the ambient atmosphere. Our infiltration method has the potential to be generalised to related perovskite materials, offering a route to producing composites of interest for use in optoelectronic devices for light-emitting applications.



## 4.1 Background and Motivation

Metal halide perovskites have been regarded as one of the most distinctive next-generation luminescence materials due to their advanced properties, such as colour tunability, high quantum efficiency, narrow emission, and affordable solution processability. These superior qualities make it possible to create low price perovskite light sources with a wide colour range, low power supply and high colour purity. In the former investigation, various impermeable matrices with better stabilities, such as nanoporous silicon<sup>118</sup>, silica<sup>124</sup>, alumina<sup>174</sup> and titania<sup>142</sup>, were utilised to protect perovskites from degradation, as well as introducing quantum confinement to perovskites. These mesoporous matrices offer a promising alternative approach to colloidal nucleation and growth method in controlling semiconductor crystal size at the nanoscale. However, the poor electronic conductivity of some mesoporous matrices (for example, silica) precludes their application in electronic devices.<sup>124,175</sup> Charge transport through the composite solid is determined by the conductivity of the matrix. Therefore, a mesoporous matrix with promising charge transport property should be utilised to achieve high efficiency light-emitting devices.

Gallium nitride (GaN) is an encouraging inorganic semiconductor applied in light emitting devices in recent years. GaN has a direct bandgap in the UV region, and it has promising chemical and thermal stability, as well as novel electron and thermal conductivity. GaN is outstanding in light emission in the UV and blue region. However,

it is less effective for longer wavelength emission. Recently the porosification of epitaxial GaN by selective electrochemical etching of highly doped GaN layers has been demonstrated by Rachel Oliver's group<sup>160</sup>. This technique introduces an opportunity to infiltrate perovskites into the nanoporous GaN to form a composite light emitting material. Via combining perovskite and GaN, the potential for excellent colour tuning and high modulation bandwidths would be fulfilled, enable applications in solid-state lighting and visible light communication.

In this chapter we present a low-temperature solution processing measurement to infiltrate MAPbBr<sub>3</sub> into the nanoporous GaN. We chose MAPbBr<sub>3</sub> as a model perovskite because of its bright emission in the visible region and its high absorption coefficient in the near UV region ( $10^5 \text{ cm}^{-1}$ ). We optimize the infiltration method with GaN surface treatment and study the infiltration degree with elemental mapping and absorption measurement. We demonstrate GaN's protective effect on MAPbBr<sub>3</sub> perovskite with steady-state photoluminescence.

## 4.2 Results and Discussion

### 4.2.1 Morphology of the Nanoporous GaN Matrix

Nanoporous GaN templates are prepared via electrochemical etching a GaN epitaxial layers grown on sapphire substrate in 0.25 M aqueous oxalic acid electrolyte, as shown in Figure 4-1. Applying a constant potential difference between the GaN sample and a platinum counter electrode, the silicon-doped GaN layers are selectively etched while the undoped GaN remains due to their difference in conductivity. When various etching voltages are applied, different pore sizes and shapes can be achieved.

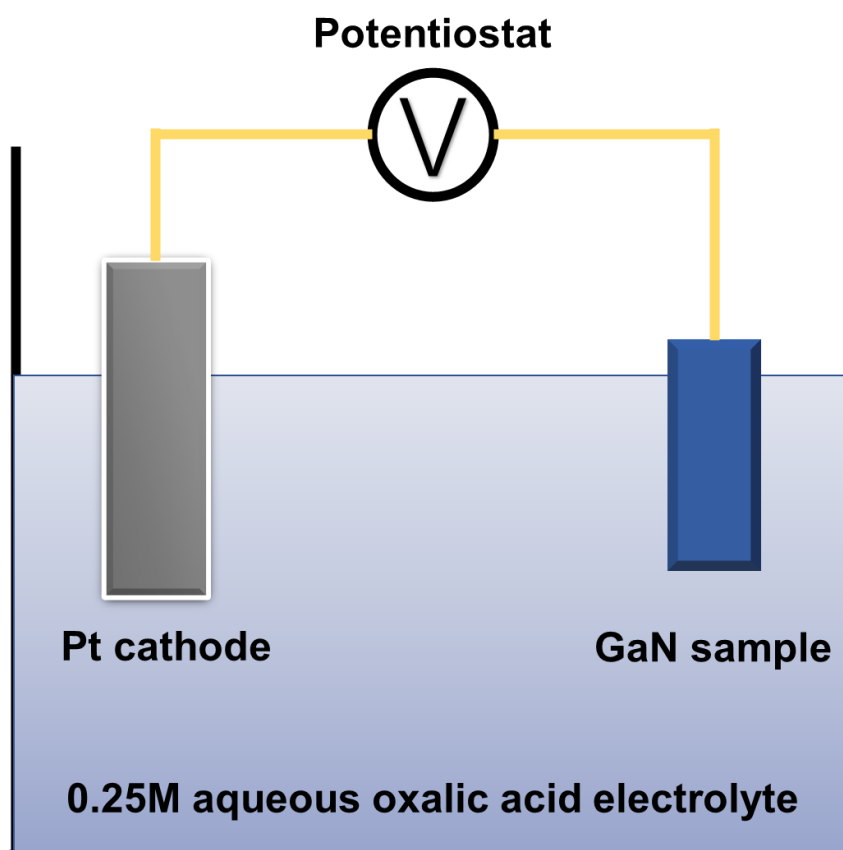


Figure 4-1 Illustration of the electrochemical etching process of a GaN epitaxial sample.

We observed the difference in surface porosity of GaN samples etched at various voltages with scanning electron microscopy (SEM) (Figure 4-2). When the doped GaN is etched at 6 V relative to the Pt counter electrode, a pitted surface with many shallow round pores with diameters ranging from 11 nm to 14 nm forms. Several elongated pores merging from two round pores (long dimension 17-26 nm) will also form. When the etching voltage increases to 8 V, denser pore coverage with a larger diameter (14-17 nm) forms. Asymmetric pores of various sizes (long dimension 40-80 nm) and shapes merging from more pores also forms. When reaching 10 V etching voltage, an open and connected pore morphology is created. Only a few round pores (diameter 16-20 nm) are produced, while the majority is an irregular-shaped porous network with deeper voids and channels with various length scales ranging from 100 nm to 200 nm tunnelling through the sample. As etching below 6 V hardly produces noticeable porosification, and above 12 V leads to compromised integrity of the porous layer, we used 6 V etched GaN (6 V GaN), 8 V etched GaN (8 V GaN) and 10 V etched GaN (10 V GaN) as templates in this investigation. The porous layer thickness of samples used in this thesis is about 500 nm, and the porosity is about 30% for 8 V etched GaN.

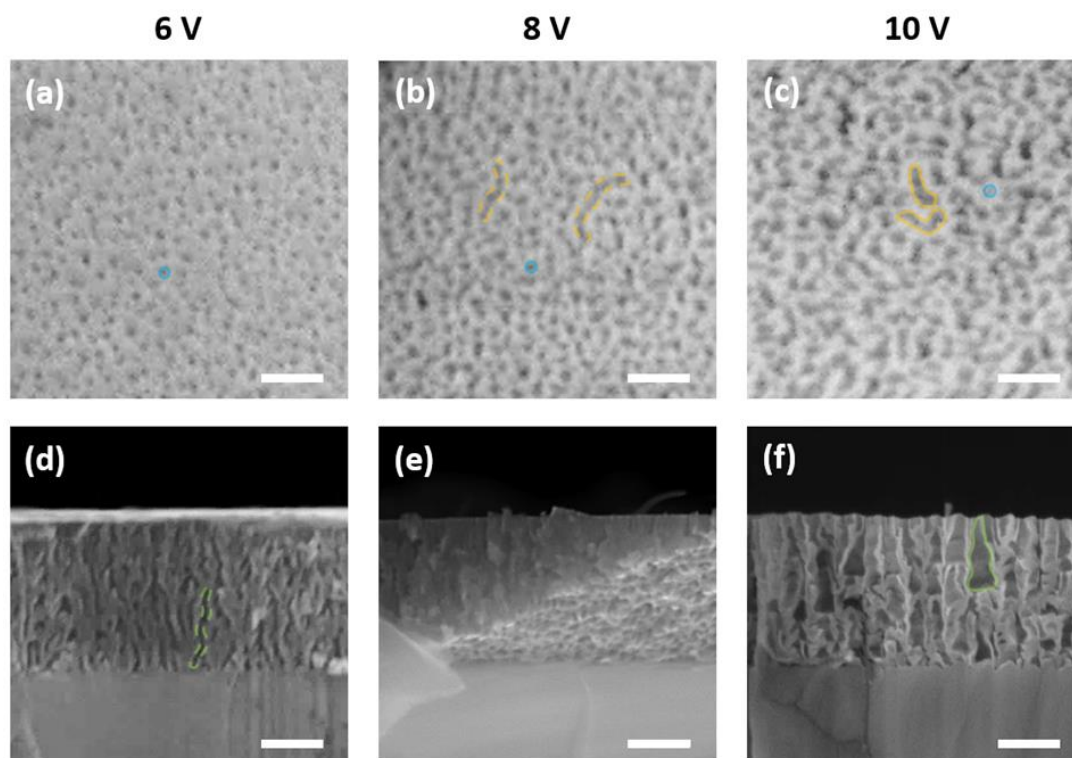


Figure 4-2 Scanning electron microscopy (SEM) image of porous GaN etching at 6 V [(a) and (d)], 8 V [(b) and (e)] and 10 V [(c) and (f)]. Scale bars: [(a)-(c)] 100 nm; [(d)-(f)] 200 nm. [(a)-(c)] Topview of porous GaN taking at 45° tilt angle, dark spots refer to pores patching on a bright background. With the increase of the etching voltage, pores (blue outline) grow larger and merge with other pores (orange outline), giving longer and asymmetric pores. [(d)-(f)] Cross-section image of the cleaved edges of the etched GaN layer on top of an unetched NID GaN layer. Etching at 6 V (d), the pores extend vertically into isolated channels (green outline); while etching at higher voltage (f), lateral etching takes place forming a porous network with large open pockets (green outline). The honeycomb appearance of 8 V etched GaN is due to a slope angle cleavage, making it difficult to observe the vertical channel. SEM was taken by Peter Griffin.



Figure 4-3 Illustration of the cross-section of nanoporous GaN samples utilised in this research. GaN samples consist of a nanoporous GaN layer, a bulk GaN layer and a sapphire layer.

The porosification of epitaxial GaN opens up the possibility to infiltrate solution-processed material, such as perovskites, inside the pores. This composite may offer a solution to make up GaN's poor emission in the green and red region, achieving more efficient solid-state light-emitting. In this research, the nanoporous GaN samples were prepared by Peter Griffin in the Department of Materials at the University of Cambridge.

## 4.2.2 Optical Properties of the Nanoporous GaN Matrix

The optical properties of GaN are independent of the etching voltage. Therefore we used 8 V etched GaN (8 V GaN) for all the measurements in this section. We took the steady-state UV-visible absorption spectroscopy and photoluminescence spectroscopy of the pristine nanoporous GaN, shown in Figure 4-4.

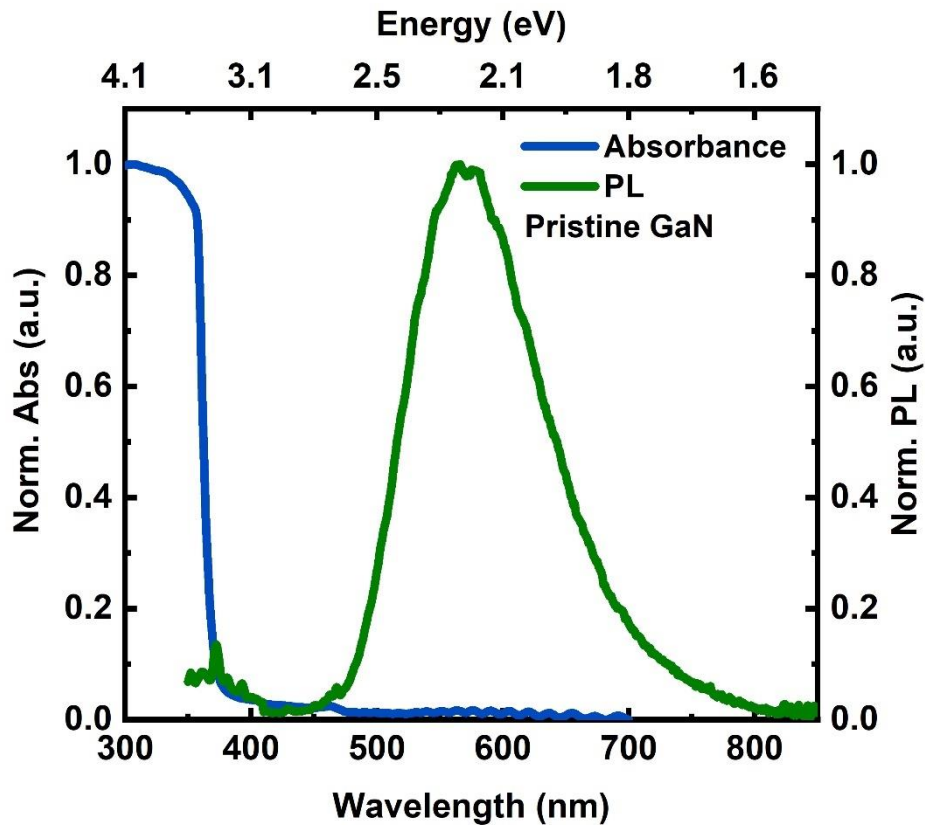


Figure 4-4 Normalised steady-state absorbance and photoluminescence of the pristine 8 V etched nanoporous GaN sample. Blue line: normalised absorbance taken with UV-Visible absorption spectrometer. The wavy character from 500 nm to 700 nm results from light interference in the sapphire layer. Green line: normalised photoluminescence of the pristine nanoporous GaN exciting at 300 nm from the GaN side with a Xe lamp. Two emission peaks are revealed. One is the blue band emission at 369 nm, originating from the band-to-band recombination; the other is the yellow band emission at 572 nm, the origin of which is controversial.

As shown in Figure 4-4, the 8 V GaN shows a sharp absorption edge at 369 nm (3.36 eV). When the sample is excited at 300 nm (4.13 eV), a blue band emission at

369 nm (3.36 eV) and a yellow band emission at 572 nm (2.17 eV) are detected. The blue band emission has a minimal Stokes shift to the absorption edge, and it originates from band-to-band charge carriers transfer<sup>167</sup>. The very broad yellow band emission centering at 572 nm (2.17 eV) has a broad full width at half maximum (FWHM) of 103 nm. The Stokes shift of the yellow band emission to the absorption edge is very large, about 203 nm (1.19 eV), suggesting the formation of a wide range of states below the conduction band of GaN.

When excited at lower photon energy than GaN's band edge, the nanoporous GaN no longer gives the broad yellow band emission. Figure 4-5 is the excitation scan of the yellow band photoluminescences detected at three wavelengths, 500 nm, 570 nm and 650 nm. According to the excitation scan, when the nanoporous GaN is excited at a wavelength longer than 375 nm, the yellow band photoluminescence disappears. As the excitation scan at various detector wavelengths is similar, we suppose the yellow band emission originates from the same recombination mechanism. There are various models to explain the recombination mechanism of the yellow band emission in former research. The below bandgap emission has been observed in undoped and doped GaNs, regardless of the growth method.<sup>176,177</sup> Former study states that a complex defect level forms due to gallium vacancies, and the broad yellow band arises from the transition from a shallow donor to a deep acceptor located at about 1 eV above the valence band (VB).<sup>176,178,179</sup> However, there is no conclusion for the origin of the yellow band

emission yet.<sup>180</sup>

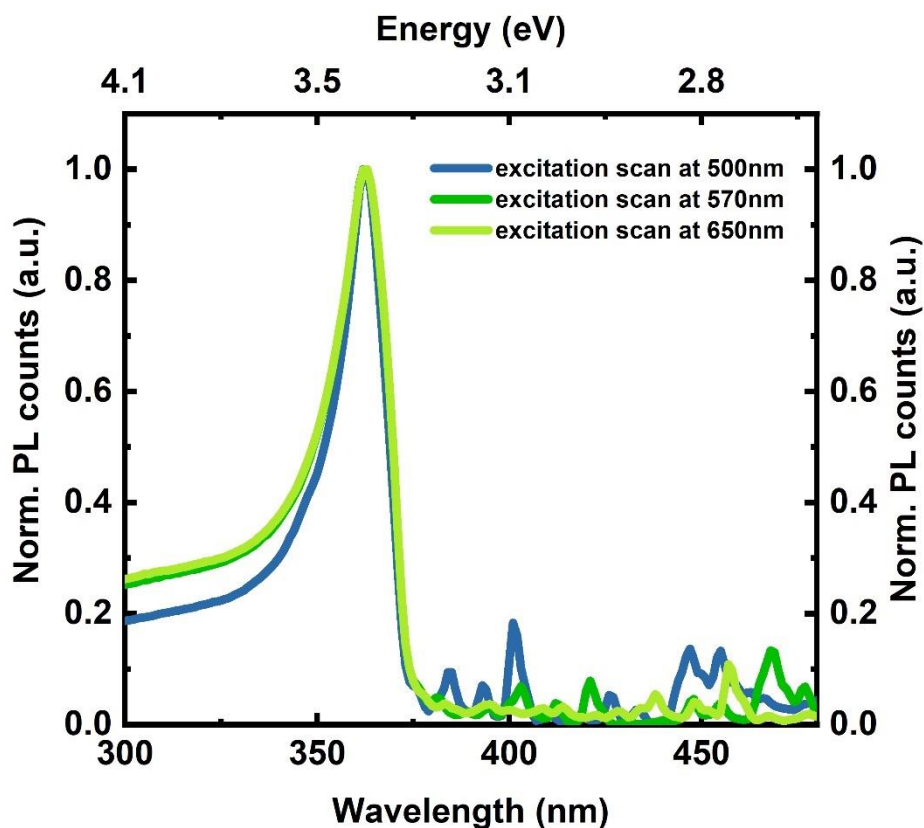


Figure 4-5 Normalised excitation scan of the pristine 8 V etched nanoporous GaN detecting at 500 nm (blue line), 570 nm (dark green line) and 650 nm (light green line). The GaN sample was excited with a Xe lamp from the GaN side from 300 nm to 500 nm. The photoluminescence was taken with a fluorimeter. The excitation scan at various detector wavelengths is similar, suggesting the broad band emission originates from the same recombination mechanism.

We then took the transient absorption (TA) of the pristine 8 V GaN to investigate the carrier dynamics. The nanoporous GaN was excited at 350 nm (3.54 eV) with femtosecond pulses laser (pump repetition rate = 500 Hz, pulse width ~ 100 fs) and was

probed with a white-light supercontinuum probe beam with a wavelength ranging from 350 nm to 600 nm. TA spectra of the 8 V GaN are shown in Figure 4-6. Immediately after the photoexcitation (0 ps), a positive signal, i.e. ground state bleach (GSB) signal, is observed at 375 nm (3.30 eV), consistent with the absorption bandedge of GaN. We attribute this to the depopulation of the ground state of GaN. The sharp GSB peak cut-off at 373 nm (3.32 eV) is due to the poor transmission of the probe beam through the GaN sample, as the absorption of GaN is intense in the high-photon-energy region above 373 nm.

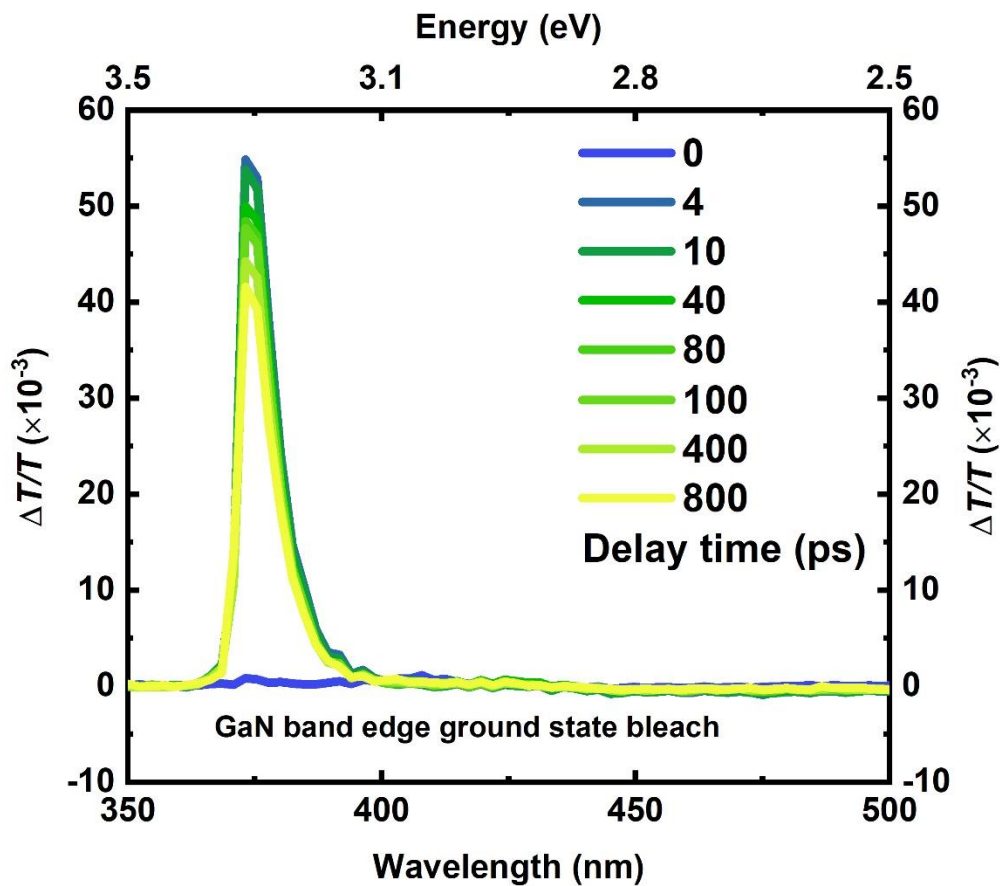


Figure 4-6 Transient absorption spectra of an 8 V etched nanoporous GaN at before time zero and after excitation. The sample was pumped with pulses of 3.54 eV energy (350 nm) with a pulse length of 200 fs at the ambient atmosphere. The sample was probed with a white-light supercontinuum beam from 350 nm to 500 nm. The fluence is about  $2 \mu\text{Jcm}^{-2}$  per pulse. TA spectra reveal a positive GSB signal at 375 nm (3.30 eV), consistent with the absorption band edge of GaN. The TA measurement was carried out jointly with Linjie Dai.

In addition, TA spectra (Figure 4-7) present a negative photo-induced absorption (PIA) signal at photon energy below the GSB ranging from 450 nm (2.75 eV) to 575 nm

(2.16 eV). The wavelength range of the PIA signal overlaps the yellow band emission of GaN. Previous studies attributed the yellow band emission to the shallow defect states caused by gallium vacancies<sup>176,178,179</sup>. Based on this statement, we would expect to observe a GSB below the bandgap from the TA spectrum since defect states are also expected to be populated after photoexcitation, indicating a GSB signal. However, instead of a positive GSB, a negative PIA signal is observed. This could indicate the formation of new electronic states in the sub-bandgap region due to photoexcitation, i.e., self-trapping excitons(STE).

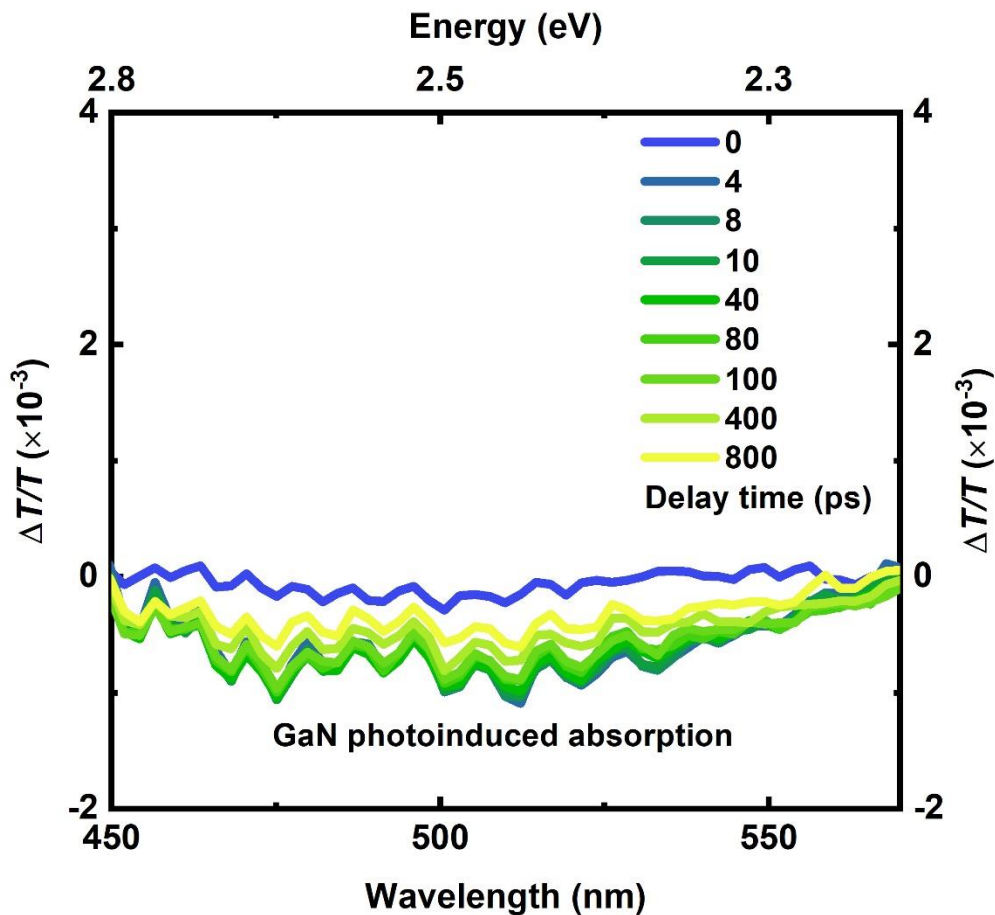


Figure 4-7 Transient absorption spectra of an 8 V etched nanoporous GaN at before time zero and after excitation. The sample was pumped with pulses of 3.54 eV energy (350 nm) with a pulse length of 200 fs at the ambient atmosphere. The sample was probed with a white-light supercontinuum beam from 450 nm to 575 nm. The fluence is about  $2 \mu\text{Jcm}^{-2}$  per pulse. TA spectra reveal a broad negative PIA signal, overlapping with the yellow band emission of GaN. The TA measurement was carried out jointly with Linjie Dai.

We compare the rise time and decay time at three probe wavelengths in Figure 4-8. The

intensity of the PIA keeps accumulating to about 500 fs after excitation, corresponding to the charge transfer from the band edge to the self-trapping state. The almost identical kinetics suggest the new self-trapping states formed simultaneously, and recombination dynamics are the same. According to the steady-state absorbance (Figure 4-4), the optical absorption below the bandgap region is negligible. As the STE spectrum overlaps with the yellow band emission of GaN when excited above its bandgap, we propose that based on the TA study, a self-trapping emission happens at an early time after photoexcitation, which could also contribute to GaN's yellow band emission in addition to the reported defect level emission in literature.<sup>166-169</sup> Future work should be carried out with more transient characterisation to identify the recombination process.

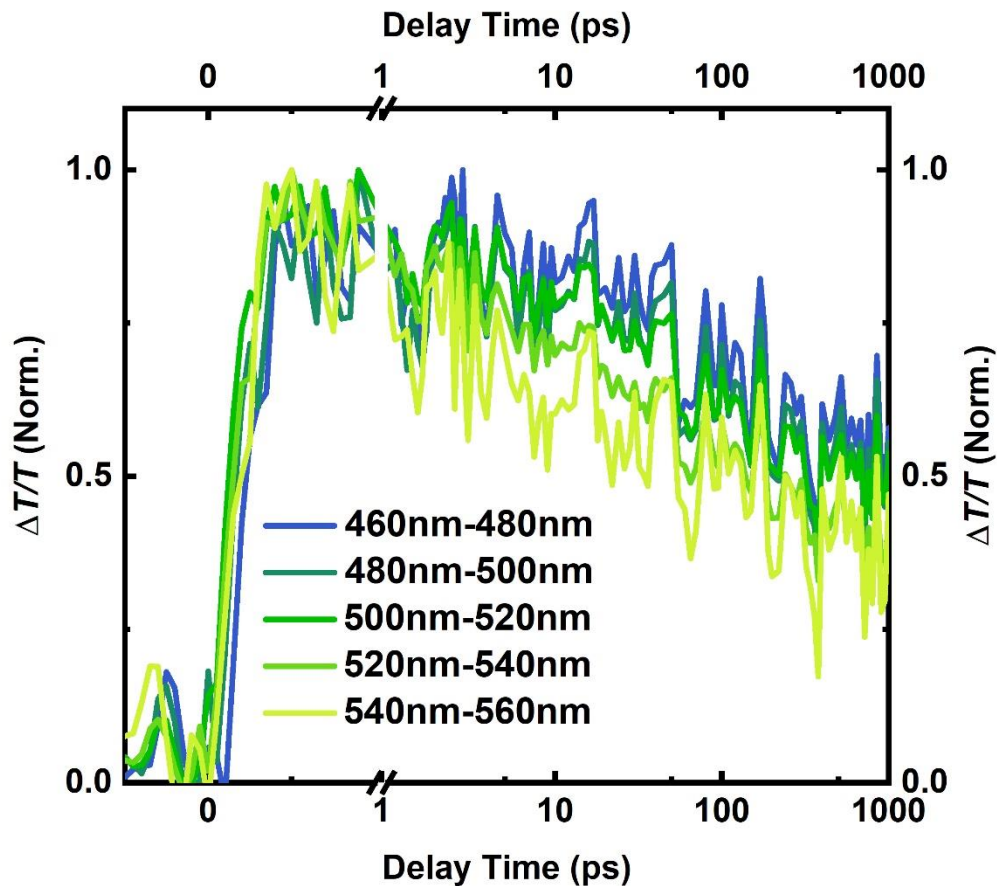


Figure 4-8 Transient absorption kinetics probed at various wavelengths of an 8 V etched nanoporous GaN before time zero and after excitation. The sample was pumped with pulses of 3.54 eV energy (350 nm) with a pulse length of 200 fs at the ambient atmosphere. The sample was probed with a white-light supercontinuum beam from 450 nm to 575 nm. The fluence is about  $2 \mu\text{Jcm}^{-2}$  per pulse.

### 4.2.3 Infiltration of MAPbBr<sub>3</sub> into Nanoporous GaN

As we discussed in Section 4.2.1, the porous GaN can be used as a matrix to contain other light-emitting materials. We chose methylammonium lead bromide perovskite

(MAPbBr<sub>3</sub>) as a suitable model perovskite in this work, as it emits strongly in the visible spectrum and high absorption coefficient in the UV to blue region. It can make up GaN's weak emission in the green light region. We found that via the two-step deposition method described in Section 3.1.2 Method 1 in Chapter 3, MAPbBr<sub>3</sub> can be infiltrated into the porous GaN.

In this study, we started from the commonly used one-step deposition method to infiltrate perovskite into nanopores. Normally perovskite will crystallise from a solution mixed from two precursors onto a substrate or in a template directly. However, evenly filled pores and discontinuous film cannot be produced via the one-step deposition method. That's because the formation enthalpy of perovskite is low.<sup>181</sup> Consequently, perovskite nanocrystals form in the colloidal perovskite precursor solution, blocking pores near the surface and hindering the further infiltration of perovskite into the pores. Therefore, we moved on to the two-step deposition method.

The sample preparation in this section was carried out jointly with Kevin T. P. Lim.

#### **4.2.4 Elemental Study of the MAPbBr<sub>3</sub>/GaN system**

We investigated the system's structure by preparing a cross-sectional TEM lamella for tandem scanning transmission electron microscopy via a focussed ion beam (FIB) microscope and energy dispersive X-ray spectroscopy (STEM-EDX) studies. The HAADF STEM image was taken by Boning Ding from the Department of Materials.

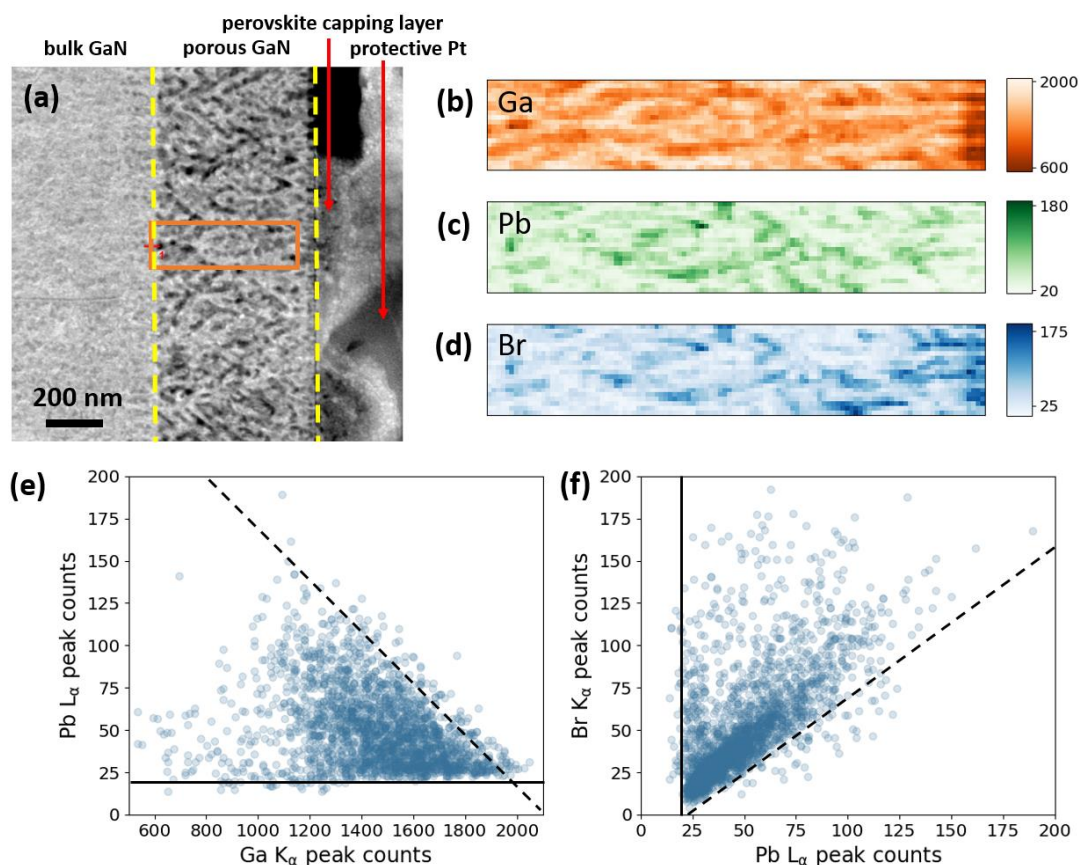


Figure 4-9 Cross-section STEM-EDX characterisation of MAPbBr<sub>3</sub>/GaN sample. (a) the HAADF-STEM image of the cross-section. The EDX elemental mapping((b), (c), (d)) was taken from the orange circle region in the HAADF-STEM image in (a). EDX elemental maps of the orange boxed area (20×110 pixels), showing the number of counts at the chosen peak for each element: (b) gallium (Ga-K), (c) lead (Pb-L), and (d) bromine (Br-K). Plots of the spatial correlation between the signal intensity measured for the elements in [(b)–(d)]: (e) Pb vs Ga, and (f) Br vs Pb. Overlapping data points appear as darker areas in the plot. Lines are a guidance to the eye (solid lines: Pb baseline; dashed lines: positive and negative correlation trends). The HAADF STEM image was taken by Boning Ding from the Department of Materials.

Figure 4-9 (a) shows the high-angle annular dark-field (HAADF) STEM image of the MAPbBr<sub>3</sub>/GaN sample cross-section. We can distinguish four layers from left to right: a bulky GaN layer, a porous GaN layer, a perovskite capping layer, and a platinum protective coating. The dark part in the porous GaN layer refers to pores in the STEM image, while the bright region refers to GaN. We measured the EDX elemental mapping of the region circled in the orange box, and they are shown in Figure 4-9 (b-d) for gallium (Ga), lead (Pb), and bromide (Br) respectively. Comparing with the HAADF-STEM image visually, the positions with weak Ga signal in elemental mapping matches with the dark parts in the STEM, which indicates where the pores are. In these positions, the signals of Pb and Br are relatively strong. This suggests a certain degree of infiltration into the nanoporous GaN. The degree of infiltration will be discussed in Section 4.2.6.

To support this argument, we analysed the spatial correlations between the elemental maps of Ga, Pb and Br in Figure 4-9 (e) and Figure 4-9 (f). Figure 4-9 (e) reveals the negative correlation between Pb and Ga signals, which is consistent with Pb being in the pores of etched GaN. The dashed line suggests the upper boundary of the maximum volume that can be filled by Pb imposed by the porosity of GaN. The solid line suggests the baseline of the Pb signal. The baseline is nonzero because of the overlap of the Pb peak with a strong Ga peak throughout the measurement area in the EDX mapping. Within the maximum filling boundary, the vertical spread of points at low Ga Count

suggests a range of Pd concentration at any porosity. Also, these points seldom reach the maximum volume boundary. These phenomena suggest an incomplete and random degree of pore filling. We attribute the incomplete filling of pores to the shrinking of lead bromide precursors when forming MAPbBr<sub>3</sub>.

Figure 4-9 (f) shows the positive correlation between Pb and Br, which is consistent with these elements occur together as compounds PbBr<sub>2</sub> and MAPbBr<sub>3</sub>. The dashed line indicates the lower bound on the ratio of Br and Pb, which is expected when MABr incorporates into PbBr<sub>2</sub>. However, it is difficult to identify whether the limiting stoichiometry that defines the dashed line results from PbBr<sub>2</sub>, MAPbBr<sub>3</sub> or other phases. Most of the dots are located above the dashed line. The slope of Br against Pb has a range of values due to various stoichiometries of MAPb<sub>x</sub>Br<sub>2+x</sub>, as the incorporating degree of MABr into PbBr<sub>2</sub> is different. At the lowest Pb counts, the points spread vertically, resulting from the unreacted MABr in the pores. As we do not have suitable standards and correlation factors to convert the measured EDX count ratios to the relative atomic concentration by the Cliff-Lorimer analysis, it is difficult to determine whether any substantial fraction of MAPbBr<sub>3</sub> is present only based on elemental analysis.

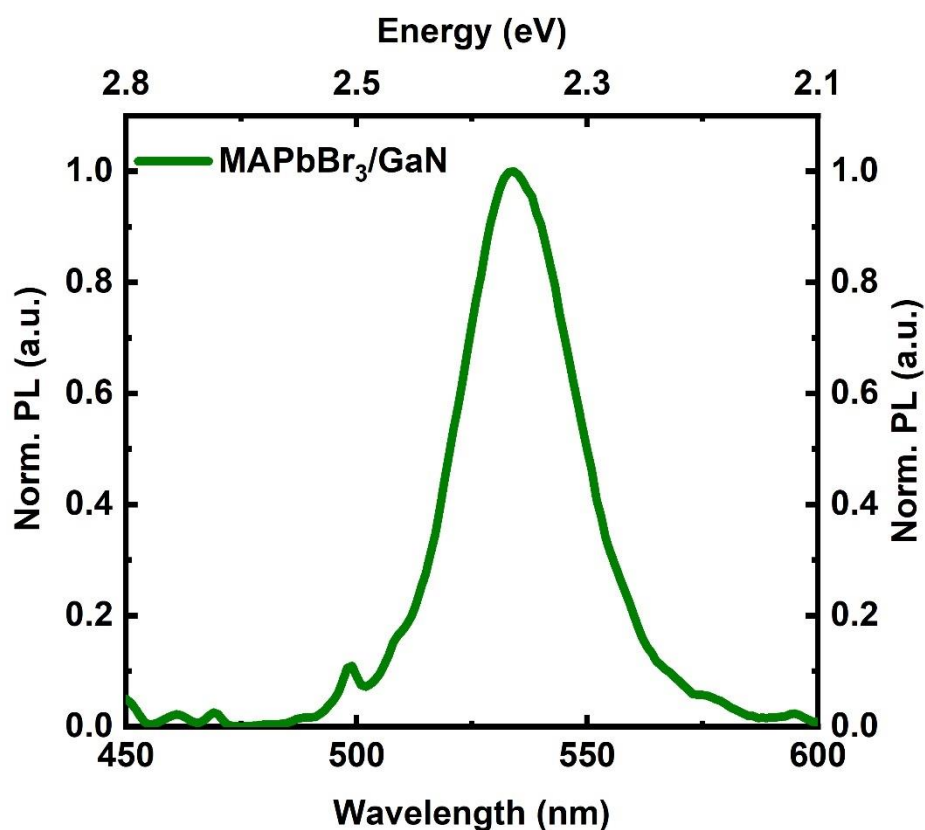


Figure 4-10 Normalised photoluminescence spectra of MAPbBr<sub>3</sub>/8 V GaN. The sample was prepared via the method described in Chapter 3 Section 3.1.2 Method 1. Excitation was performed with a Xe lamp under the ambient condition. The sample was excited at 400 nm from the GaN side.

From the elemental analysis, we verified that we have successfully infiltrated PbBr<sub>2</sub> into the porous GaN via a solution-processed method. The filling of the pores is incomplete and uneven, and the nature of the materials in the pores is still not clear. We then used photoluminescence (PL) spectroscopy (Figure 4-10) to study the nature of the material inside nanopores. The PL spectrum of the composite material reveals a characteristic green light emission, confirming both MABr and PbBr<sub>2</sub> were infiltrated

into the porous GaN, and MAPbBr<sub>3</sub> were synthesized.

## **4.2.5 Infiltration of MAPbBr<sub>3</sub> into the Nanoporous GaN with APTES Treatment**

The HAADF STEM image of the MAPbBr<sub>3</sub>/GaN sample cross-section suggests the existence of a non-negligible thick perovskite capping layer on top of the GaN (Figure 4-9 (a)). It exhibits characters of the bulk perovskite during the optical characterisation, consequently making it difficult to investigate the property of perovskite inside nanopores. Therefore, we optimised the infiltration process to eliminate the excess perovskite layer at the GaN surface.

We used (3-Aminopropyl) triethoxysilane (APTES) to treat the nanoporous GaN to modify the perovskite infiltration process. APTES is an aminosilane compound widely applied in functionalising the surface of titanium dioxide, silica, GaN, AlN and Mof.<sup>119,182–185</sup> The APTES self-assembled monolayer (SAM) can polarise the GaN surface, improving the wetting of the substrates. The amino group on APTES can bond with divalent cations<sup>186</sup>, such as Pb<sup>2+</sup>, and can prevent the lead cation from being washed away during the surface cleaning step. It is also known as a promising ligand to passivate the surface defects of MAPbBr<sub>3</sub> nanocrystals and protect them from degradation.<sup>183,187</sup> Considering these reported functions of APTES, we used it to polarise the GaN surface, optimise the infiltration process and passivate the defect levels at MAPbBr<sub>3</sub> nanoparticles' surface. Former research suggested that the APTES

growth mode depends strongly on the property of GaN.<sup>184</sup> To make sure we achieve a perfect surface functionalisation with a monolayer of APTES, we hydroxylate the GaN surface with Piranha solution first before the APTES treatment.<sup>185</sup> The detail of the infiltration process can be found in Section 3.1.2 Method 2 in Chapter 3.

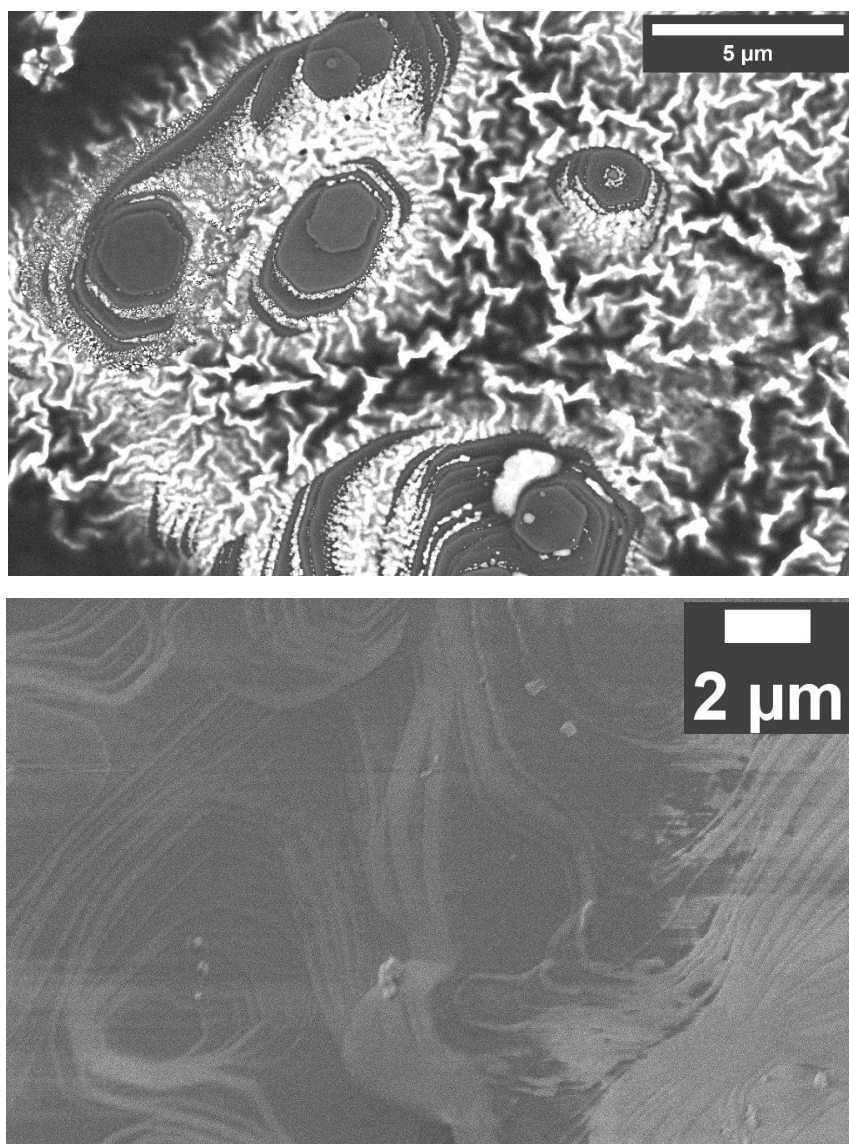


Figure 4-11 Top-view scanning electron microscope images of MAPbBr<sub>3</sub>/GaN sample prepared without (Top) and with (Bottom) APTES treatment. Top: Dark hexagon is the surface of nanoporous GaN, while the bright cluster is the MAPbBr<sub>3</sub> capping layer, Scale bar: 5 μm. Bottom: Dark hexagon is the surface of nanoporous GaN, while the bright crystal is the MAPbBr<sub>3</sub> leftover at the GaN surface, Scale bar: 2 μm.

Figure 4-11 compares the top-view SEM of MAPbBr<sub>3</sub>/GaN samples prepared with (top) and without (bottom) APTES treatment. In the left side SEM, the dark hexagon part

refers to the GaN surface, and the bright part refers to the perovskite capping layer on top of the GaN. It is evident that a large amount of perovskite is accumulated at the GaN surface. The measured sample also has an orange colour, which is the characteristic colour of MAPbBr<sub>3</sub>. However, with the APTES functionalisation, the surface of the MAPbBr<sub>3</sub>/GaN sample is much cleaner. Different from samples prepared without treatment, the APTES treated sample looks pale yellow after perovskite infiltration. Only a small quantity of perovskite crystals, seen as bright spheres at the GaN surface, are left at the GaN surface in the top-view SEM. Samples without the thick capping layer are ideal for the following optical property characterisation of perovskite inside nanopores in the next chapter.

## **4.2.6 Estimation of the Infiltration Degree of MAPbBr<sub>3</sub> in the 8 V etched Nanoporous GaN**

We estimated the effective thickness of the perovskite infiltrate into the 8 V etched nanoporous GaN from the absorption of the sample,

$$t = \frac{2.303A}{a}, \quad (4.1)$$

where  $t$  is the thickness of the material,  $A$  is the absorption and  $a$  is the absorption coefficient of MAPbBr<sub>3</sub>. In Figure 4-12, we plot the UV-Vis absorption spectra of a pristine 8 V GaN and a MAPbBr<sub>3</sub>/8 V GaN sample. GaN samples were treated with APTES to eliminate the perovskite capping layer. According to the literature, the absorption peak at 460 nm originates from a very high defects density of GaN.<sup>188</sup> It is

inconsistent from sample to sample, revealed as the intensity difference of 460 nm absorption peak in two spectra. Beyond that, the absorption of MAPbBr<sub>3</sub>/GaN at 500 nm originates from the perovskite. Comparing with perovskite thin film, the absorption of perovskite in pores is broad, resulting from a crystal size distribution, which will be discussed that in the next chapter. The absorption coefficient of MAPbBr<sub>3</sub> at 500 nm is 38000 cm<sup>-1</sup>.<sup>12</sup> Therefore, the estimated effective thickness of MAPbBr<sub>3</sub> inside pores is 46 nm.

We run the same estimation on five MAPbBr<sub>3</sub>/8 V GaN samples, and the estimated thickness ranging from 40 nm to 54 nm (Table 4-1), showing the infiltration process is repeatable. The GaN sample we used in this study is 8 V etched GaN, and the porosity is 30% in a 500 nm porous layer. Based on the estimated thickness, we know that the pore filling degree is about 30% for 8 V etched GaN. This result is physically reasonable and is likely to reflect incomplete pore filling due to shrinkage of the precursor film upon transformation into perovskite.

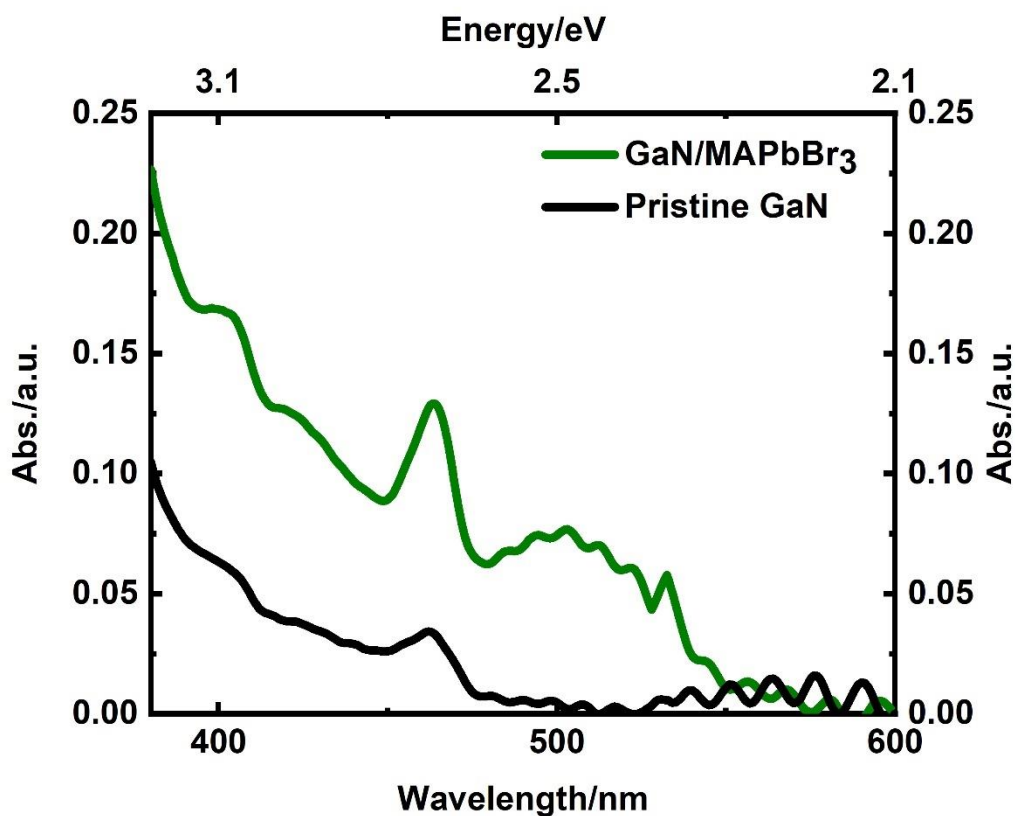


Figure 4-12 UV-Visible absorption spectra of a pristine nanoporous GaN sample (Black) and a MAPbBr<sub>3</sub>/8 V GaN sample (Green) under ambient conditions. Nanoporous GaN substrates were treated with APTES before perovskite infiltration. The wavy character from 500 nm to 600 nm results from light interference in the GaN layer. The additional absorption peak at around 500 nm in the spectrum of the MAPbBr<sub>3</sub>/GaN sample originates from MAPbBr<sub>3</sub> inside nanopores.

Sample number	Absorption at 500 nm (a.u.)	Effective Thickness (nm)
1	0.066	40
2	0.070	42
3	0.074	45
4	0.090	54
5	0.076	46

Table 4-1 Estimated effective thickness of MAPbBr<sub>3</sub> inside 8 V GaN for four samples prepared with the same method. Nanoporous GaN substrates were treated with APTES before perovskite infiltration.

### 4.2.7 Protective Effect of the Nanoporous GaN on MAPbBr<sub>3</sub>

The nanoporous GaN matrix enhances the stability of perovskite in nanopores and effectively prevent the degradation of MAPbBr<sub>3</sub> in the ambient environment. In this work, we studied GaN's protective effect on perovskite under two conditions, under the light-induced condition and under the ambient condition.

For the light-induced perovskite stability test, we monitored the photoluminescence intensity changes of MAPbBr<sub>3</sub> in GaN nanopores and bulk MAPbBr<sub>3</sub> thin film under

excitation with 405 nm CW laser ( $9.5 \text{ mW cm}^{-2}$ ) for 20000 seconds. We prepared four types of samples, MAPbBr<sub>3</sub>/8 V GaN, epoxy- and glass- encapsulated MAPbBr<sub>3</sub>/8 V GaN, MAPbBr<sub>3</sub> spin-coated thin film on quartz and epoxy- and glass- encapsulated MAPbBr<sub>3</sub> spin-coated thin film on quartz. MAPbBr<sub>3</sub>/8 V GaN was prepared with the APTES treated GaN. As shown in Figure 4-13, after exciting with the 405 nm CW laser for 20000 seconds, the PL intensity of the MAPbBr<sub>3</sub>/GaN in the ambient environment increased to more than five times its initial PL intensity, while PL of the bulk MAPbBr<sub>3</sub> thin films, both encapsulated and non-encapsulated, decreased rather rapidly to less than 50% of their initial intensity. The PL intensity of the encapsulated MAPbBr<sub>3</sub>/GaN barely changed with time under an air-free environment in 20000 seconds. This demonstrates that perovskite nanocrystals remain stable under blue light illumination in the absence of water and oxygen. Signs of degradation have not been observed in this time range. In literature, the light-induced degradation of perovskite results from two interrelated processes, ion migration<sup>189</sup> and annealing of the sample.<sup>123</sup> In perovskite thin film, ions, especially halide, are able to migrate relatively far apart from their original location. When perovskite is spatially confined in a rigid matrix as the nanoporous GaN, the ion migration is limited. Consequently, light-induced degradation is prevented.<sup>123</sup> This result demonstrates that the light-induced degradation of the MAPbBr<sub>3</sub> is limited by the nanoporous GaN matrix, therefore, improving the stability of perovskite in nanopores.

We also know from this comparison that MAPbBr<sub>3</sub> in the nanoporous GaN matrix is

more stable in both ambient environment and air/water-free environment than bulk MAPbBr<sub>3</sub> thin film under 405 nm laser beams for about 5 hours. We observed a photobrightening treatment process with the MAPbBr<sub>3</sub>/8 V GaN sample. We attribute the increase in PL intensity to the passivation of the trapping state of light-curing with oxygen, hence reducing the non-radiative recombination process.<sup>190,191</sup>

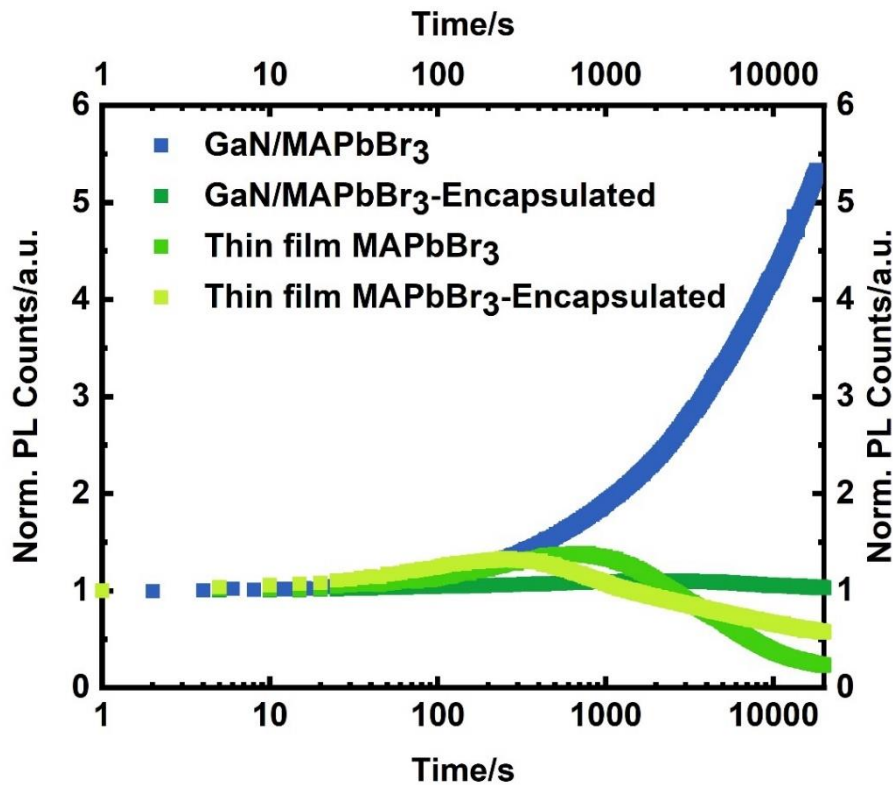


Figure 4-13 Normalized time evolution of the PL intensity during illumination at 405 nm CW laser ( $9.5 \text{ mW cm}^{-2}$ ) for  $2 \times 10^4$  seconds under ambient condition for MAPbBr<sub>3</sub>/GaN (dark blue squares), epoxy and glass encapsulated MAPbBr<sub>3</sub>/GaN (dark green squares), spin-coated MAPbBr<sub>3</sub> thin film on quartz (green squares), and epoxy and glass encapsulated MAPbBr<sub>3</sub> thin film on quartz (yellow-green squares). The initial PL intensities of four samples are normalised to one. The PL intensity of MAPbBr<sub>3</sub>/GaN (dark blue squares) increases five times its initial intensity. The PL intensity of encapsulated MAPbBr<sub>3</sub>/GaN (dark green squares) barely changes during the plotted time scale. The PL intensity of spin-coated MAPbBr<sub>3</sub> thin films (encapsulated and non-encapsulated) decrease to less than half of their initial PL intensity.

We also measured the photoluminescence quantum efficiency (PLQE) to quantitatively study the protective effect on the selected GaN samples in the ambient environment on a longer time scale. In this study, we prepared three types of samples, MAPbBr<sub>3</sub>/8 V GaN, MAPbBr<sub>3</sub> spin-coated thin film on quartz and MAPbBr<sub>3</sub> thin film on bulk GaN. The MAPbBr<sub>3</sub>/8 V GaN was prepared via the method without APTES treatment. The PLQE of the unsealed perovskite on nanoporous GaN dropped from 1.65% to 0.93% after ten days in the ambient atmosphere. After 50 weeks, the PLQE of unsealed MAPbBr<sub>3</sub>/GaN dropped to 0.60%, about 36% of its initial PLQE, and the emission can be observed by bare eyes.

In contrast, the PLQE of unsealed glass and bulky GaN dropped to less than 0.10%. Compared with literature<sup>175</sup>, this year-long survival of unsealed MAPbBr<sub>3</sub> perovskite in the ambient environment is one of the longest recorded durations reported, which suggested the protective effect of porous GaN on perovskite. The PLQE measurement was carried out by Kevin T. P. Lim.

Our observations demonstrate that the porous GaN can protect MAPbBr<sub>3</sub> inside pores from light-induced degradation for about 5 hours, as well as from environmental degradation up to 1 year in the ambient atmosphere. This result suggests that the GaN matrix improves the stability of MAPbBr<sub>3</sub> in the ambient atmosphere, and such composite is promising in developing ambient environment stable light-emitting devices in the future.

### 4.3 Conclusion and Future Work

This chapter demonstrates a solution-processed method to prepare perovskite /GaN composite via a two-step deposition method at low temperatures. With further GaN surface treatment, we successfully prepared perovskite/GaN composite without a capping layer and achieved a 30% pore-filling degree for 8 V etched GaN. As our preparation approach only involves a simple solution-processed method, it is possible to infiltrate other types of perovskites, such as low dimensional perovskite and inorganic perovskite, into the GaN matrix. Therefore, the perovskite/GaN has the potential to become a colour tunable light emitting material in the future. We also find that the nanoporous GaN matrix can prevent light-induced degradation of MAPbBr<sub>3</sub> under continuous luminescence under 405 nm laser for more than five hours, and perovskite inside pores was stable after one year of exposure in the ambient environment. The solution-process approach and long-term stability make the perovskite/GaN composite a promising candidate for light-emitting devices in the future.

Another interesting study in this investigation is the recombination mechanism behind the yellow band emission of pristine GaN. We demonstrated that a self-trapping exciton recombination process may contribute to the yellow band emission for the first time. We suggest an argument different from the literature before. In future, more research should be carried out to study the origin of GaN's yellow band emission in order to

investigate whether the yellow emission arises from defect states or self-trap states.

However, the confinement effect of nanoporous GaN on perovskite has not been investigated before. Therefore, we use transient photoluminescence and transient absorption in the following chapter to study the recombination process in GaN confined perovskite.



# Chapter 5 Confinement Effect of the Nanoporous GaN on Methylammonium Lead Bromide Perovskite

We have successfully synthesized a MAPbBr<sub>3</sub>/GaN composite in the last chapter. The composite has shown the potential to be applied in light emitting devices due to the simple solution-processed method. However, the photophysics properties of the new composite are still unknown. Therefore, this chapter demonstrates the charge carrier recombination process in MAPbBr<sub>3</sub> nanocrystals inside the nanoporous GaN with transient photoluminescence and transient absorption measurements. In this investigation, we observed enhanced radiative recombination rate and blue-shift photoluminescence from the MAPbBr<sub>3</sub> nanocrystals comparing to its bulk counterpart. Additional, we show that the dominant recombination process in MAPbBr<sub>3</sub> nanocrystals is exciton recombination rather than the bimolecular recombination process in bulk perovskite. These results reveal that the quantum confinement effect of nanoporous GaN matrix on MAPbBr<sub>3</sub> increase the binding energy of electrons and holes in perovskite. This enhanced carrier interaction suggests that the perovskite/nanoporous GaN composite could achieve efficient light emitting in the future. We also report that the significant non-radiative process limits the light emitting performance of the

composite. Therefore, perovskite nanocrystal passivation routes should be explored in future research.

## 5.1.1 Background and Motivation

Organic-inorganic lead halide perovskites are novel semiconductors for next-generation displays and optoelectronic devices. Nevertheless, perovskites are hindered by their poor stability in the ambient atmosphere as they rapidly degrade when exposed to air and moisture, making it quite laborious to apply in devices. Additionally, the dominant charge carriers for three-dimensional perovskites, such as methylammonium lead bromide perovskite (MAPbBr<sub>3</sub>), are free electrons and holes at room temperature.<sup>40</sup> The low binding energy between carriers leads to a low radiative recombination rate. Therefore, the non-radiative recombination process competes effectively with the radiative processes, especially at low carrier density, resulting in poor quantum efficiency. The application of perovskites in light-emitting devices has motivated the exploration of synthetic methods to improve their luminescence performance. One approach is reducing the perovskite crystal size and dimensionality to achieve quantum confinement. Colloidal chemistry techniques, such as emulsion synthesis<sup>192</sup>, nanocrystalline capping<sup>193</sup>, reprecipitation method<sup>194</sup> and two-step processes with PbI<sub>2</sub> nanocrystals as templates<sup>195</sup>, have been investigated to achieve nanocrystals featuring quantum size effects.

In situ growth of perovskite nanocrystals in the mesoporous matrix offers an alternative ligand-free approach to achieving quantum confinement of perovskites. The quantum confinement effect on perovskites has been observed in matrices such as mesoporous

silica<sup>123</sup>, mesoporous titania<sup>196</sup>, anodised alumina<sup>118</sup> and mesoporous ZrO<sub>2</sub><sup>197</sup>. These nanoporous templates force the formation of perovskite nanoparticles in pores and confine the localisation of charge carriers. When the particle size approaches the exciton Bohr radius of the perovskite, strong spatial confinement leads to a blue shift in photoluminescence. The overlap of electron and hole wavefunctions enhance the probability of radiative recombination, thus increasing the quantum efficiency. When perovskites are surrounded by materials with a lower dielectric constant, electrons and holes in perovskite will experience a stronger attraction due to the dielectric confinement effect, revealed as a fine-tuning of the dynamic photoemission properties. Perovskites encapsulated in these matrices can remain stable on time scales ranging from one day to more than one month<sup>175</sup>. However, these reported matrixes suffer from poor conductivity in device application, while GaN has known for its outstanding performance in conductivity.

We have demonstrated an approach to infiltrate MAPbBr<sub>3</sub> perovskite into the electrochemical etching gallium nitride matrix in Chapter 4. Since the GaN/MAPbBr<sub>3</sub> is reported to be a type-I heterojunction, we anticipate that MAPbBr<sub>3</sub> perovskite will be both quantum and dielectric confined in the nanoporous GaN matrix.<sup>198</sup> However, the charge carrier recombination process of perovskite inside pores is still unclear. This chapter will discuss the confinement effect of nanoporous GaN on the charge carrier dynamics of MAPbBr<sub>3</sub> inside pores.

## 5.2 Results and Discussion

### 5.2.1 MAPbBr<sub>3</sub>/GaN Sample Preparation

MAPbBr<sub>3</sub>/GaN samples used in this study were prepared via the method reported in Chapter 3. We used the APTES treated GaN as the matrix to ensure that no perovskite capping layer interferes with the optical characterisation. We used 6 V etched GaN, 8 V etched GaN, and 10 V etched GaN as substrates for the pore-size-dependent photoluminescence study. We used 8 V GaN as substrates for all the other transient photoluminescence and transient absorption studies. A MAPbBr<sub>3</sub> spin-coated thin film on quartz was used as a reference. We prepared the MAPbBr<sub>3</sub> thin film with the method described in Chapter 3.

In the following optophysical study on the MAPbBr<sub>3</sub>/GaN composite, we used light sources with energy below GaN's band edge to excite samples. Therefore, we could eliminate the influence of the yellow band emission from GaN. When MAPbBr<sub>3</sub>/GaN is excited above the band edge of GaN, both GaN and perovskite will be excited. The broad yellow band emission from GaN overlaps with the sharp photoluminescence of perovskite at 525 nm (2.36 eV), as shown in Figure 5-1. It would be difficult to distinguish the perovskite signal from that of GaN during the measurement. Therefore, we only excite perovskite below the band edge of GaN when studying the carrier recombination process in perovskite.

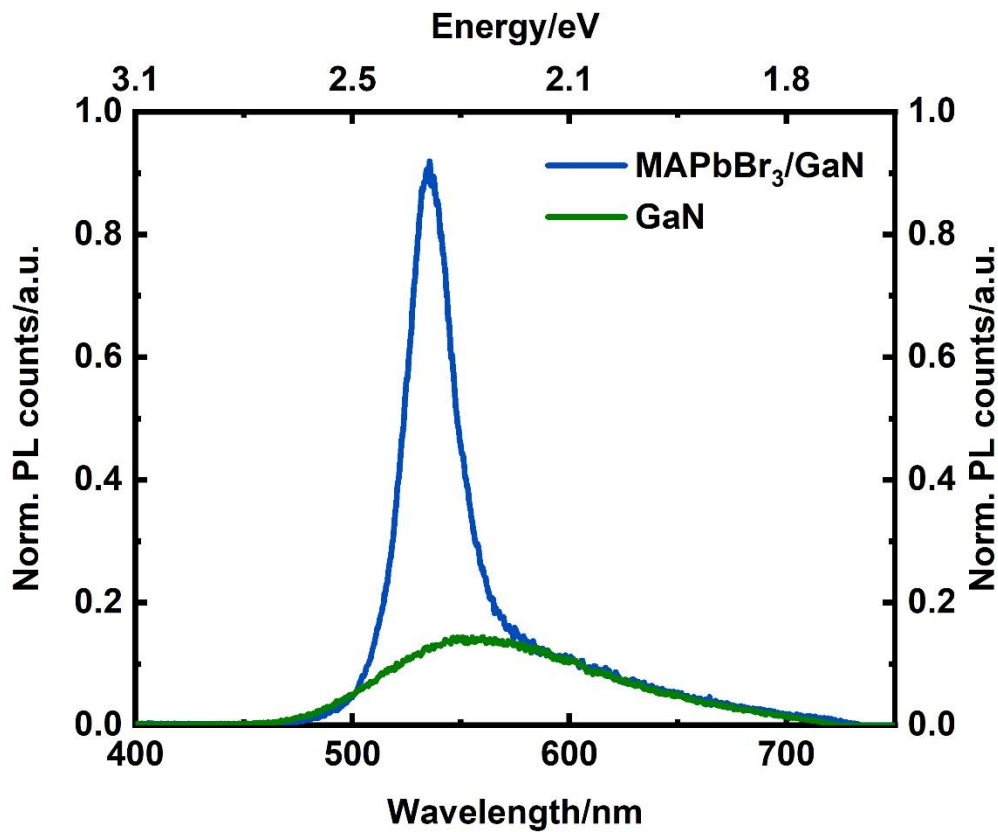


Figure 5-1 Normalised photoluminescence spectra of MAPbBr<sub>3</sub>/8 V GaN and pristine GaN. The sample was prepared via the method described in Section 3.1.2 Method 2 in Chapter 3. Excitation was performed with a Xe lamp under the ambient condition. The sample was excited at 350 nm from the GaN side. Spectra are normalized to the low energy edge of GaN's yellow band emission.

## 5.2.2 Templating Effect of Nanoporous GaN on MAPbBr<sub>3</sub> Perovskite

To investigate the templating effect of the nanoporous GaN on MAPbBr<sub>3</sub>, we prepared three types of porous GaN samples with various pore sizes via controlling

electrochemical etching voltage. GaN substrates were etched at 6 V, 8 V and 10 V. As we described in Section 4.2.1 when increasing the etching voltage from 6 V to 10 V, the minimum diameter of an individual pore at the surface increases from 11 nm to 16 nm. Meanwhile, the increase in etching voltage cause pores to merge into trenches and channels with long and irregular shapes, resulting in even larger pores. We deposited MAPbBr<sub>3</sub> perovskite onto three types of APTES treated GaN substrates and used a MAPbBr<sub>3</sub> spin-coated thin film on quartz as a reference.

We plot the steady-state photoluminescence (PL) spectra of MAPbBr<sub>3</sub>/6 V GaN, MAPbBr<sub>3</sub>/8 V GaN, MAPbBr<sub>3</sub>/10 V GaN and MAPbBr<sub>3</sub> thin film in Figure 5-2. The PL of MAPbBr<sub>3</sub>/GaN samples shows a ~20 nm (87 meV) blue shift compared with that of the MAPbBr<sub>3</sub> bulk thin film (544 nm), suggesting increasing confinement due to the perovskite being forced into nanopores. The nanopore size of the porous GaN ranges from 11 nm to 20 nm. Therefore, the growth of perovskite from precursor solutions is constrained in these nanoreactors, leading to a smaller perovskite crystal size than bulk perovskite. The reduction of perovskite crystal sizes leads to quantum confinement. When the crystal size of the MAPbBr<sub>3</sub> approaches its exciton Bohr radius 4.7 nm<sup>199</sup>, the wavefunction and the energetic states of excitons will be influenced, shown as the blueshift we observed in photoluminescence.

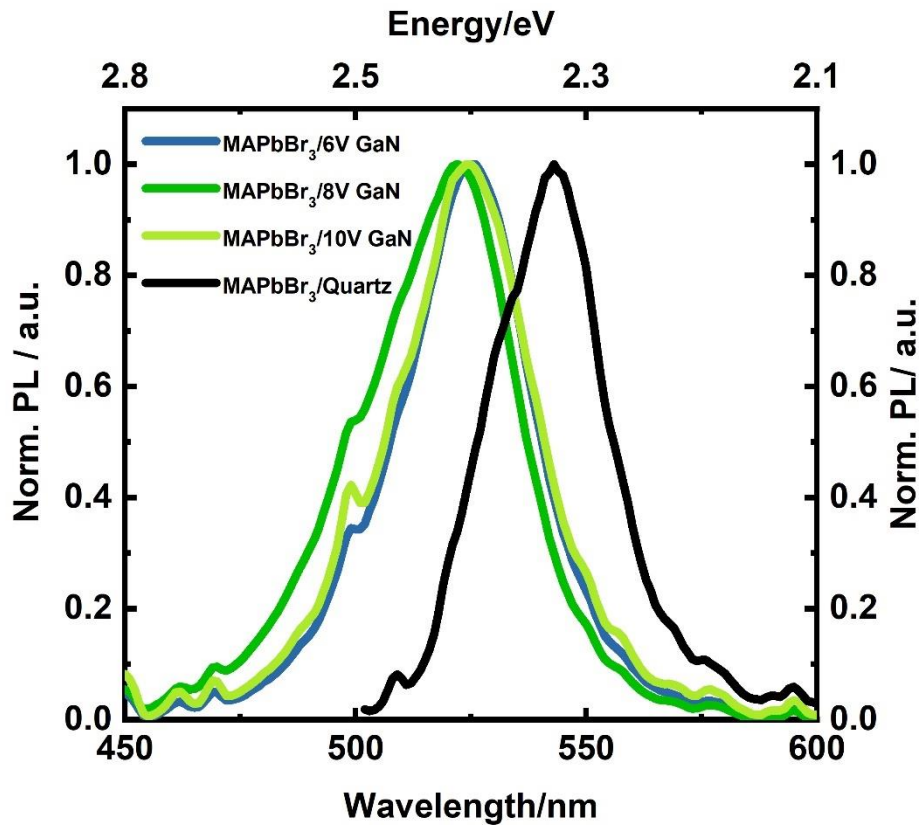


Figure 5-2 Normalised photoluminescence spectra of MAPbBr<sub>3</sub>/6 V GaN (dark blue line), MAPbBr<sub>3</sub>/8 V GaN (dark green line), MAPbBr<sub>3</sub>/10 V GaN (light green line) and MAPbBr<sub>3</sub> spin-coated thin film on quartz (black line). Nanoporous GaN substrates were treated with APTES before perovskite infiltration. Excitation was performed with a Xe lamp under the ambient condition. Samples were excited at 400 nm from the GaN side. PL spectra of MAPbBr<sub>3</sub> grown in porous GaNs are blue shifted by about 20 nm (87 meV) compared to the MAPbBr<sub>3</sub> thin film (544 nm). In addition, no significant pore size-dependent blue shift of PL spectra for MAPbBr<sub>3</sub>/GaN is observed. The peak positions of MAPbBr<sub>3</sub> in nanoporous GaNs are 525 nm, 522 nm, and 524 nm for 6 V, 8 V, and 10 V etched GaN respectively. No significant pore-size-dependent blue

shift is observed. This result suggests that although the nanopores forced MAPbBr<sub>3</sub> to form smaller crystals, the perovskite nanocrystal size is not strongly dependent on the pore size in the investigated pore size range. This result contradicts our former pore-size dependent study on MAPbBr<sub>3</sub>/GaN with a perovskite capping layer.<sup>200</sup> In our former investigation, a systematic blue shift of the PL peak from 541 nm to 525 nm was observed from MAPbBr<sub>3</sub>/bulk GaN to MAPbBr<sub>3</sub>/6 V porous GaN. The former measured PL spectra (Figure 5-3) of perovskite in the same type of GaN sample is red-shifted compared to the capping layer free sample. This red shifted PL results from the contribution from the bulk perovskite capping layer. We also note that the photoluminescence wavelength is sensitive to variations in preparation conditions for samples with a capping layer. We propose that the difference in PL results from the uncontrollable capping layer thickness during the surface washing process. Therefore, the pore-size-dependent blue shift in PL we observed before may be caused by a variable fraction of bulk perovskite layer contributing to the emission. It is not the intrinsic property of the MAPbBr<sub>3</sub> inside nanopores.

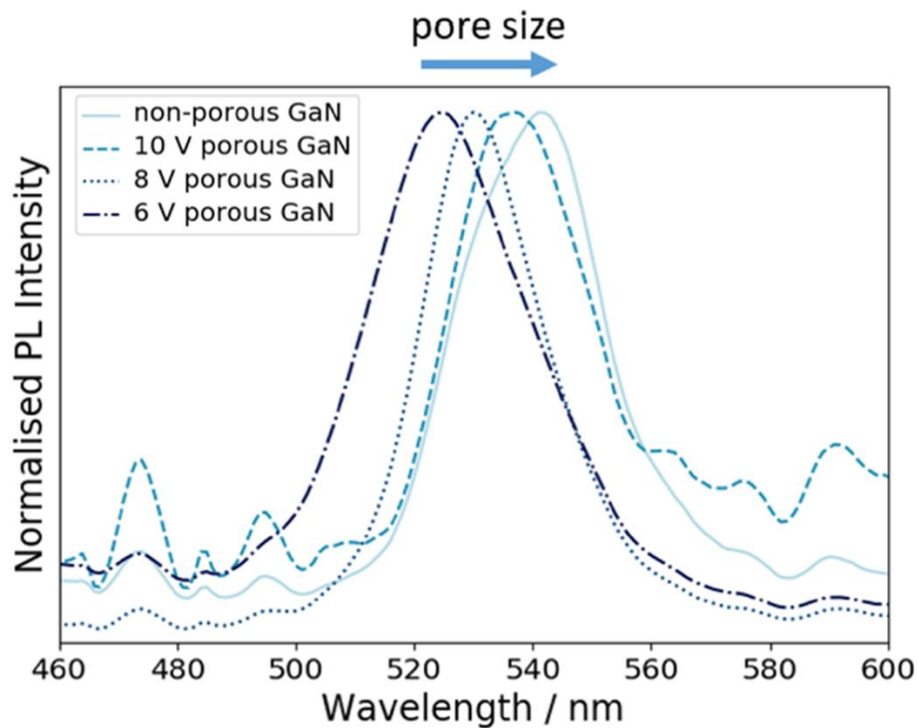


Figure 5-3 Normalised photoluminescence spectra of MAPbBr<sub>3</sub>/6 V GaN (dark blue dashed line), MAPbBr<sub>3</sub>/8 V GaN (blue dot line), MAPbBr<sub>3</sub>/10 V GaN (cyan dashed line) and MAPbBr<sub>3</sub> thin film on quartz (light blue solid line). Nanoporous GaN substrates were not treated with APTES. Samples were excited at 380 nm with a Xe lamp from the sample side. The PL measurement was carried out by Kevin T. P. Lim.

The FWHMs of MAPbBr<sub>3</sub> in the APTES treated nanoporous GaNs range from 35 nm to 40 nm, while the FWHM of MAPbBr<sub>3</sub> spin-coated thin film is only 29 nm. This broadening in PL could indicate a distribution of nanoparticle size inside pores. The PL spectra in Figure 5-2 was taken with the fluorometer, showing the photoluminescence character at the square centimetre scale. Therefore, we took a closer look at the sample with the hyperspectra optical microscope at a square micrometre scale in Section 5.2.3

to extract more information about nanocrystals distribution inside pores.

### **5.2.3 MAPbBr<sub>3</sub> Nanocrystals Size Distribution in Nanoporous GaN**

Figure 5-4 (a) shows the top view of the MAPbBr<sub>3</sub>/8 V GaN sample surface taken with an optical microscope. The hexagonal shape in Figure 5-4 (a) is the character of the 8 V etched GaN surface, and the bright dots at the surface of GaN is the perovskite leftover after the surface washing process. Figure 5-4 (b) shows the photoluminescence image of the sample at the same area in Figure 5-4 (a). The sample was excited with a 405 nm CW laser to ensure only the perovskite was excited. The bright dots in Figure 5-4 (b) indicate the light emission species, while no emission was detected at the dark part.

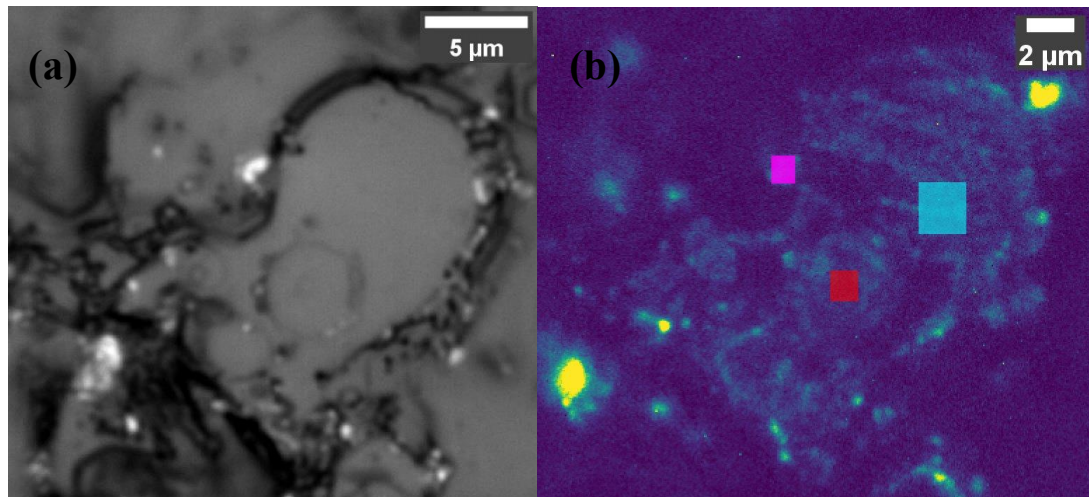


Figure 5-4 Hyperspectra photoluminescence image of encapsulated  $\text{MAPbBr}_3/\text{GaN}$  sample: correlated reflection (a) and PL mode image (b). Images were taken using a hyperspectra PL microscope. The nanoporous GaN substrate was treated with APTES before perovskite infiltration. The sample was encapsulated with epoxy and glass in the nitrogen-filled glovebox. The sample was excited with a 405 nm continuous wave laser with an excitation intensity of  $100 \text{ mW/cm}^2$  in the PL mode measurement. Hyperspectra images were measured using an IMA-VIS system (Photon etc.). The measurement was carried out jointly with Kangyu Ji.

We picked three areas (pink area, blue area and red area) from the PL image in Figure 5-4 (b), where no capping perovskite is observed in Figure 5-4 (a), and compared their PL spectra in Figure 5-5. Local PL spectra are not uniform. Their PL peaks range from 523 nm to 511 nm from different areas. Since we observed roundness characters from the Pb elemental mapping in Figure 4-9 in Chapter 4, we assume that perovskite forms spherical crystals inside nanopores. Based on this hypothesis, we use the Brus

Equation to estimate MAPbBr<sub>3</sub> crystal size from the local PL of perovskite,

$$E^* = E_g + \frac{\hbar^2 \pi^2}{2\mu R^2} + \frac{1.8e^2}{4\pi\epsilon_0\epsilon_r R}, \quad (5.1)$$

where  $E^*$  is the PL peak wavelength,  $E_g$  is the perovskite bandgap,  $R$  is the radius of the crystal. We calculated the crystal size of MAPbBr<sub>3</sub> to be 8 nm when PL peak is at 511 nm (blue line), 9 nm when PL peak is 518 nm (red line) and 9.5 nm when PL peak is 523 nm (pink line). At the blue region in Figure 5-4 (b), the PL peak is very broad (FHMW=43.9 nm), suggesting the existence of perovskite nanocrystals with a size distribution ranging from 8 nm to 9.5 nm. The calculated MAPbBr<sub>3</sub> nanocrystal size is smaller than the pore size of nanoporous GaNs observed from the SEM in Section 4.2.1. As we discussed before, the incomplete pore filling is due to shrinkage of the precursor film upon transformation into perovskite. Instead of forming a large particle with a similar size to the pore that contains it, MAPbBr<sub>3</sub> perovskite prefers to form several smaller nanoparticles inside GaN templates. This also explains why the PL spectra are not pore-size-dependent in Section 5.2.1. However, the perovskite crystallisation mechanism in the nanoporous GaN is not clear, which should be investigated in further research.

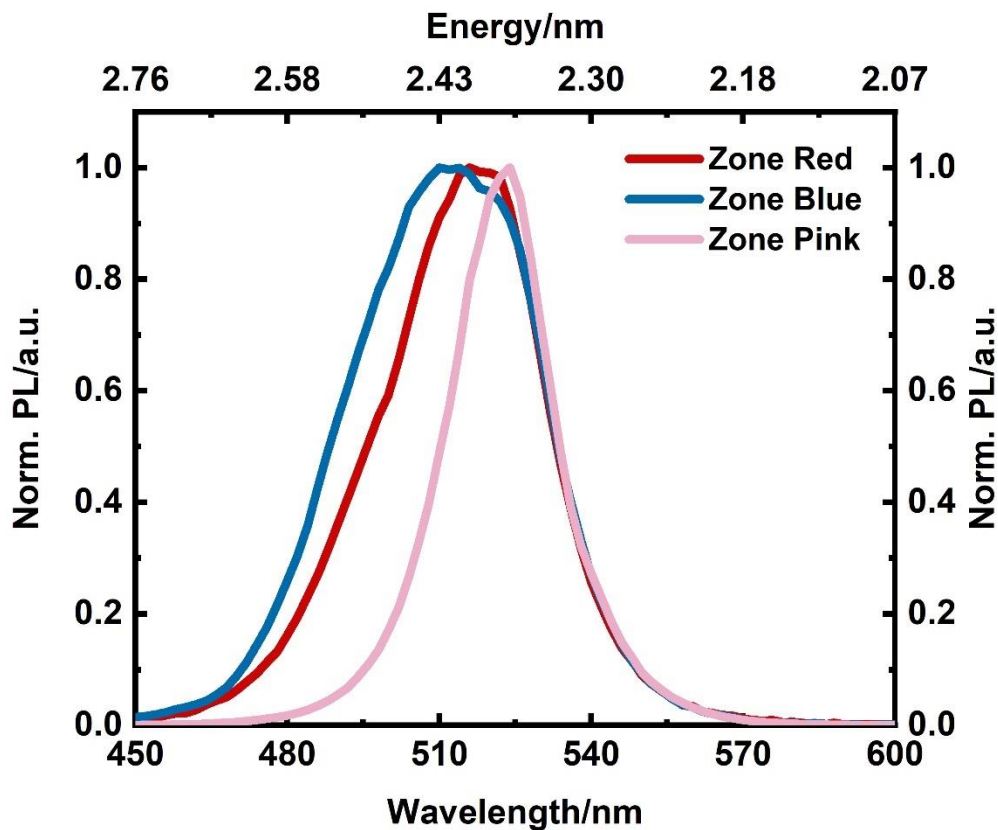


Figure 5-5 Normalised photoluminescence spectra of encapsulated MAPbBr<sub>3</sub>/GaN at three areas in Figure 5-3 PL mode image. Nanoporous GaN substrates were treated with APTES before perovskite infiltration. The sample was encapsulated with epoxy and glass in the nitrogen-filled glovebox. The sample was excited with a 405 nm continuous wave laser with an excitation intensity of 100 mW/cm<sup>-2</sup>. The measurement was carried out jointly with Kangyu Ji.

We compare the transient PL of a MAPbBr<sub>3</sub>/8 V GaN sample at the short emission wavelength (450 nm to 500 nm) and at the long emission wavelength (520 nm to 600 nm) to study the influence of perovskite size distribution on the carrier recombination dynamic. As shown in Figure 5-6, the excited state lifetime decreases

faster at the short wavelength. Due to the crystal size distribution, smaller perovskite crystals contribute to the shorter wavelength PL. Hence, the PL decay accelerates as the crystal size reduces. We calculate the effective lifetime as the time required for PL intensity reduces to  $1/e$  of its initial intensity<sup>201</sup>, plotted in Figure 5-7. The calculated effective lifetime is ~2.45 ns at 450 nm to 500 nm and ~5.10 ns at 520 nm to 600 nm.

We suggest three hypothesises to explain the accelerated PL decay at the shorter wavelength, (1) the energy transfer from smaller crystals to larger crystals due to size distribution, (2) the reduction of crystal size leads to enhanced spatial confinement, resulting in larger binding energy between carriers and (3) the reduction of crystal size introduces more surface defect states, revealed as a higher number of non-radiative recombination paths.

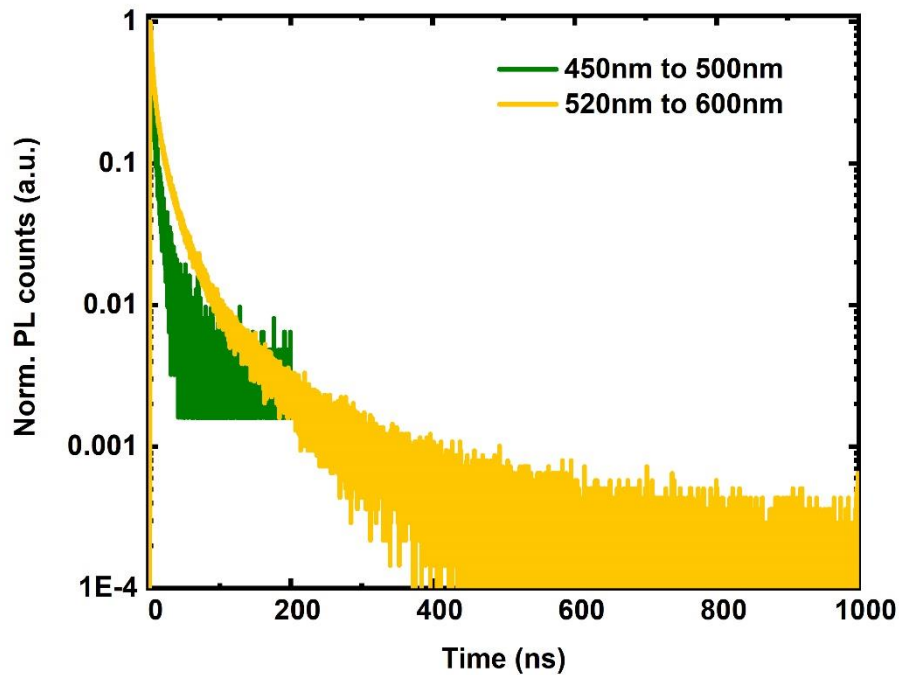


Figure 5-6 Normalised photoluminescence decay of encapsulated MAPbBr<sub>3</sub>/GaN sample integrating from 450 nm to 500 nm (green line) and from 520 nm to 600 nm (yellow line). Nanoporous GaN substrates were treated with APTES before perovskite infiltration. The sample was encapsulated with epoxy and glass in the nitrogen-filled glovebox. The sample was excited with a pulsed laser (1 MHz) at 405 nm (3.06 eV) at a fluence of 2.97  $\mu\text{Jcm}^{-2}$  per pulse. The detecting wavelength was selected with a 500 nm shortpass filter and a 520 nm longpass filter, respectively. The measurement was carried out jointly with Kangyu Ji.

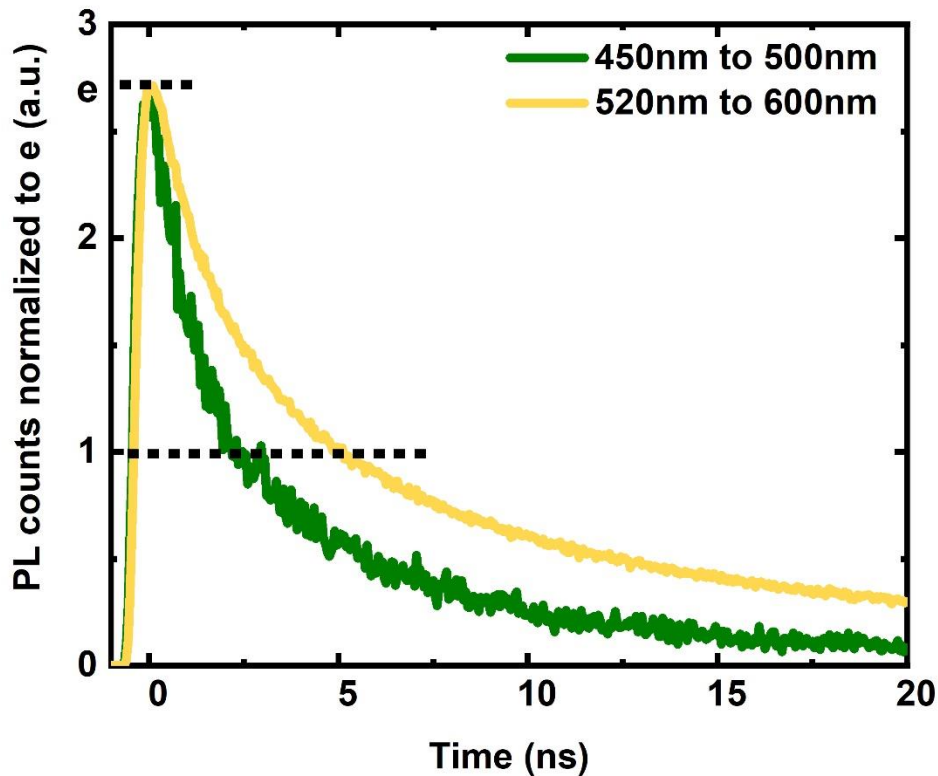


Figure 5-7  $1/e$  method to calculate the effective lifetime of PL decays in Figure 5-5.

Photoluminescence decay normalized to  $e$  of encapsulated MAPbBr<sub>3</sub>/GaN sample integrating from 450 nm to 500 nm (green line) and from 520 nm to 600 nm (yellow line).

We performed transient absorption (TA) measurement on a MAPbBr<sub>3</sub>/ 8 V GaN sample to verify the mechanism behind the wavelength-dependent PL decay. Energy transfer from high energy states to low energy states between perovskite nanocrystals is observed from the TA measurement. The sample was pumped at 400 nm at 45  $\mu\text{J cm}^{-2}$ . TA spectra in the first 350 ps after the photoexcitation are shown in Figure 5-8. The

dominant features of TA spectra are two ground state bleach (GSB) peaks at 510 nm and 520 nm. As shown in Figure 5-8 (a), the bleach at 510 nm recovers much faster than the bleach at 520 nm in the first 350 ns. We normalised the TA spectra to the maximum absorption of the GSB (Figure 5-8 (b)), and the relative intensity of 520 nm GSB to 510 nm GSB increases with time. As the time scale is too short for photon recycle to happen, the evolution of TA spectra in the first 350 ps suggests that charge carriers reach the low energy excitation state at 520 nm from the high energy excitation state at 510 nm. Time traces at probe wavelengths (510 nm and 520 nm) are shown in Figure 5-8 (c). After photoexcitation, the 510 nm GSB rises almost simultaneously and quickly decays. The 520 nm GSB rising is slower than that at 510 nm and declines after 5 ps. The slow rising kinetic at the 520 nm band reveals the carrier populating process to this phase due to the carrier transfer from a higher energy state. This phenomenon suggests energy transfer process take place due to the perovskite nanocrystal size distribution.

According to the TA measurement, the energy transfer process completes in the first 350 ps after photoexcitation. Therefore, this process is beyond the resolution of the transient PL measurement in Figure 5-6. In addition, no notable slower PL counts rise time is shown in Figure 5-7 after photoexcitation. Based on this study, although energy transfer happens due to perovskite crystal size distribution, it cannot be observed from the transient PL study in Figure 5-6. Therefore, the fast PL decay we observed is not

caused by charge transfer due to crystal size distribution.

According to former studies on perovskite nanocrystals confined in nanoporous structures,<sup>123,196</sup> the smaller the perovskite crystal, the larger the surface lattice distortion. The surface lattice distortion leads to a higher density of surface defects, which could give rise to more non-radiative decay paths. Therefore, a faster PL decay could be observed at the shorter PL wavelength. Although the PLQE (7%) of the MAPbBr<sub>3</sub>/8 V GaN sample implies the dominant recombination process is the non-radiative process in this study, we could not discard the influence of the spatial confinement increasing the overlap between the electron and hole wavefunctions, and thus increasing the radiative recombination probability.<sup>202</sup> Therefore, the fast PL decay could result from the increasing non-radiative. However, we cannot rule out the contribution from the radiative recombination process at the current stage. In the future, a wavelength-dependent PLQE measurement should be carried out to distinguish the contribution from the radiative recombination process and the non-radiative recombination process.

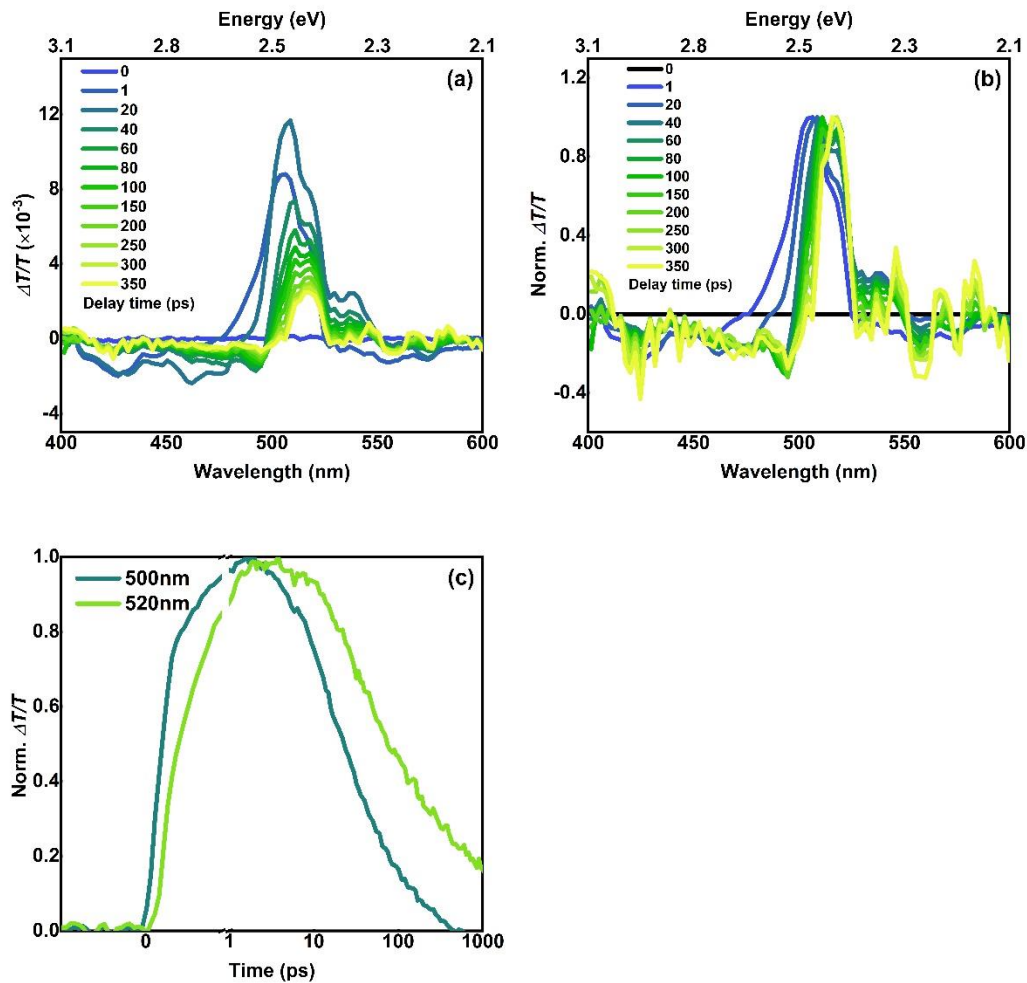


Figure 5-8 (a) Transient absorption spectra MAPbBr<sub>3</sub>/GaN sample in the first 350 ps after excitation. Nanoporous GaN substrates were treated with APTES before perovskite infiltration. The sample was pumped with a pulsed laser (1 kHz) at 400 nm (3.1 eV) at a fluence of 45.4  $\mu\text{Jcm}^{-2}$  per pulse under the ambient condition. The initial carrier density is  $7.51 \times 10^{17} \text{ cm}^{-3}$ . (b) Normalised transient absorption spectra of Fig (a). (c) Transient absorption kinetics taken at 510 nm GSB and 520 nm GSB. The GSB at 510 nm states rises simultaneously with the pump, while the rising of the 520 nm GSB is slower than that at 510 nm. The TA measurement was carried out jointly with Linjie Dai.

## **5.2.4 Charge carriers recombination in MAPbBr<sub>3</sub> in 8 V etched GaN**

We then investigate the confinement effect of GaN on the charge carrier recombination process. The PLQE we achieved with the treatment reaches 7%. Although quantum efficiency is higher than that of MAPbBr<sub>3</sub> thin film (3%), the quantum efficiency is much lower than the reported PLQE of MAPbBr<sub>3</sub> nanoparticles (83%).<sup>203</sup> Some former research attributes the low quantum yield of non-passivated nanoparticles to the localised surface traps.<sup>204</sup> To investigate the charge carriers recombination dynamics for the infiltrated perovskite, we compare the transient PL kinetic of MAPbBr<sub>3</sub>/8 V GaN with that of a bulk perovskite thin film at their emission peak in Figure 5-9.

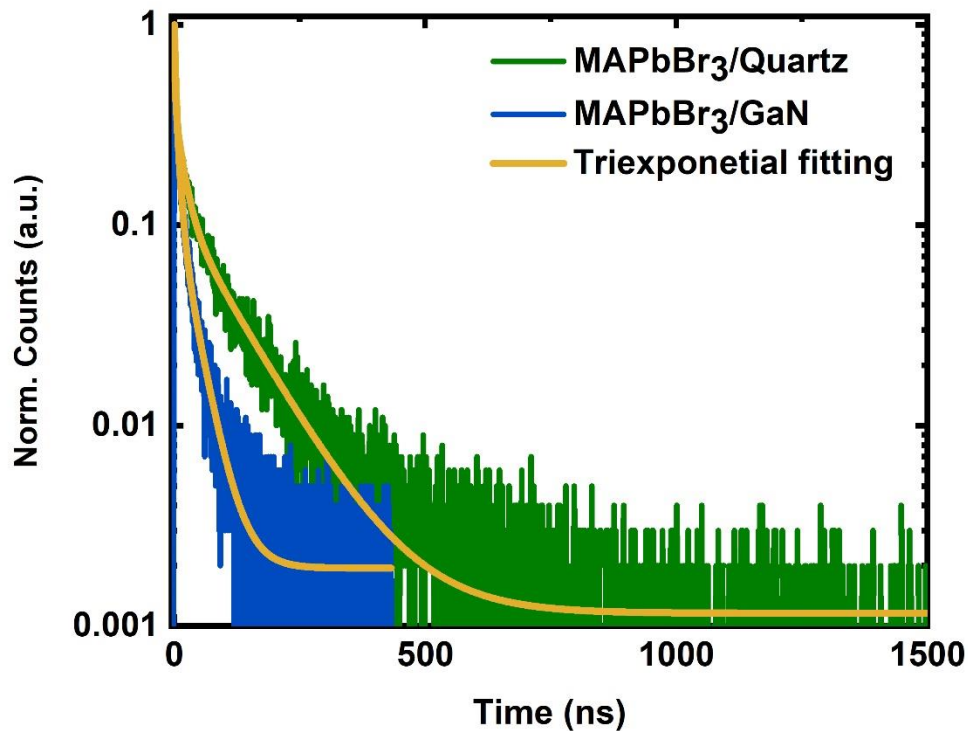


Figure 5-9 Normalised photoluminescence decay of a MAPbBr<sub>3</sub>/8 V GaN (blue line) and a MAPbBr<sub>3</sub> spin-coated thin film on quartz (green). Yellow lines indicate the triexponential function fitted results. The nanoporous GaN substrate was treated with APTES before perovskite infiltration. MAPbBr<sub>3</sub>/GaN sample was excited with a pulsed laser (2 MHz) at 407 nm (3.04 eV) at a fluence of  $7.37 \times 10^{-2} \mu\text{Jcm}^{-2}$  per pulse under ambient condition. MAPbBr<sub>3</sub> thin film sample was excited with a pulsed laser (0.5 MHz) at 375 nm (3.30 eV) at a fluence of  $1.35 \times 10^{-2} \mu\text{Jcm}^{-2}$  per pulse under ambient condition.

The PL decay is not monoexponential. In order to extract radiative and non-radiative recombination rates from the transient PL, we fit PL kinetics with the triexponential

function,

$$I_{PL}(t) = A_1 e^{-\frac{t}{\tau_1}} + A_2 e^{-\frac{t}{\tau_2}} + A_3 e^{-\frac{t}{\tau_3}} \quad (5.2)$$

The fitting result is listed in Table 5-1:

	$A_1$	$\tau_1$ (ns)	$A_2$	$\tau_2$ (ns)	$A_3$	$\tau_3$ (ns)
MAPbBr <sub>3</sub> /GaN	0.428	2.02	0.447	7.28	0.124	31.66
MAPbBr <sub>3</sub> thin film	0.598	1.69	0.267	17.16	0.122	100.39

Table 5-1 Triexponential fitting parameters from the transient photoluminescence measured with TCSPC in Figure 5-9

We can calculate the average lifetime ( $\tau_{PL}$ ) from the triexponential results according to

$$\tau_{PL} = \frac{A_1 \tau_1^2 + A_2 \tau_2^2 + A_3 \tau_3^2}{A_1 \tau_1 + A_2 \tau_2 + A_3 \tau_3} \quad (5.3)$$

We have already known the PLQE of MAPbBr<sub>3</sub>/GaN and MAPbBr<sub>3</sub> thin film is 7% and 3% respectively. By combining the average PL lifetime and the PLQE, we calculated the radiative recombination rate and non-radiative recombination rate based on equations

$$k_{PL} = k_{non-rad} + k_{rad} \quad (5.4)$$

$$PLQE = \frac{k_{rad}}{k_{non-rad} + k_{rad}} \quad (5.5)$$

$$k = \frac{1}{\tau}, \quad (5.6)$$

where  $k_{PL}$  is the average recombination rate,  $k_{non-rad}$  is the non-radiative recombination rate and  $k_{rad}$  is the radiative recombination rate. The recombination rate equals the reciprocal of a lifetime. The calculated results are listed in Table 5-2.

	$\tau_{PL}$ (ns)	$k_{PL}$ ( $s^{-1}$ )	$\tau_{rad}$ (ns)	$k_{rad}$ ( $s^{-1}$ )	$\tau_{non-rad}$ (ns)	$k_{non-rad}$ ( $s^{-1}$ )
MAPbBr <sub>3</sub> / GaN	18.62	$5.37 \times 10^7$	266.02	$3.76 \times 10^6$	20.02	$4.99 \times 10^7$
MAPbBr <sub>3</sub> thin film	73.45	$1.36 \times 10^7$	2448.44	$4.08 \times 10^5$	75.73	$1.32 \times 10^7$

Table 5-2 Calculated recombination constants from the recombination rates measured with TCSPC in Figure 5-9.

We know from the calculation that both radiative and non-radiative recombination rates increase when MAPbBr<sub>3</sub> is confined in the nanoporous GaN comparing to bulk perovskite thin film. Considering the low PLQE of perovskite in GaN, the shorter non-radiative lifetime we observe in Figure 5-9 could result from increasing surface trap states when the crystal size decreases. Therefore, we suggest that the surface of MAPbBr<sub>3</sub> nanoparticles are not effectively passivated, and the dominant non-radiative recombination process leads to low quantum efficiency. In the future, the perovskite surface defect passivation method should be explored to improve quantum efficiency.

In addition to the higher non-radiative recombination rate, perovskite nanocrystals inside the GaN matrix also show an increasing radiative recombination rate comparing

to the bulk perovskite. It could be caused by enhanced charge carrier recombination in perovskite in nanopores. To verify this hypothesis, we investigate the recombination mechanism of MAPbBr<sub>3</sub> in nanoporous 8 V etched GaN. We measured PL spectra of MAPbBr<sub>3</sub>/GaN sample under elevated excitation fluence at 400 nm to determine the dominant radiative recombination process in MAPbBr<sub>3</sub> inside porous GaN. The integrated PL intensity as a function of the excitation fluence was plotted in a double-logarithmic scale in Figure 5-10. We calculated the initial carrier density from the absorption of the sample and the laser fluence

$$n_0 = \frac{a \cdot P}{E_{ph} \cdot f} \cdot \frac{1}{\pi \left(\frac{d}{2}\right)^2 \cdot t}, \quad (5.7)$$

where  $a$  is the absorption of the sample,  $P$  is the power of the laser,  $E_{ph}$  is the photon energy of the laser,  $f$  is the frequency of the laser,  $d$  is the laser beam diameter, and  $t$  is the sample thickness. We used the calculated effective perovskite thickness (46 nm) from Chapter 4 in this case.

Generally, the integrated PL intensity ( $I$ ) increases linearly with the pump fluence ( $P$ ) under  $20 \mu\text{Jcm}^{-2}$  per pulse ( $I \sim P^1$ ). Schmidt et al. suggested that the integrated PL intensity  $I$  is proportional to  $P^K$ , where  $P$  is the excitation fluence. The exponent  $K$  is related to the dominant radiative recombination mechanism. When  $K$  is close to 1, it suggests a monomolecular recombination process is the dominant radiative recombination. When  $K$  is around 2, it suggests a bimolecular recombination process is the dominant radiative recombination.<sup>205</sup> In this experiment,  $K = 1$  suggests the

radiative recombination involves single electron-hole pairs.

At higher excitation fluence than  $20 \mu\text{Jcm}^{-2}$  per pulse, the integrated PL intensity increases sub-linearly as a function of the excitation fluence ( $I \sim P^{0.47}$ ). In Section 5.2.2, we calculated the  $\text{MAPbBr}_3$  nanocrystal diameter to be between 8 nm and 9.5 nm. Therefore, we use the average diameter, 9 nm, to calculate the average nanocrystal volume,  $1.8 \times 10^{-18} \text{ cm}^3$ . According to the calculated average nanocrystal volume, the charge carrier density should be around  $6 \times 10^{17} \text{ cm}^{-3}$  for multiple photon absorption to happen on a single nanocrystal. The charge carrier density is calculated by dividing the initial carrier density by the nanocrystal volume. In the fluence dependent PL measurement, the sublinear increase starts at a carrier density of  $3.98 \times 10^{17} \text{ cm}^{-3}$  per pulse, which is consistent with the calculated carrier density for multiple photon absorption to happen. Therefore, we attribute this sublinear increase to the absorption of multiple photons on a single perovskite nanocrystal at a high excitation density. When multiexciton is generated on a single nanocrystal, Auger recombination, which is a non-radiative recombination process, will take place, shown as a reduction in PLQE and a roll-off in luminescence in fluence-dependent PL measurement. Since no redshift in PL spectra is observed in this measurement, we rule out the impact of perovskite nanocrystals aggregation under intense laser illumination on the roll-off in PL and attribute the sublinear increase in the fluence dependent PL measurement to multiexciton recombination process.

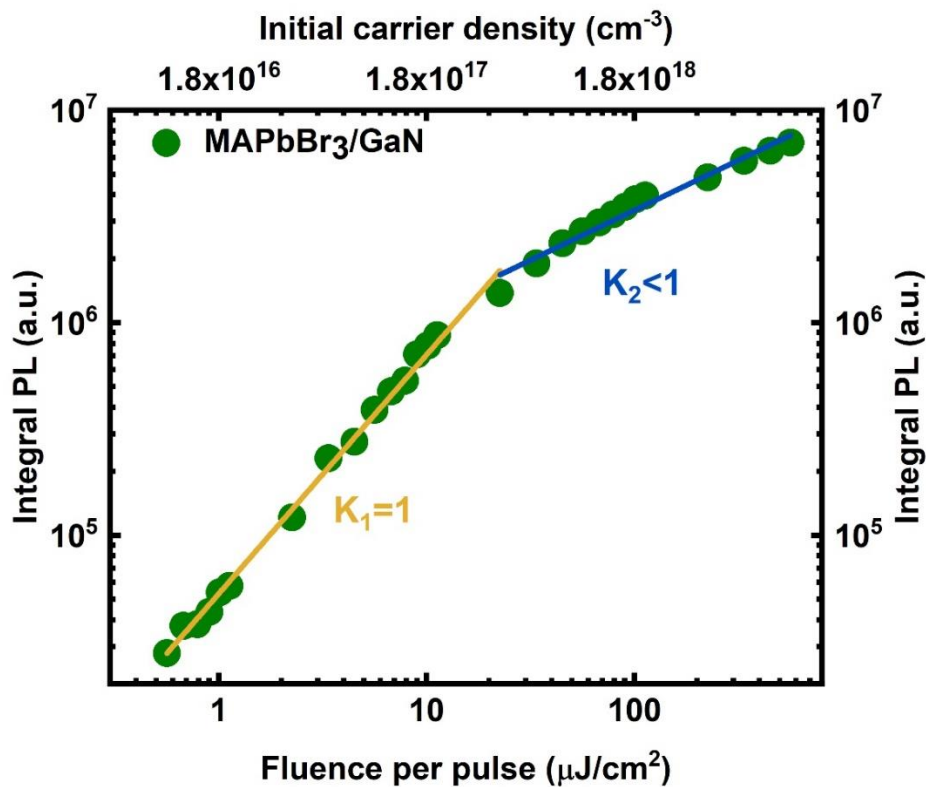


Figure 5-10 Logarithm plot of the integrated PL intensity (integrated from 450 nm (2.76 eV) to 600 nm (2.06 eV)) versus excitation fluence of encapsulated MAPbBr<sub>3</sub>/GaN sample. The initial charge carrier density was calculated from the absorption of the sample and the laser fluence. Nanoporous GaN substrates were treated with APTES before perovskite infiltration. The sample was encapsulated with epoxy and glass in the nitrogen-filled glovebox. The sample was excited with a pulsed laser (1 kHz) at 400 nm (3.1 eV) at fluences from 0.6 μJcm<sup>-2</sup> per pulse to 500 μJcm<sup>-2</sup> per pulse at room temperature. PL signal was collected with a CCD detector. The fitting of the data is indicated by the yellow line and green line. The integrated PL intensity increases linearly to the excitation fluence before 30 μJcm<sup>-2</sup> and increases sublinearly to the excitation fluence at higher fluence.

It has been reported that the dominant radiative recombination process in bulk MAPbBr<sub>3</sub> at room temperature is the free charge carrier recombination due to the low exciton binding energy of MAPbBr<sub>3</sub>.<sup>40</sup> However, the dominant radiative recombination process in this research is exciton recombination. We attribute this different behaviour to bulk perovskite to the localisation of charge carriers in MAPbBr<sub>3</sub> nanocrystals inside nanoporous scaffolds. The size reduction spatially confines excitons in nanocrystals. The quantum confinement and dielectric confinement of GaN will enhance the interaction between free electrons and holes. Therefore, the binding energy of carriers is more significant, making the exciton recombination the dominant process, shown as the increase in radiative recombination rate in Table 5-2. In this case, the GaN matrix can enhance charge carrier interaction in perovskite nanocrystals via spatial confinement and increase the carrier binding energy.

## 5.3 Conclusion and Future Work

In this chapter, we resolved the confinement effect of the nanoporous GaN matrix on MAPbBr<sub>3</sub> perovskite. Nanopores GaN confines the growth of perovskite crystals inside. The spatial confinement enhances the Coulomb interaction between charge carriers, leading to a blue shift in photoluminescence comparing to the bulky MAPbBr<sub>3</sub>. The enhanced charge carrier interaction also results in the exciton dominant radiative recombination process in MAPbBr<sub>3</sub> nanocrystals at room temperature. These results suggest that the nanoporous GaN matrix increases the binding energy of carriers in perovskite nanocrystals, allowing a more efficient radiative recombination process to happen. We hope that the promising optoelectronic properties of the confined perovskite could combine with the remarkable conductivity of GaN to make them valuable materials for light emitting applications in the future.

We expect that further perovskite surface passivation could improve the light emitting performance in the future. Currently, the low photoluminescence quantum efficiency resulting from defect states of nanocrystals still hinders advancing the composite to applications in light-emitting devices. Therefore, efficient surface passivation methods should be explored to improve photoluminescence efficiency in the future.

Additionally, the energy transfer process between perovskite and GaN should be investigated in the future. GaN has energy states in between the conduction band and valence band. However, whether these states will quench the luminescence of

perovskite has not been investigated yet. This research is essential in achieving efficient luminescence from perovskite in the future.

# Chapter 6 Synthesis of Two-dimensional Perovskite with Polyaromatic Hydrocarbon Compounds

Two dimensional (2D) organic-inorganic hybrid perovskites have revealed their potential in light-emitting diode due to the large exciton binding energy, natural multi-quantum well structure and outstanding stability in the ambient environment. The less size restriction on spacer organic cations opens up an opportunity to introduce large polyaromatic hydrocarbon compounds into the perovskite structure. In this chapter, we demonstrate a solution-processed method to synthesis 2D perovskite with bis(propargyl ammonium iodide) anthracene (BPAIA) and 2,6-dimethylammoniumnaphthalene (DMAN) separately. However, due to the steric effect, phase pure BPAIA perovskite was not achieved. Although the structural and optical characterization of the BPAIA perovskites suggests the formation of 2D perovskite, unreacted precursors were also observed in this study. Besides, we successfully synthesized 2D Dion-Jacobson DMAN perovskite, presenting a new type of 2D perovskite for light emitting applications.

## 6.1.1 Background and Motivation

Hybrid lead halide perovskites have shown their remarkable potential in optoelectronic applications in the past decades. A general formula of three-dimensional (3D) hybrid perovskite is  $ABX_3$ , in which A is the monovalent central organic cation, such as methylammonium ( $MA^+$ ), formamidinium ( $FA^+$ ) and  $Cs^+$ ; B is the bivalent metal ion, such as  $Pb^{2+}$  and  $Sn^{2+}$ ; X is halide anion, such as  $Cl^-$ ,  $Br^-$  and  $I^-$ .<sup>206</sup>

3D perovskites have been enormously investigated and applied in optical-electronic devices, such as photovoltaic devices<sup>207</sup>, light-emitting diodes<sup>8</sup>, and lasers<sup>11</sup>. Despite their outstanding performance, 3D perovskites suffer from poor stability in the ambient atmosphere. Meanwhile, two-dimensional (2D) perovskites formed by reducing the crystal dimension of 3D perovskite chemically show superior stability in the ambient atmosphere and become particularly attractive for the next generation semiconductor<sup>91</sup>.

A general formula of 2D hybrid perovskite is  $(A')_m(A)_{n-1}B_nX_{3n+1}$ , in which A' is organic monovalent or bivalent cations intercalated between the anions of 2D perovskite sheets.

In 2D perovskite, the A' organic cation works as an insulating barrier that confines carriers in two dimensions. Depending on the organic spacer group, 2D perovskite can be classified into three phases, the Ruddlesden-Popper (RP) phase<sup>91</sup> and Dion-Jacobson (DJ) phase<sup>93</sup>. The RP phase perovskite is a dominant phase of 2D perovskite. In the RP phase 2D perovskite, two layers of A' cations, commonly monovalent ammonium cations ( $RNH_3^+$ ), pack between the inorganic layers with an offset per unit cell. In the

DJ phase 2D perovskite, a single layer of A' cations, commonly bivalent ammonium cations, packs between the inorganic layers. The 2D DJ phase perovskite layers stack with either perfect alignment or a minor misalignment depending on the spacer cation, making it more stable against humidity than the RP phase perovskite<sup>93</sup>. Besides, in the DJ phase perovskite, inorganic layers are directly connected with bifunctional species. Consequently, the out-of-plane charge transport ability is enhanced compared with the RP phase perovskite<sup>208</sup>, as the out-of-plane charge transport in RP phase perovskite is hindered by the gap between two organic layers. Therefore, the DJ phase perovskite has the potential to achieve more stable devices with better efficiency in the ambient atmosphere. However, the influence of the gap between organic layers on the confinement effect on perovskite is still not clear. Therefore, we synthesis a new DJ phase perovskite base on naphthalene, hoping to investigate the confinement effect difference between a DJ phase and an RP phase perovskite based on naphthalene in the future.

2D perovskites have far fewer size restrictions on A' cation. However, the A' cation must be able to fit into the interlayer space. A' cation's suitability is determined by its stereochemical configuration, space-filling ability, hydrogen-bond capacity, and degree of substitution<sup>206</sup>. In this case, the coupling of divalent cations into the inorganic perovskite sheet is less preferred than two layers of monovalent cations. In former research, DJ phase perovskite based on 1,4-phenylenedimethan ammonium<sup>137</sup>, 5,5'-bis(aminoethyl)-2,2':5',2'':5'',2'''-quaterthiophene<sup>209</sup>, N,N-dimethyl-p-

phenylenediammonium<sup>210</sup> and 2,5-thiophenedimethylammonium<sup>138</sup> have been successfully synthesized. However, most compounds function as a spacer group to form the two-dimensional perovskite structure. Functional organic compounds, such as anthracene, have not been applied in 2D perovskite synthesis before. Therefore, we would like to prepare a 2D perovskite based on anthracene to study whether the functional compound only acts as a spacer group or it would have its own photophysical property in the perovskite structure. In this chapter, we synthesis DJ phase 2D perovskite from naphthalene and anthracene to explore the aromatic hydrocarbon cations for 2D DJ phase perovskite synthesis.

## 6.2 Results and Discussion

### 6.2.1 Properties of Bis(propargyl ammonium iodide) anthracene (BPAIA)

We used the bis(propargyl ammonium iodide) anthracene (BPAIA) as the A' spacer cation to synthesize 2D DJ phase perovskite. The BPAIA was synthesized by John Anthony's group at the University of Kentucky. Figure 6-1 shows its chemical structure. The ammonium iodide groups are connected to the anthracene with a carbon-carbon triple bond on position 9, 10 of the anthracene.

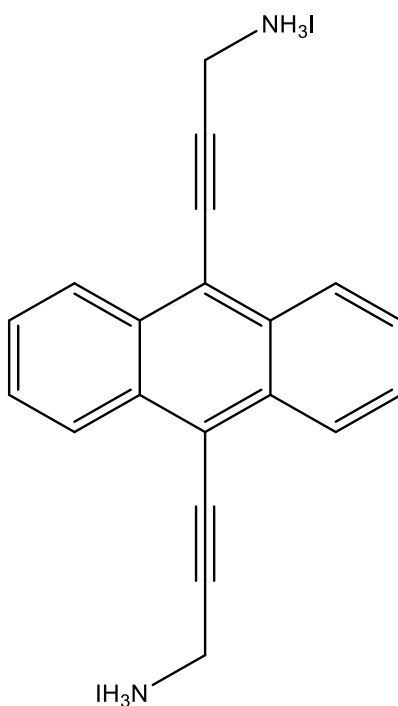


Figure 6-1 Chemical structure of bis(propargyl ammonium iodide) anthracene (BPAIA)

BPAIA is a functional organic compound. We measured its steady-state absorption and

photoluminescence (PL) spectra of a spin-coated BPAIA thin film (Figure 6-2). The absorption of BPAIA reveals three peaks at 396 nm (3.13 eV), 419 nm (2.95 eV) and 448 nm (2.76 eV). When the BPAIA was excited at 380 nm with a Xe lamp, we observed three PL peaks at 448 nm (2.77 eV), 472 nm (2.63 eV) and 501 nm (2.48 eV) correspondingly. According to the literature, the absorption and PL peaks originates from spin allowed singlet-singlet transition in anthracene. They are assigned to vibronic transitions, 0-0 transition, 0-1 transition and 0-2 transition among the vibronic bands.<sup>211</sup>

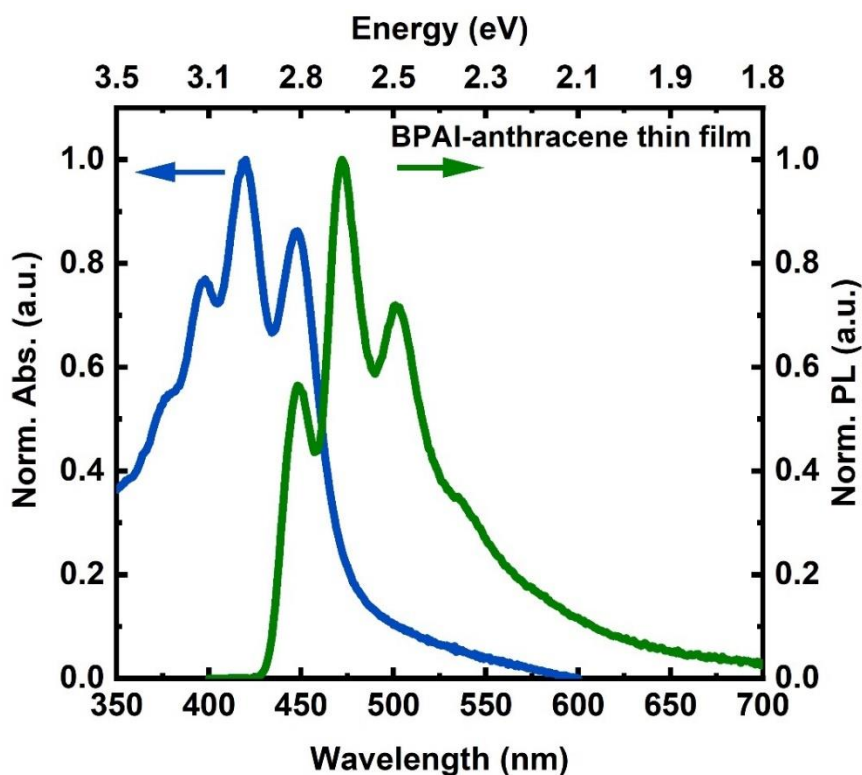


Figure 6-2 Normalised steady-state absorption (blue line) and photoluminescence spectra (Green line) of the BPAIA spin-coated thin film in the ambient environment. For the PL measurement, the sample was excited at 380 nm with a Xe lamp in the ambient atmosphere.

## 6.2.2 Structural Study of the Synthesized Mixture

BPAIA perovskite thin film was prepared with the method described in Section 3.1.4 in Chapter 3. However, impurities composing of unreacted precursors were also observed. We took the X-Ray diffraction of the synthesized mixture at room temperature to study its structural properties (Figure 6-3). The XRD for our sample exhibits pronounced peaks at the diffraction angle  $2\theta$  at  $8.26^\circ$ ,  $16.54^\circ$  and  $24.86^\circ$ , which can be indexed as the (0 0 2), (0 0 4) and (0 0 8) lattice reflections of the  $n=1$  BPAIA lead iodide perovskite according to literature<sup>212</sup>. From the low angle reflection peak at  $2\theta=8.26^\circ$ , we calculated the inorganic-organic layer thickness to be  $d=10.68 \text{ \AA}$ . Therefore, we confirm that an  $n=1$  BPAIA lead iodide perovskite with a unit cell dimension of  $10.68 \text{ \AA}$  is synthesized. However, the low intensity of the XRD peaks indicates poor crystallinity of the perovskite. In addition to diffraction peaks of the synthesized perovskite, we also observe strong diffraction peaks of  $\text{PbI}_2$  at  $2\theta=12.72^\circ$ ,  $38.72^\circ$  and  $42.01^\circ$ , which demonstrates the existence of excess  $\text{PbI}_2$  on the synthesized thin film.

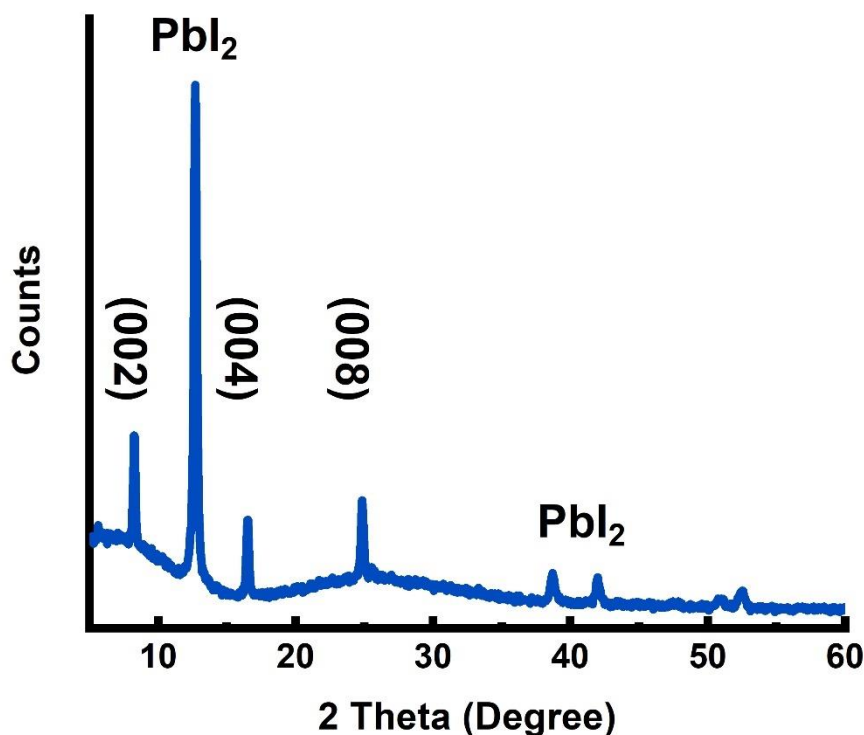


Figure 6-3 X-Ray diffraction of the synthesized BPAIA perovskite with precursors on quartz at room temperature.

### 6.2.3 Optical Properties of the Synthesized Mixture

We then investigated the optical properties of the synthesized thin film. Figure 6-4 shows the normalised UV-Visible absorption and photoluminescence spectra of the thin film. The sample has a sharp absorption edge at 529 nm, suggesting the formation of the excitonic state. The two absorption peaks at 418 nm and 448 nm match the absorption of the pristine BPAIA thin film plotting in Figure 6-2. The PL spectrum was measured from the front side of the sample, indicated by the inset in Figure 6-4. The emission of the sample is very broad, ranging from 423 nm to 800 nm. Three PL peaks

are observed at 444 nm, 469 nm and 527 nm. Comparing with the absorption and PL spectra of the pristine BPAIA thin film in Figure 6-2, we attribute the absorption peak at 418 nm and 448 nm, as well as PL peaks at 444 nm and 469 nm, to the excess anthracene on the prepared thin film.

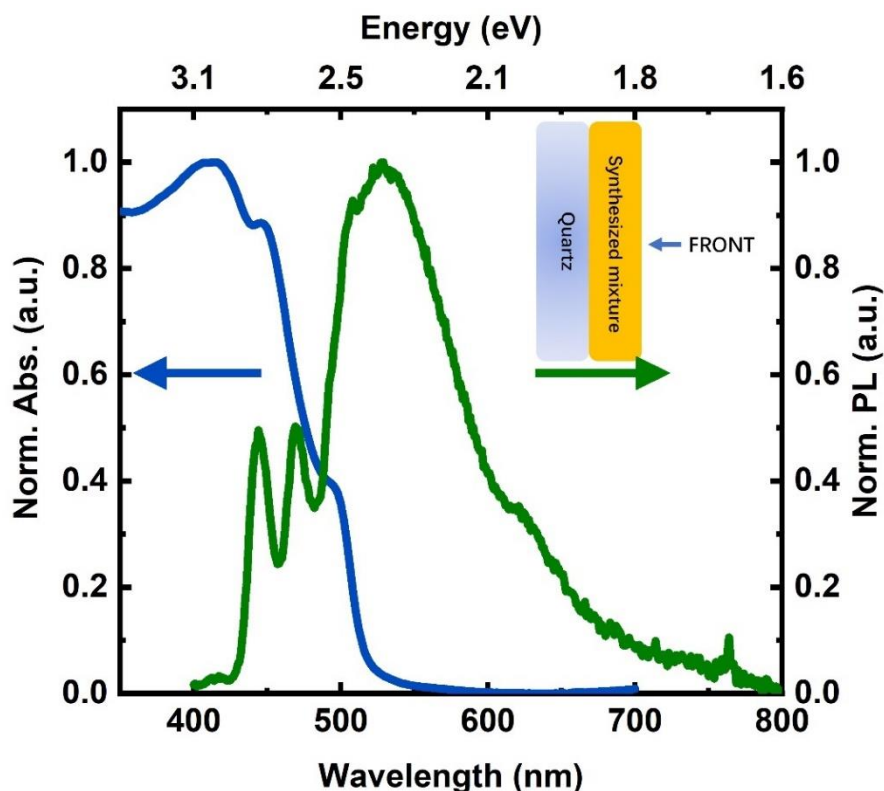


Figure 6-4 Normalised steady-state absorption and photoluminescence spectra of the synthesized BPAIA perovskite and precursors on quartz. Blue line: normalised absorption spectrum measured with UV-Visible absorption spectrometer in the ambient atmosphere; Green line: normalised photoluminescence measured with a fluorometer, the sample was excited at 380 nm with Xe lamp in the ambient atmosphere. The excitation and PL signal collection were from the front side of the sample. Inset: Illustration of front side excitation for PL measurement.

We attribute the broadband emission centred at 527 nm to the synthesized BPAIA lead iodide perovskite, as we observed in the structural study. The FWHM of the broadband emission is 89 nm. In recent years several 2D perovskites with broadband emission have been reported, such as (N1-methylethane-1,2-diammonium)PbBr<sub>4</sub><sup>213</sup>, (2,2'-(ethylenedioxy)bis(ethylammonium))PbBr<sub>4</sub><sup>214</sup>, (2-(dimethylamino)ethylamine)PbBr<sub>4</sub>, (3-(dimethylamino)-1-propylamine)PbBr<sub>4</sub> and (4-dimethylaminobutylamine) PbBr<sub>4</sub><sup>215</sup>. According to the literature, the broad PL emission is due to the large octahedral distortion of the inorganic framework. With a larger distortion, a broader PL emission will be observed<sup>215</sup>. The distortion of the inorganic layer also leads to self-trapping excitonic states (Figure 6-5), resulting in white light emission<sup>214</sup>. According to the force-field modelling shown in Section 6.2.7, the anthracene is larger than the perovskite lattice diagonal. Therefore, to fit in the anthracene, the lead iodide framework needs to distort from its original position. We propose that the broadband PL is due to the distortion of the lead iodide framework. The recombination dynamic behind the self-trapping emission needs to be investigated in the future.

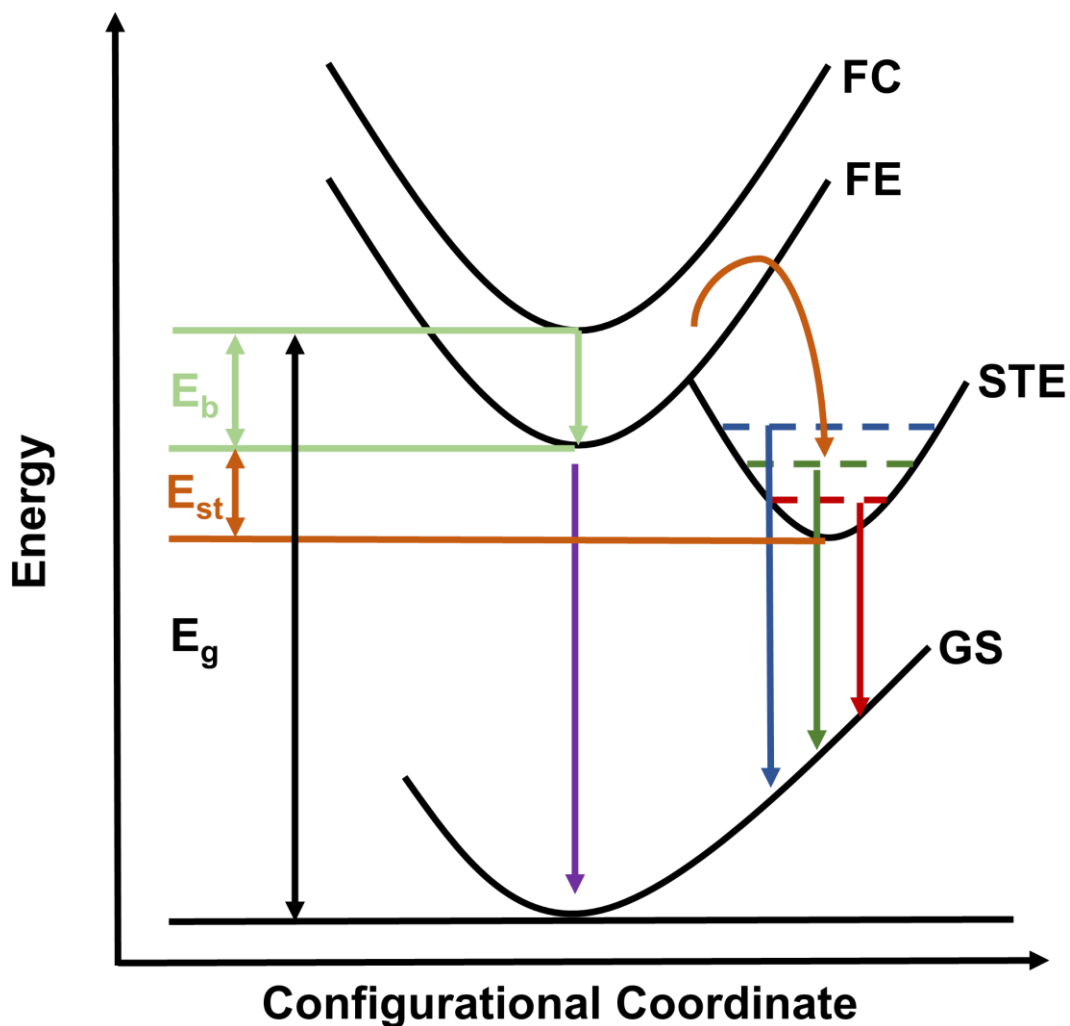


Figure 6-5 A schematic of the self-trapping excitonic states (STE: self-trapping exciton, FC: Free carrier state, FE: free exciton state, GS: ground state,  $E_b$ : binding energy,  $E_{st}$ : self-trapping energy,  $E_g$ : bandgap energy).

We also measured the PL from the backside of the sample (Figure 6-6), indicated by the inset in Figure 6-6. We normalized PL spectacle to the broad PL peak at 527 nm. Two spectra overlap with each other at the red edge, while no anthracene PL character peaks at 444 nm and 469 nm are detected from the backside.

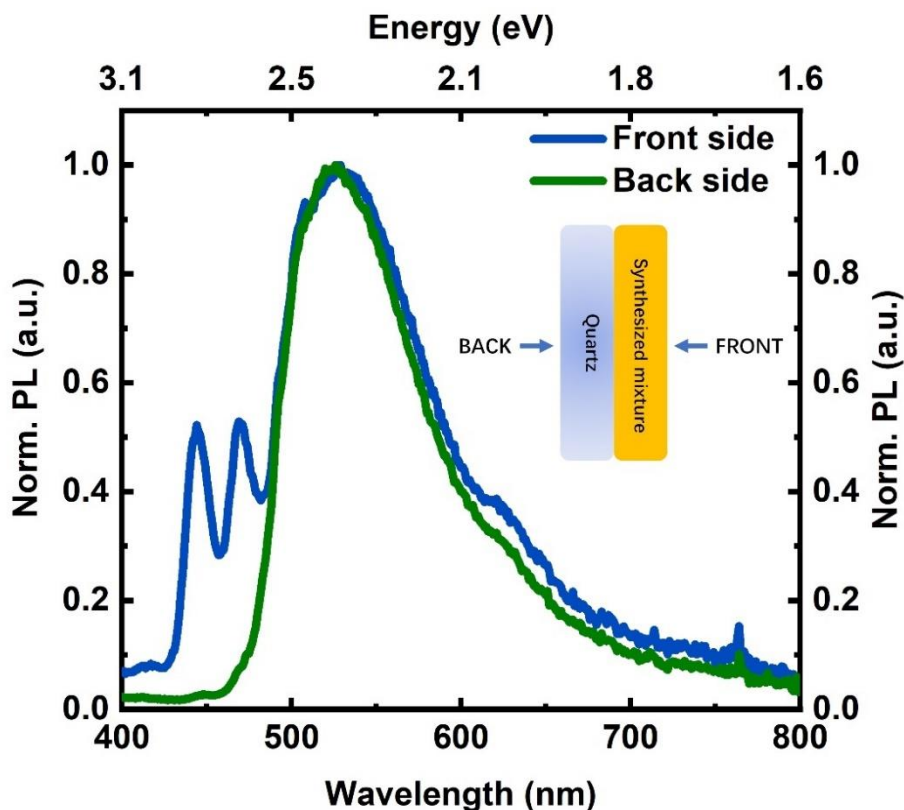
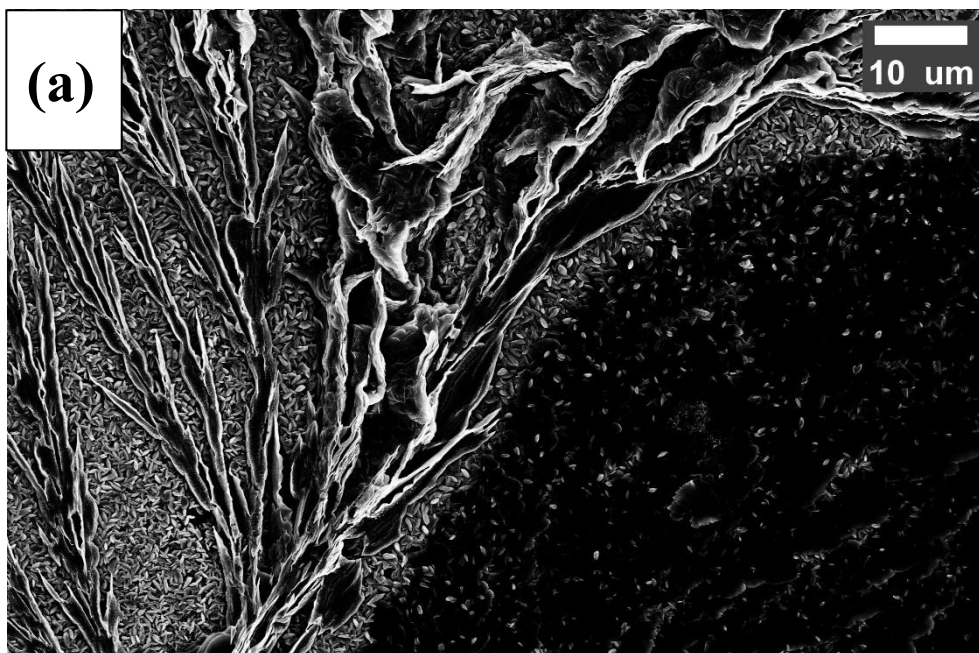


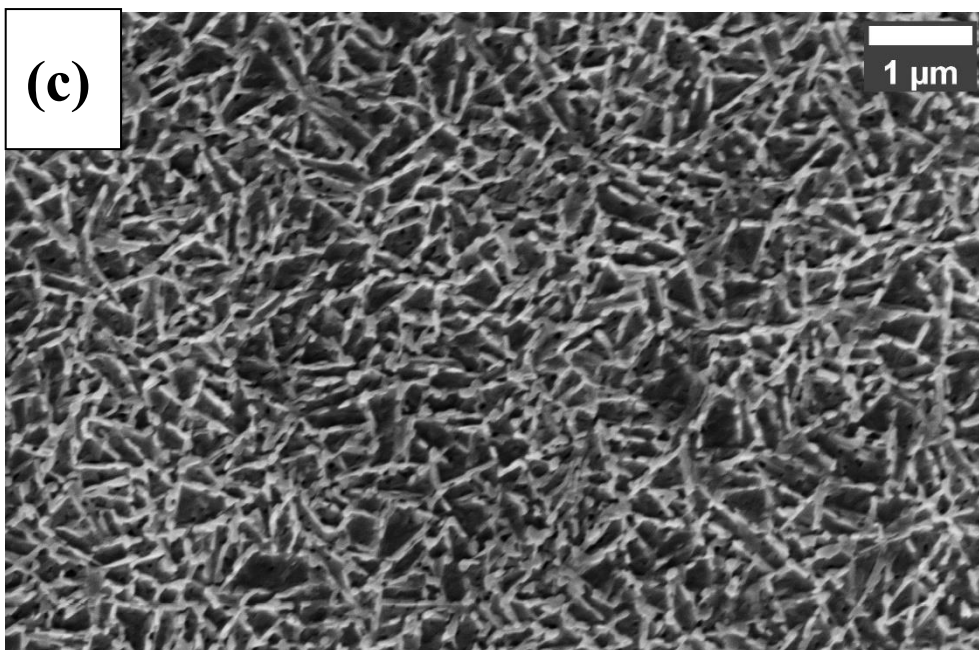
Figure 6-6 Normalised photoluminescence spectra of the synthesized mixture measured from the front side (blue line) and backside (green line). Normalised photoluminescence was measured with a fluorometer in the ambient atmosphere. The sample was excited at 380 nm with a Xe lamp. Inset: Illustration of front side excitation and backside excitation for the PL measurement.

## 6.2.4 Morphology of the Synthesized Mixture

We take the top-view scanning electron microscope (SEM) of the synthesized mixture to investigate its morphology. The morphology of the sample surface is very uneven. We distinguish three characters from the SEM image: a widespread dendritic solid with a length of hundreds of micrometres on the top layer, plate shape crystals with a

thickness of  $\sim 200$  nm and needle shape crystals with a length of  $\sim 1$   $\mu\text{m}$ . Different morphologies suggest the prepared sample is not phase pure and is a mixture of three components. Comparing with the top-view SEM of BPAIA thin film and  $\text{PbI}_2$  thin film in Figure 6-7, we infer that the widespread dendritic solid could be the excess BPAIA, which matches the BPAIA PL observed from the front side of the sample. The needle shape crystals are the extra  $\text{PbI}_2$  thin film at the bottom, which is demonstrated by the XRD. Therefore, the plate shape crystal should be the synthesized BPAIA 2D perovskite crystals. In addition to the formation of new phases, SEM is in accordance with what we observed in the XRD and PL, that both unreacted BPAIA and  $\text{PbI}_2$  are mixed together with the perovskite.





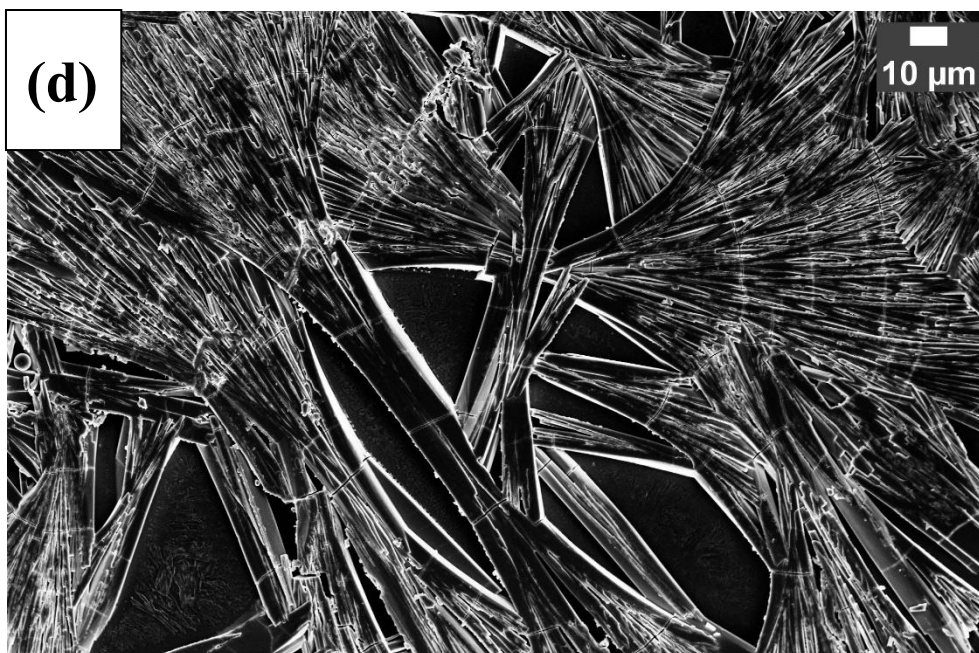


Figure 6-7 Top-View scanning electronic microscope (SEM) image of :(a) and (b): the synthesized mixture, (a): scale bar 10μm (b): scale bar 1μm; (c) spin-coated PbI<sub>2</sub> thin film, scale bar: 1μm; (d) spin-coated BPAIA thin film, scale bar: 10μm

## 6.2.5 Local photoluminescence of the Synthesized Mixture

As shown in Figure 6-8, we excited the sample at 509 nm from the front side to ensure only the BPAIA perovskite was excited and measured the PL mapping of an area of 625 μm<sup>2</sup>. The yellow colour indicates regions where the sample emits, while the blue part shows the dark area. The local PL colour map suggests that the distribution of synthesized perovskite is random, and full coverage cannot be achieved. The uneven luminescence of the sample also relates to the incomplete reaction of BPAIA and PbI<sub>2</sub>, and the formation of perovskite is random in different areas. Combined with the

morphology study and structural study, we surmise that perovskite formation with BPAIA is not preferred.

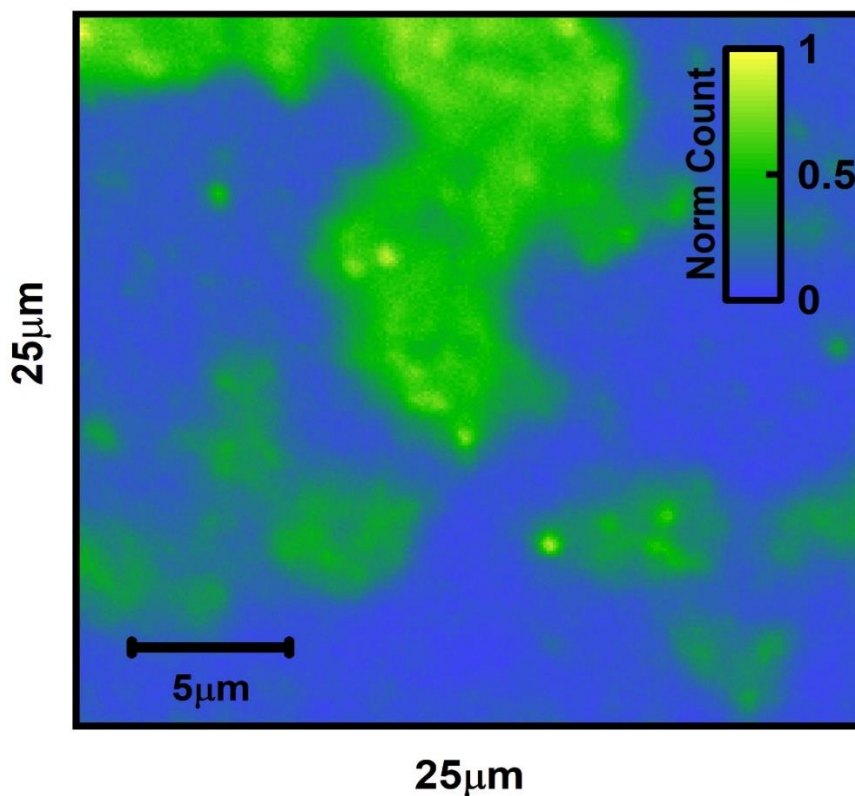


Figure 6-8 Hyperspectra photoluminescence image of the encapsulated synthesized mixture. Images were taken using a hyperspectra PL microscope. The sample was encapsulated with epoxy and glass in the nitrogen-filled glovebox. The sample was excited with a 509 nm continuous wave laser with an excitation intensity of  $100 \text{ mW/cm}^2$ . Hyperspectra images were measured using an IMA-VIS system (Photon etc.). The measurement was carried out jointly with Dr Krzysztof Galkowski.

## 6.2.6 Force-field Modelling of the BPAIA 2D Perovskite

To investigate the reason for the unpreferred reaction, we run a force-field modelling of the BPAIA based layered perovskite structure. In Figure 6-9, the red-grey ball-and-stick model is the inorganic lead iodide framework, and the blue-grey ball-and-stick model is the BPAIA packed in between the framework. According to the modelling, the building block of anthracene is larger than the perovskite lattice diagonal. Thus neighbouring anthracenes would need to overlap into a zipper-like structure with less than 3 Å distance. Therefore, the repulsion between organic cations is too large that the crystal structure is very unstable, making the formation of perovskite unpreferred.

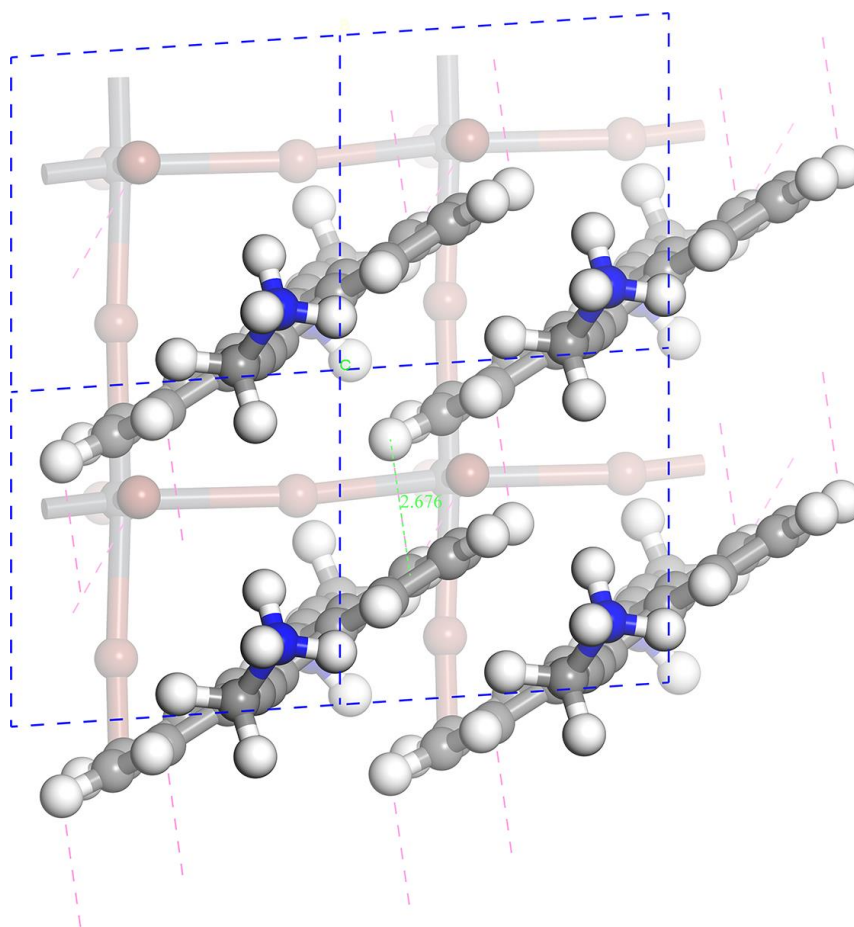


Figure 6-9 Force-field modelling of a (BPAIA)PbI<sub>4</sub> 2D perovskite. The red-grey ball-and-stick model indicates the inorganic lead iodide framework, and the blue-grey ball-and-stick model suggests the BPAIA packed in between the framework. The simulated distance between two BPAIA molecules is 2.676 Å. The simulation was carried out by Dr Florian Auras.

The simulation demonstrates that the synthesis of BPAIA 2D perovskite is not preferred due to the significant repulsion between BPAIA molecules in the organic spacer layer. Since the substitution for BPAIA is at position 9,10, when coupling into the lead iodide framework, the width of the anthracene is essential. According to the modelling, the

rigid anthracene structure is too wide for the lead iodide inorganic framework, making the perovskite structure very unstable. Therefore, we anticipate that to synthesis 2D perovskite with anthracene, the substitution needs to be on position 2,6 on anthracene to avoid the significant repulsion between anthracenes.

### 6.2.7 Synthesis of 2D DJ Phase Perovskite with 2,6-dimethylammoniumnaphthalene (DMAN)

We also synthesized 2D perovskite with 2,6-dimethylammoniumnaphthalene (DMAN) (Figure 6-10) with the method described in Section 3.1.5 Chapter 3. Via the one-step deposition method, we successfully synthesized 2D DJ phase (DMAN)PbI<sub>4</sub> perovskite

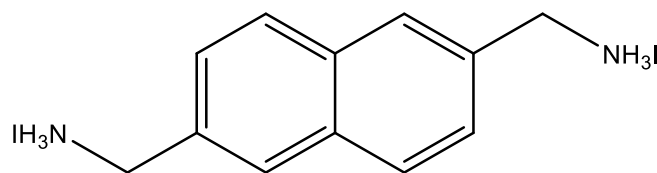


Figure 6-10 Chemical structure of the 2,6-dimethylammoniumnaphthalene (DMAN)

### 6.2.8 Structural Study of the 2D (DMAN)PbI<sub>4</sub> Perovskite

The crystal structure of the 2D DMAN perovskite was investigated with X-ray diffraction (XRD) (Figure 6-11). The reflections of the measured sample were indexed as an analogy to the 1,4-phenylenedimethan ammonium lead iodide 2D DJ phase perovskite, whose XRD has been reported by Li et al.<sup>137</sup>. The XRD reveals low angle reflection below 10°, suggesting the formation of a low dimensional structure. The low

angle reflection at  $\sim 6.07^\circ$  may be associated with the (002) lattice reflection of the 2D perovskite, and the unit cell dimension is  $d=14.5 \text{ \AA}$ . We also notice a dominant lattice reflection at  $14.59^\circ$ , which is constant with the reported DJ phase perovskite XRD<sup>137</sup>. To further confirm the crystal structure of the prepared thin film, we will need to carry out XRD measurement on the single crystal synthesized from DMAN and lead iodide in the future. However, the current XRD result only demonstrates that a low dimensional crystal with a similar crystal structure to the reported 2D DJ phase phenylenedimethan ammonium (PDMA) lead iodide can be synthesized via a solution-processed method.

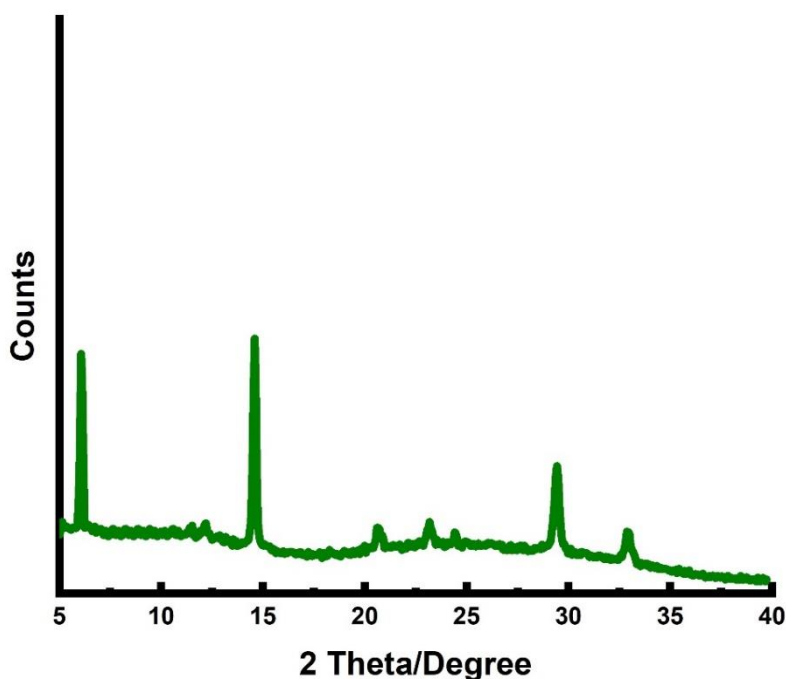


Figure 6-11 X-Ray diffraction of the (DMAN)PbI<sub>4</sub> DJ phase perovskite on quartz at room temperature.

## 6.2.9 Optical Properties of the (DMAN)PbI<sub>4</sub> Perovskite

We know from the XRD measurement that a thin film with a low dimensional structure has been prepared. We use the steady-state UV-Visible absorption and photoluminescence (PL) spectra to study the nature of the material (Figure 6-12). The absorption reveals an excitonic peak at 508 nm (2.44 eV), which is a typical feature for  $n=1$  quantum well perovskite. The PL spectra for the (DMAN)PbI<sub>4</sub> perovskite displays a peak at 520 nm (2.38 eV), which is the same as the reported (1,4-phenylenedimethan ammonium)PbI<sub>4</sub> DJ perovskite. Therefore, combining with the XRD, we suggest that we have synthesized (DMAN)PbI<sub>4</sub> DJ phase perovskite. The excitonic character of (DMAN)PbI<sub>4</sub> perovskite suggests its potential to be applied in the light-emitting diode.

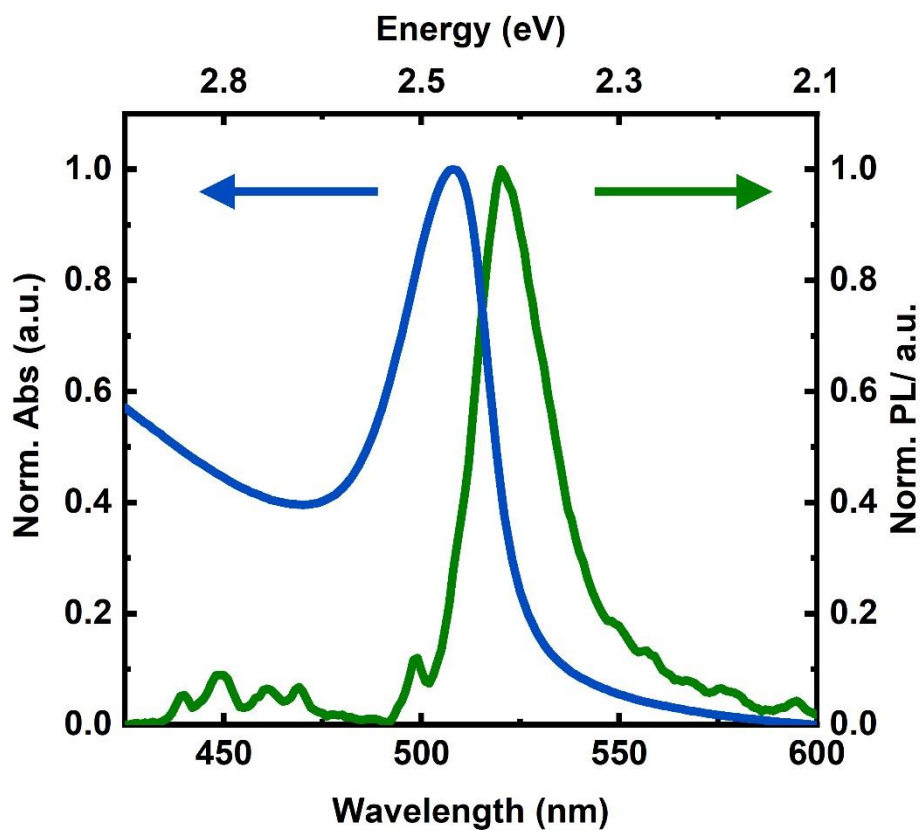


Figure 6-12 Normalised steady-state absorption and photoluminescence spectra of the (DMAN)PbI<sub>4</sub> perovskite. Blue line: normalised absorption spectrum measured with UV-Visible absorption spectrometer in the ambient atmosphere; Green line: normalised photoluminescence measured with a fluorometer. The sample was excited at 400 nm with a Xe lamp in the ambient atmosphere.

## 6.3 Conclusion and Future Work

In this chapter, we describe the synthesis of two-dimensional bis(propargyl ammonium iodide) anthracene (BPAIA) lead iodide perovskite and two-dimensional (2,6-dimethylammoniumnaphthalene) DMAN lead iodide perovskite via a solution-processed method. The synthesized BPAIA lead iodide thin film is not phase pure. Excess precursors are observed from the structural and optical characterization. The force-field modelling of the perovskite demonstrates that a significant repulsion exists between adjacent anthracene molecules, leading to an unstable crystal structure. The inorganic framework distortion caused by the steric effect of anthracenes leads to a broadband emission of the BPAIA lead iodide perovskite. Therefore, BPAIA is not a proper compound to study the influence of functional organic compounds on low dimensional perovskite. In order to solve this problem, we will need to replace BPAIA with functional compounds that can fit into the inorganic framework, such as pyrene or 2,6-substituted anthracene, in the future.

In addition to the BPAIA lead iodide perovskite, we also synthesise DMAN lead iodide perovskite via the one-step deposition method. The DMAN lead iodide perovskite reveals a structural character of the reported Dion-Jacobson perovskite<sup>137</sup> and exhibits excitonic character in the steady-state absorption and PL. However, the crystal structure of the compound is not clear, which will be studied in further research. In addition, we will also compare the out-of-plane charge transport ability of the (DMAN)PbI<sub>4</sub>

perovskite with other naphthalene, such as 2-(2-naphthyl)ethan ammonium lead iodide RP phase perovskites and study the influence of organic layer gap on the communication in between 2D perovskites quantum wells.

# Chapter 7 Conclusions and Future Work

This thesis investigates the confinement of inorganic-organic hybrid perovskite with inorganic nanoporous gallium nitride matrix and with polyaromatic hydrocarbon compounds.

In Chapter 4, we demonstrate a solution-processed method to infiltrate methylammonium lead bromide perovskite into the nanoporous GaN matrix. We show that by treating the nanoporous GaN matrix with APTES, MAPbBr<sub>3</sub>/GaN composite without perovskite capping layer can be achieved. We observe that the nanoporous GaN matrix can prevent light-induced degradation of MAPbBr<sub>3</sub> under continuous luminescence under 405 nm laser for more than five hours, and perovskite inside pores was stable after one-year exposure to the ambient environment. This result suggests that perovskite can be infiltrated into nanoporous GaN with a simple solution-processed method, and the GaN matrix can effectively prevent perovskite from degradation in the ambient environment. We expect this technique could be applied in building stable light emitting devices in the future.

Following the study in Chapter 4, we discuss the confinement effect of the nanoporous GaN on methylammonium lead bromide perovskite in Chapter 5. We show that the spatial confinement enhances the Coulomb interaction between charge carriers, lead to

a blue shift in photoluminescence comparing to the bulky MAPbBr<sub>3</sub>. As a result of the confinement, excitons become the dominant radiative recombination carriers in MAPbBr<sub>3</sub> nanocrystals at room temperature. The transient photoluminescence measurement demonstrates that the nanoporous GaN improves the radiative recombination rate of perovskites, while it also introduces defect states to perovskite nanocrystals. Therefore, the perovskite nanocrystal passivation approach needs to be explored in the future to achieve efficient light emission.

A general conclusion for Chapter 4 and Chapter 5 is that the MAPbBr<sub>3</sub>/GaN composite is well-suited to applications in light-emitting diodes. In the composite, nanoporous GaN enhances the stability of perovskite and introduces a confinement effect to perovskite. Meanwhile, perovskites make up for the less efficient emission of GaN in the green region. The infiltration process is simple and could be applied to other perovskites in the future. Therefore, it is possible to achieve a full spectrum emission with perovskite/GaN composition. In the future, it would be interesting to optimise the perovskite quality in pores and design perovskite/GaN composite lighting devices.

In Chapter 6, we demonstrate a solution-processed method to synthesis two-dimensional BPAIA lead iodide perovskite and two-dimensional DMAN lead iodide perovskite. We show that the steric effect between BPAIA molecules makes the structure of the synthesized perovskite unstable via the force-field modelling of the compound. The inorganic framework distortion caused by the steric effect of

anthracenes leads to a broadband emission of the BPAIA lead iodide perovskite. Therefore, in order to continue the research about the effect of functional organic materials on perovskite, we will change BPAIA to smaller functional compounds that can fit into the lead halide framework.

We also reveal that the DMAN lead iodide perovskite can be synthesized via the one-step deposition method, introducing a new perovskite to light emitting materials. In the future, it is also interesting to study the difference of charge transport ability for the naphthalene based RP phase and DJ phase perovskites to investigate the communication between 2D perovskite quantum wells.

To sum up, we investigate two approaches to achieve confinement of perovskite in this thesis, in situ perovskite nanocrystal growth in a nanoporous matrix and 2D perovskite synthesis. We show that perovskite/nanoporous GaN composite has the potential to be applied in stable light-emitting solid in the future due to the simple preparation method and respectable stability in the ambient atmosphere. We also synthesized a new two-dimensional perovskite in this study, broadening the 2D perovskite family. We hope our research could contribute to the fabrication of efficient perovskite light emitting diode in the future.



## Chapter 8 References

1. Global Warming vs. Climate Change | Resources – Climate Change: Vital Signs of the Planet. Available at: <https://climate.nasa.gov/resources/global-warming-vs-climate-change/>. (Accessed: 30th March 2021)
2. NASA GISS: NASA News & Feature Releases: 2020 Tied for Warmest Year on Record, NASA Analysis Shows. Available at: <https://www.giss.nasa.gov/research/news/20210114/>. (Accessed: 30th March 2021)
3. Ecological crisis - The Futures Centre. Available at: [https://www.thefuturescentre.org/trends/ecological-crisis/?gclid=Cj0KCQjwmIuDBhDXARIsAFITC\\_56Hi1gU989D-13AYi9NBIFViRxb7Vd4LOhijTapiWcfTeoJ3hzAZAaAqYNEALw\\_wcB](https://www.thefuturescentre.org/trends/ecological-crisis/?gclid=Cj0KCQjwmIuDBhDXARIsAFITC_56Hi1gU989D-13AYi9NBIFViRxb7Vd4LOhijTapiWcfTeoJ3hzAZAaAqYNEALw_wcB). (Accessed: 30th March 2021)
4. World Energy Outlook 2020 – Analysis - IEA. Available at: <https://www.iea.org/reports/world-energy-outlook-2020>. (Accessed: 30th March 2021)
5. Thejo Kalyani, N. & Dhoble, S. J. Organic light emitting diodes: Energy saving lighting technology - A review. *Renewable and Sustainable Energy Reviews* **16**, 2696–2723 (2012).
6. The coming revolution in LED lighting. Available at: <https://phys.org/news/2019-02-revolution.html>. (Accessed: 30th March 2021)
7. Zheludev, N. The life and times of the LED - A 100-year history. *Nature Photonics* **1**, 189–192 (2007).
8. Tan, Z. K. *et al.* Bright light-emitting diodes based on organometal halide perovskite. *Nat. Nanotechnol.* **9**, 687–692 (2014).

9. Kim, Y. H. *et al.* Comprehensive defect suppression in perovskite nanocrystals for high-efficiency light-emitting diodes. *Nat. Photonics* **15**, 148–155 (2021).
10. Mimura, T. Development of high electron mobility transistor. *Japanese J. Appl. Physics, Part 1 Regul. Pap. Short Notes Rev. Pap.* **44**, 8263–8268 (2005).
11. Veldhuis, S. A. *et al.* Perovskite Materials for Light-Emitting Diodes and Lasers. *Adv. Mater.* **28**, 6804–6834 (2016).
12. Chen, X., Lu, H., Yang, Y. & Beard, M. C. Excitonic Effects in Methylammonium Lead Halide Perovskites. *J. Phys. Chem. Lett.* **9**, 2595–2603 (2018).
13. Green, M. ~A. Solar cells: Operating principles, technology, and system applications. (1982).
14. Nelson, J. The physics of solar cells. (Imperial College Press, 2009).
15. Klingshirn, C. F. Electrons in a Periodic Crystal. (2012).
16. Even, J., Pedesseau, L., Jancu, J. M. & Katan, C. Importance of spin-orbit coupling in hybrid organic/inorganic perovskites for photovoltaic applications. *J. Phys. Chem. Lett.* **4**, 2999–3005 (2013).
17. Yu, P. Y. & Cardona, M. Electronic Band Structures. (2010).
18. Kittel, C. & McEuen, P. Introduction to solid state physics.(2004)
19. .Fox, M. Optical properties of solids. (Oxford University Press, 2012).
20. Griffiths, D. J. & Schroeter, D. F. *Introduction to Quantum Mechanics. Introduction to Quantum Mechanics* (Cambridge University Press, 2018).
21. Cohen-Tannoudji, C. (1933-). *et al.* Quantum mechanics. Vol. 1, Basic concepts, tools, and applications. (Wiley-VCH Verlag, 2020).
22. Oudar, J. L., Hulin, D., Migus, A., Antonetti, A. & Alexandre, F.

- Subpicosecond Spectral Hole Burning Due to Nonthermalized Photoexcited Carriers in GaAs. *Phys. Rev. Lett.* **55**, 2074–2077 (1985).
23. Hunsche, S., Heesel, H., Ewertz, A., Kurz, H. & Collet, J. H. Spectral-hole burning and carrier thermalization in GaAs at room temperature. *Phys. Rev. B* **48**, 17818–17826 (1993).
  24. Alfano, R. Semiconductors probed by ultrafast laser spectroscopy. (Academic Press, 1984).
  25. Clark, J. Intermolecular interactions in  $\pi$ -conjugated molecules : optical probes of chain conformation. (2007).
  26. Hot Carriers in Semiconductor Nanostructures. Hot Carriers in Semiconductor Nanostructures (Elsevier, 1992).
  27. Price, M. B. *et al.* Hot-carrier cooling and photoinduced refractive index changes in organic-inorganic lead halide perovskites. *Nat. Commun.* **6**, 1–8 (2015).
  28. Chen, K., Barker, A. J., Morgan, F. L. C., Halpert, J. E. & Hodgkiss, J. M. Effect of carrier thermalization dynamics on light emission and amplification in organometal halide perovskites. *J. Phys. Chem. Lett.* **6**, 153–158 (2015).
  29. Wright, A. D. *et al.* Electron-phonon coupling in hybrid lead halide perovskites. *Nat. Commun.* **7**, 1–9 (2016).
  30. Sendner, M. *et al.* Optical phonons in methylammonium lead halide perovskites and implications for charge transport. *Mater. Horizons* **3**, 613–620 (2016).
  31. Yang, Y. *et al.* Observation of a hot-phonon bottleneck in lead-iodide perovskites. *Nat. Photonics* **10**, 53–59 (2016).
  32. Rosenwaks, Y. *et al.* Hot-carrier cooling in GaAs: Quantum wells versus bulk.

- Phys. Rev. B* **48**, 14675–14678 (1993).
33. Herz, L. M. Charge-Carrier Dynamics in Organic-Inorganic Metal Halide Perovskites. *Annu. Rev. Phys. Chem.* **67**, 65–89 (2016).
  34. Varshni, Y. P. Band-to-Band Radiative Recombination in Groups IV, VI, and III–V Semiconductors (II). *Phys. status solidi* **20**, 9–36 (1967).
  35. Milot, R. L., Eperon, G. E., Snaith, H. J., Johnston, M. B. & Herz, L. M. Temperature-Dependent Charge-Carrier Dynamics in CH<sub>3</sub>NH<sub>3</sub>PbI<sub>3</sub> Perovskite Thin Films. *Adv. Funct. Mater.* **25**, 6218–6227 (2015).
  36. Grundmann, M. Recombination. Graduate Texts in Physics 309-344 (2010).
  37. Jellicoe, T. C. *et al.* Synthesis and Optical Properties of Lead-Free Cesium Tin Halide Perovskite Nanocrystals. *J. Am. Chem. Soc.* **138**, 2941–2944 (2016).
  38. Fang, H.-H. *et al.* Exciton Recombination in Formamidinium Lead Triiodide: Nanocrystals versus Thin Films. *Small* **13**, 1700673 (2017).
  39. Yakunin, S. *et al.* Low-threshold amplified spontaneous emission and lasing from colloidal nanocrystals of caesium lead halide perovskites. *Nat. Commun.* **6**, 1–9 (2015).
  40. Richter, J. M. *et al.* Enhancing photoluminescence yields in lead halide perovskites by photon recycling and light out-coupling. *Nat. Commun.* **7**, 1–8 (2016).
  41. De Mello, J. C., Wittmann, H. F. & Friend, R. H. An improved experimental determination of external photoluminescence quantum efficiency. *Adv. Mater.* **9**, 230–232 (1997).
  42. Snoke, D. W. Electronic Quasiparticles. *Solid State Physics* 86–156 (Cambridge University Press, 2020).
  43. Klingshirn, C. F. Optical Properties of Intrinsic Excitons in Bulk

- Semiconductors. in 309–362 (2012).
44. Klingshirn, C. F. Excitons, Biexcitons and Trions. (2012).
  45. Klingshirn, C. F. Optical Properties of Excitons in Structures of Reduced Dimensionality. (2012).
  46. Miller, D. A. B. & Miller, D. A. B. Optical Physics of Quantum Wells.
  47. Saparov, B. & Mitzi, D. B. Organic–Inorganic Perovskites: Structural Versatility for Functional Materials Design. *Chem. Rev.* **116**, 4558–4596 (2016).
  48. Efros, A. L. & Rosen, M. The Electronic Structure of Semiconductor Nanocrystals. *Annu. Rev. Mater. Sci.* **30**, 475–521 (2000).
  49. Klimov, V. I. Mechanisms for photogeneration and recombination of multiexcitons in semiconductor nanocrystals: Implications for lasing and solar energy conversion. *J. Phys. Chem. B* **110**, 16827–16845 (2006).
  50. Brus, L. E. Electron-electron and electron-hole interactions in small semiconductor crystallites: The size dependence of the lowest excited electronic state. *J. Chem. Phys.* **80**, 4403–4409 (1984).
  51. Wenk, H. & Bulakh, A. Minerals. (Cambridge university press, 2016).
  52. Perovskite Mineral Data. Available at:  
[http://webmineral.com/data/Perovskite.shtml#.YF\\_WF51KiUk](http://webmineral.com/data/Perovskite.shtml#.YF_WF51KiUk). (Accessed: 28th March 2021)
  53. Weber, D. CH<sub>3</sub>NH<sub>3</sub>PbX<sub>3</sub>, ein Pb(II)-System mit kubischer Perowskitstruktur. *Zeitschrift für Naturforsch. - Sect. B J. Chem. Sci.* **33**, 1443–1445 (1978).
  54. Kojima, A., Teshima, K., Shirai, Y. & Miyasaka, T. Organometal halide perovskites as visible-light sensitizers for photovoltaic cells. *J. Am. Chem. Soc.* **131**, 6050–6051 (2009).

55. Zhao, Y. & Zhu, K. Organic-inorganic hybrid lead halide perovskites for optoelectronic and electronic applications. *Chemical Society Reviews* **45**, 655–689 (2016).
56. Stranks, S. D. & Snaith, H. J. Metal-halide perovskites for photovoltaic and light-emitting devices. *Nature Nanotechnology* **10**, 391–402 (2015).
57. Yang, W. S. *et al.* Iodide management in formamidinium-lead-halide-based perovskite layers for efficient solar cells. *Science (80-. )*. **356**, 1376–1379 (2017).
58. Tan, Z. *et al.* Bright light-emitting diodes based on organometal halide perovskite. *Nat. Nanotechnol.* **9**, 687–692 (2014).
59. Ban, M. *et al.* Solution-processed perovskite light emitting diodes with efficiency exceeding 15% through additive-controlled nanostructure tailoring. *Nat. Commun.* **9**, 1–10 (2018).
60. Deschler, F. *et al.* High photoluminescence efficiency and optically pumped lasing in solution-processed mixed halide perovskite semiconductors. *J. Phys. Chem. Lett.* **5**, 1421–1426 (2014).
61. Zhu, H. *et al.* Lead halide perovskite nanowire lasers with low lasing thresholds and high quality factors. *Nat. Mater.* **14**, 636–642 (2015).
62. Sutherland, B. R. & Sargent, E. H. Perovskite photonic sources. *Nature Photonics* **10**, 295–302 (2016).
63. Mitzi, D. B., Chondroudis, K. & Kagan, C. R. Organic-inorganic electronics. *IBM J. Res. Dev.* **45**, 29–45 (2001).
64. Xu, X. *et al.* High-Performance Near-IR Photodetector Using Low-Bandgap MA<sub>0.5</sub>FA<sub>0.5</sub>Pb<sub>0.5</sub>Sn<sub>0.5</sub>I<sub>3</sub> Perovskite. *Adv. Funct. Mater.* **27**, 1701053 (2017).
65. Dou, L. *et al.* Solution-processed hybrid perovskite photodetectors with high

- detectivity. *Nat. Commun.* **5**, 1–6 (2014).
66. Yoo, J. J. *et al.* Efficient perovskite solar cells via improved carrier management. *Nature* **590**, 587–593 (2021).
67. Oxford PV hits new world record for solar cell | Oxford Photovoltaics. Available at: <https://www.oxfordpv.com/news/oxford-pv-hits-new-world-record-solar-cell>. (Accessed: 31st March 2021)
68. Goldschmidt, V. M. Krystallbau und chemische Zusammensetzung. *Berichte der Dtsch. Chem. Gesellschaft (A B Ser.)* **60**, 1263–1296 (1927).
69. Li, C. *et al.* Formability of  $ABX_3$  (X = F, Cl, Br, I) halide perovskites. *Acta Crystallogr. Sect. B Struct. Sci.* **64**, 702–707 (2008).
70. Hayashi, S., Aoki, R. & Nakamura, T. Metallic conductivity in perovskite-type compounds  $AMoO_3$  (A = Ba, Sr, Ca) down to 2.5K. *Mater. Res. Bull.* **14**, 409–413 (1979).
71. Smolin, S. Y., Scafetta, M. D., Guglietta, G. W., Baxter, J. B. & May, S. J. Ultrafast transient reflectance of epitaxial semiconducting perovskite thin films. *Appl. Phys. Lett.* **105**, 022103 (2014).
72. Jin, H., Rhim, S. H., Im, J. & Freeman, A. J. Topological oxide insulator in cubic perovskite structure. *Sci. Rep.* **3**, 1–5 (2013).
73. De Wolf, S. *et al.* Organometallic halide perovskites: Sharp optical absorption edge and its relation to photovoltaic performance. *J. Phys. Chem. Lett.* **5**, 1035–1039 (2014).
74. Stranks, S. D. *et al.* Electron-Hole Diffusion Lengths Exceeding 1 Micrometer in an Organometal Trihalide Perovskite Absorber. *Science (80-. )*. **342**, 341–344 (2013).
75. Wehrenfennig, C., Eperon, G. E., Johnston, M. B., Snaith, H. J. & Herz, L. M.

- High Charge Carrier Mobilities and Lifetimes in Organolead Trihalide Perovskites. *Adv. Mater.* **26**, 1584–1589 (2014).
76. Reynolds, D. C., Collins, T. C. & Sturge, M. Excitons: Their Properties and Uses. *Phys. Today* **36**, 73–75 (1983).
77. Knox, R. S. Introduction to Exciton Physics. *Collective Excitations in Solids* 183–245 (Springer US, 1983).
78. Amat, A. *et al.* Cation-induced band-gap tuning in organohalide perovskites: Interplay of spin-orbit coupling and octahedra tilting. *Nano Lett.* **14**, 3608–3616 (2014).
79. Röhm, H., Leonhard, T., Hoffmann, M. J. & Colmann, A. Ferroelectric domains in methylammonium lead iodide perovskite thin-films. *Energy Environ. Sci.* **10**, 950–955 (2017).
80. Ding, R. *et al.* High-performance piezoelectric nanogenerators composed of formamidinium lead halide perovskite nanoparticles and poly(vinylidene fluoride). *Nano Energy* **37**, 126–135 (2017).
81. Du, K. Z. *et al.* Two-Dimensional Lead(II) Halide-Based Hybrid Perovskites Templated by Acene Alkylamines: Crystal Structures, Optical Properties, and Piezoelectricity. *Inorg. Chem.* (2017).
82. Zhou, Y. *et al.* Giant photostriction in organic-inorganic lead halide perovskites. *Nat. Commun.* **7**, 1–8 (2016).
83. Herz, L. M. Charge-Carrier Dynamics in Organic-Inorganic Metal Halide Perovskites. *Annu. Rev. Phys. Chem.* (2016).
84. Saidaminov, M. I., Mohammed, O. F. & Bakr, O. M. Low-Dimensional- Networked Metal Halide Perovskites: The Next Big Thing. *ACS Energy Lett.* **2**, 889–896 (2017).

85. Park, N.-G. Perovskite Solar Cells: An Emerging Photovoltaic Technology. *Mater. Today* **18**, 1–8 (2014).
86. Veldhuis, S. A. *et al.* Perovskite Materials for Light-Emitting Diodes and Lasers. *Adv. Mater.* 6804–6834 (2016).
87. Chen, Y. *et al.* 2D Ruddlesden-Popper Perovskites for Optoelectronics. *Adv. Mater.* **30**, 1703487 (2018).
88. Velusamy, D. B. *et al.* 2D Organic–Inorganic Hybrid Thin Films for Flexible UV–Visible Photodetectors. *Adv. Funct. Mater.* **27**, (2017).
89. Tsai, H. *et al.* High-efficiency two-dimensional ruddlesden-popper perovskite solar cells. *Nature* **536**, 312–317 (2016).
90. Smith, I. C., Hoke, E. T., Solis-Ibarra, D., McGehee, M. D. & Karunadasa, H. I. A Layered Hybrid Perovskite Solar-Cell Absorber with Enhanced Moisture Stability. *Angew. Chemie - Int. Ed.* **53**, 11232–11235 (2014).
91. Stoumpos, C. C. *et al.* Ruddlesden-Popper Hybrid Lead Iodide Perovskite 2D Homologous Semiconductors. *Chem. Mater.* **28**, 2852–2867 (2016).
92. Stoumpos, C. C. *et al.* High Members of the 2D Ruddlesden-Popper Halide Perovskites: Synthesis, Optical Properties, and Solar Cells of  $(\text{CH}_3(\text{CH}_2)_3\text{NH}_3)_2(\text{CH}_3\text{NH}_3)_4\text{Pb}_5\text{I}_{16}$ . *Chem* **2**, 427–440 (2017).
93. Mao, L. *et al.* Hybrid Dion-Jacobson 2D Lead Iodide Perovskites. *J. Am. Chem. Soc.* **140**, 3775–3783 (2018).
94. Ruddlesden, S. N. & Popper, P. The compound  $\text{Sr}_3\text{Ti}_2\text{O}_7$  and its structure. *Acta Crystallogr.* **11**, 54–55 (1958).
95. Ruddlesden, S. N. & Popper, P. New compounds of the  $\text{K}_2\text{NIF}_4$  type. *Acta Crystallogr.* **10**, 538–539 (1957).
96. Dion, M., Ganne, M. & Tournoux, M. Nouvelles familles de phases

- MIMII<sub>2</sub>Nb<sub>3</sub>O<sub>10</sub> a feuillets 'perovskites'. *Mater. Res. Bull.* **16**, 1429–1435 (1981).
97. Jacobson, A. J., Johnson, J. W. & Lewandowski, J. T. Interlayer Chemistry between Thick Transition-Metal Oxide Layers: Synthesis and Intercalation Reactions of K[Ca<sub>2</sub>Na<sub>n-3</sub>Nb<sub>n</sub>O<sub>3+1</sub>] ( $3 \leq n \leq 7$ ). *Inorganic Chemistry* **24**, 3727–3729 (1985).
98. Mao, L., Stoumpos, C. C. & Kanatzidis, M. G. Two-Dimensional Hybrid Halide Perovskites: Principles and Promises. *J. Am. Chem. Soc.* **141**, 1171–1190 (2019).
99. Sichert, J. A. *et al.* Quantum Size Effect in Organometal Halide Perovskite Nanoplatelets. *Nano Lett.* **15**, 6521–6527 (2015).
100. Tyagi, P., Arveson, S. M. & Tisdale, W. A. Colloidal Organohalide Perovskite Nanoplatelets Exhibiting Quantum Confinement. *J. Phys. Chem. Lett.* **6**, 1911–1916 (2015).
101. Long, G. *et al.* Spin control in reduced-dimensional chiral perovskites. *Nat. Photonics* **12**, 528–533 (2018).
102. DeQuilettes, D. W. *et al.* Impact of microstructure on local carrier lifetime in perovskite solar cells. *Science* (80-. ). **348**, 683–686 (2015).
103. Wang, F., Bai, S., Tress, W., Hagfeldt, A. & Gao, F. Defects engineering for high-performance perovskite solar cells. *Flex. Electron.* **2**, 1–14 (2018).
104. Dmitri V. Talapin, *et al.* CdSe/CdS/ZnS and CdSe/ZnSe/ZnS Core–Shell–Shell Nanocrystals. *J. Phys. Chem. B* **108**, 18826–18831 (2004).
105. Zhang, F. *et al.* Brightly Luminescent and Color-Tunable Colloidal CH<sub>3</sub>NH<sub>3</sub>PbX<sub>3</sub> (X = Br, I, Cl) Quantum Dots: Potential Alternatives for Display

- Technology. *ACS Nano* **9**, 4533–4542 (2015).
106. Protesescu, L. *et al.* Nanocrystals of Cesium Lead Halide Perovskites ( $\text{CsPbX}_3$ , X = Cl, Br, and I): Novel Optoelectronic Materials Showing Bright Emission with Wide Color Gamut. *Nano Lett.* **15**, 3692–3696 (2015).
107. Murray, C. B., Norris, D. J. & Bawendi, M. G. Synthesis and characterization of nearly monodisperse CdE (E = sulfur, selenium, tellurium) semiconductor nanocrystallites. *J. Am. Chem. Soc.* **115**, 8706–8715 (2002).
108. Liu, L. & Risbud, S. H. Quantum-dot size-distribution analysis and precipitation stages in semiconductor doped glasses. *J. Appl. Phys.* **68**, 28 (1998).
109. Kojima, A., Ikegami, M., Teshima, K. & Miyasaka, T. Highly Luminescent Lead Bromide Perovskite Nanoparticles Synthesized with Porous Alumina Media.
110. Liu, S. *et al.* Precipitation and tunable emission of cesium lead halide perovskites ( $\text{CsPbX}_3$ , X = Br, I) QDs in borosilicate glass. *Ceram. Int.* **44**, 4496–4499 (2018).
111. Huang, X. *et al.* Reversible 3D laser printing of perovskite quantum dots inside a transparent medium. *Nat. Photonics* 2019 142 **14**, 82–88 (2019).
112. Protesescu, L., Yakunin, S., Nazarenko, O., Dirin, D. N. & Kovalenko, M. V. Low-Cost Synthesis of Highly Luminescent Colloidal Lead Halide Perovskite Nanocrystals by Wet Ball Milling. *ACS Appl. Nano Mater.* **1**, 1300–1308 (2018).
113. Hintermayr, V. A. *et al.* Tuning the Optical Properties of Perovskite Nanoplatelets through Composition and Thickness by Ligand-Assisted Exfoliation. *Adv. Mater.* **28**, 9478–9485 (2016).

114. Vybornyi, O., Yakunin, S. & Kovalenko, M. V. Polar-solvent-free colloidal synthesis of highly luminescent alkylammonium lead halide perovskite nanocrystals. *Nanoscale* **8**, 6278–6283 (2016).
115. Dey, A. *et al.* State of the Art and Prospects for Halide Perovskite Nanocrystals. *ACS Nano* **15**, 10775–10981 (2021).
116. Xu, K., Liu, C., Chung, W. J. & Heo, J. Optical properties of CdSe quantum dots in silicate glasses. *J. Non. Cryst. Solids* **356**, 2299–2301 (2010).
117. Huang, H., Bodnarchuk, M. I., Kershaw, S. V., Kovalenko, M. V. & Rogach, A. L. Lead Halide Perovskite Nanocrystals in the Research Spotlight: Stability and Defect Tolerance. *ACS Energy Lett.* **2**, 2071–2083 (2017).
118. Demchyshyn, S. *et al.* Confining metal-halide perovskites in nanoporous thin films. *Sci. Adv.* **3**, e1700738 (2017).
119. Wei, N. *et al.* Fabrication of an amine-modified ZIF-8@GO membrane for high-efficiency adsorption of copper ions. *New J. Chem.* **43**, 5603–5610 (2019).
120. Zhang, C. *et al.* Conversion of invisible metal-organic frameworks to luminescent perovskite nanocrystals for confidential information encryption and decryption. *Nat. Commun.* 2017 81 **8**, 1–9 (2017).
121. Zhang, Q. *et al.* Ceramic-like stable CsPbBr<sub>3</sub> nanocrystals encapsulated in silica derived from molecular sieve templates. *Nat. Commun.* 2020 111 **11**, 1–9 (2020).
122. Zhou, Q. *et al.* In Situ Fabrication of Halide Perovskite Nanocrystal-Embedded Polymer Composite Films with Enhanced Photoluminescence for Display Backlights. *Adv. Mater.* **28**, 9163–9168 (2016).
123. Malgras, V. *et al.* Observation of Quantum Confinement in Monodisperse

- Methylammonium Lead Halide Perovskite Nanocrystals Embedded in Mesoporous Silica. *J. Am. Chem. Soc.* **138**, 13874–13881 (2016).
124. Dirin, D. N. *et al.* Harnessing Defect-Tolerance at the Nanoscale: Highly Luminescent Lead Halide Perovskite Nanocrystals in Mesoporous Silica Matrixes. *Nano Lett.* **16**, 5866–5874 (2016).
125. Crouch, R. K., Debnam, W. J. & Fripp, A. L. Properties of GaN grown on sapphire substrates. *J. Mater. Sci. 1978 1311* **13**, 2358–2364 (2013).
126. Tong, Y. *et al.* Highly Luminescent Cesium Lead Halide Perovskite Nanocrystals with Tunable Composition and Thickness by Ultrasonication. *Angew. Chemie Int. Ed.* **55**, 13887–13892 (2016).
127. Gonzalez-Carrero, S., Galian, R. E. & Pérez-Prieto, J. Maximizing the emissive properties of  $\text{CH}_3\text{NH}_3\text{PbBr}_3$  perovskite nanoparticles. *J. Mater. Chem. A* **3**, 9187–9193 (2015).
128. Protesescu, L. *et al.* Nanocrystals of Cesium Lead Halide Perovskites ( $\text{CsPbX}_3$ , X = Cl, Br, and I): Novel Optoelectronic Materials Showing Bright Emission with Wide Color Gamut. *Nano Lett.* **15**, 3692–3696 (2015).
129. Droseros, N. *et al.* Origin of the Enhanced Photoluminescence Quantum Yield in  $\text{MAPbBr}_3$  Perovskite with Reduced Crystal Size. *ACS Energy Lett.* **3**, 1458–1466 (2018).
130. Becker, M. A. *et al.* Bright triplet excitons in caesium lead halide perovskites. *Nat. 2018 5537687* **553**, 189–193 (2018).
131. Makarov, N. S. *et al.* Spectral and Dynamical Properties of Single Excitons, Biexcitons, and Trions in Cesium–Lead-Halide Perovskite Quantum Dots. *Nano Lett.* **16**, 2349–2362 (2016).
132. Eperon, G. E., Jedlicka, E. & Ginger, D. S. Biexciton Auger Recombination

- Differs in Hybrid and Inorganic Halide Perovskite Quantum Dots. *J. Phys. Chem. Lett.* **9**, 104–109 (2017).
133. Manser, J. S. & Kamat, P. V. Band filling with free charge carriers in organometal halide perovskites. *Nat. Photonics* 2014 89 **8**, 737–743 (2014).
134. Yang, B. & Han, K. Charge-Carrier Dynamics of Lead-Free Halide Perovskite Nanocrystals. *Acc. Chem. Res.* **52**, 3188–3198 (2019).
135. Leijtens, T. *et al.* Towards enabling stable lead halide perovskite solar cells; interplay between structural, environmental, and thermal stability. *J. Mater. Chem. A* **5**, 11483–11500 (2017).
136. Vincent, B. R., Robertson, K. N., Cameron, T. S. & Knop, O. Alkylammonium lead halides. Part 1. Isolated  $\text{PbI}_6^{4-}$  ions in  $(\text{CH}_3\text{NH}_3)_4\text{PbI}_6 \cdot 2\text{H}_2\text{O}$ .
137. Li, Y. *et al.* Bifunctional Organic Spacers for Formamidinium-Based Hybrid Dion-Jacobson Two-Dimensional Perovskite Solar Cells. *Nano Lett.* **19**, 150–157 (2019).
138. Lu, D. *et al.* Thiophene-Based Two-Dimensional Dion-Jacobson Perovskite Solar Cells with over 15% Efficiency. *J. Am. Chem. Soc.* **142**, 11114–11122 (2020).
139. Chen, Y. *et al.* Tailoring Organic Cation of 2D Air-Stable Organometal Halide Perovskites for Highly Efficient Planar Solar Cells. *Adv. Energy Mater.* **7**, 1700162 (2017).
140. Lermer, C. *et al.* Toward Fluorinated Spacers for MAPI-Derived Hybrid Perovskites: Synthesis, Characterization, and Phase Transitions of  $(\text{FC}_2\text{H}_4\text{NH}_3)_2\text{PbCl}_4$ . *Chem. Mater.* **28**, 6560–6566 (2016).
141. Cao, D. H. *et al.* Thin Films and Solar Cells Based on Semiconducting Two-Dimensional Ruddlesden–Popper  $(\text{CH}_3(\text{CH}_2)_3\text{NH}_3)_2(\text{CH}_3\text{NH}_3)_{n-1}\text{Sn}_n\text{I}_{3n+1}$

- Perovskites. *ACS Energy Lett.* **2**, 982–990 (2017).
142. Burschka, J. *et al.* Sequential deposition as a route to high-performance perovskite-sensitized solar cells. *Nature* **499**, 316–319 (2013).
143. Andaji-Garmaroudi, Z., Anaya, M., Pearson, A. J. & Stranks, S. D. Photobrightening in Lead Halide Perovskites: Observations, Mechanisms, and Future Potential. *Adv. Energy Mater.* **10**, 1903109 (2020).
144. Motti, S. G. *et al.* Controlling competing photochemical reactions stabilizes perovskite solar cells. *Nat. Photonics* 2019 138 **13**, 532–539 (2019).
145. Godding, J. S. W. *et al.* Oxidative Passivation of Metal Halide Perovskites. *Joule* **3**, 2716–2731 (2019).
146. Osherov, A. *et al.* The Impact of Phase Retention on the Structural and Optoelectronic Properties of Metal Halide Perovskites. *Adv. Mater.* **28**, 10757–10763 (2016).
147. Meggiolaro, D., Mosconi, E. & Angelis, F. De. Mechanism of Reversible Trap Passivation by Molecular Oxygen in Lead-Halide Perovskites. *ACS Energy Lett.* **2**, 2794–2798 (2017).
148. Stranks, S. D. *et al.* Recombination Kinetics in Organic-Inorganic Perovskites: Excitons, Free Charge, and Subgap States. *Phys. Rev. Appl.* **2**, 034007 (2014).
149. Gottesman, R. *et al.* Photoinduced Reversible Structural Transformations in Free-Standing CH<sub>3</sub>NH<sub>3</sub>PbI<sub>3</sub> Perovskite Films. *J. Phys. Chem. Lett.* **6**, 2332–2338 (2015).
150. Anaya, M., Galisteo-López, J. F., Calvo, M. E., Espinós, J. P. & Míguez, H. Origin of Light-Induced Photophysical Effects in Organic Metal Halide Perovskites in the Presence of Oxygen. *J. Phys. Chem. Lett.* **9**, 3891–3896 (2018).

151. deQuilettes, D. W. *et al.* Photo-induced halide redistribution in organic–inorganic perovskite films. *Nat. Commun.* **2016 7** **1**, 1–9 (2016).
152. Tian, Y. *et al.* Enhanced Organo-Metal Halide Perovskite Photoluminescence from Nanosized Defect-Free Crystallites and Emitting Sites. *J. Phys. Chem. Lett.* **6**, 4171–4177 (2015).
153. Rinke, P. *et al.* Band gap and band parameters of InN and GaN from quasiparticle energy calculations based on exact-exchange density-functional theory. *Appl. Phys. Lett.* **89**, 161919 (2006).
154. Hassan, A., Savaria, Y. & Sawan, M. GaN Integration Technology, an Ideal Candidate for High-Temperature Applications: A Review. *IEEE Access* **6**, 78790–78802 (2018).
155. Amano, H. *et al.* The 2018 GaN power electronics roadmap. *Journal of Physics D: Applied Physics* **51**, 163001 (2018).
156. Park, J.-S., Kim, J. K., Cho, J. & Seong, T.-Y. Review—Group III-Nitride-Based Ultraviolet Light-Emitting Diodes: Ways of Increasing External Quantum Efficiency. *ECS J. Solid State Sci. Technol.* **6**, Q42–Q52 (2017).
157. Nakamura, S., Senoh, M., Iwasa, N. & Nagahama, S. I. High-brightness InGaN blue, green and yellow light-emitting diodes with quantum well structures. *Jpn. J. Appl. Phys.* **34**, L797–L799 (1995).
158. Arbouche, O., Belgoumène, B., Soudini, B. & Driz, M. First principles study of the relative stability and the electronic properties of GaN. *Comput. Mater. Sci.* **47**, 432–438 (2009).
159. Xia, H., Xia, Q. & Ruoff, A. L. High-pressure structure of gallium nitride: Wurtzite-to-rocksalt phase transition. *PHYSICAL REVIEW* **8**,
160. Zhu, T. *et al.* Wafer-scale Fabrication of Non-Polar Mesoporous GaN

- Distributed Bragg Reflectors via Electrochemical Porosification. *Sci. Rep.* **7**, 1–8 (2017).
161. Zhang, C. *et al.* Mesoporous GaN for Photonic Engineering-Highly Reflective GaN Mirrors as an Example. *ACS Photonics* **2**, 980–986 (2015).
162. Soh, C. B. *et al.* Nanopore morphology in porous GaN template and its effect on the LEDs emission. *J. Phys. D. Appl. Phys.* **46**, 365102 (2013).
163. Tseng, W. J., Van Dorp, D. H., Lieten, R. R., Vereecken, P. M. & Borghs, G. Anodic etching of n-GaN epilayer into porous GaN and its photoelectrochemical properties. *J. Phys. Chem. C* **118**, 29492–29498 (2014).
164. Monemar, B. Chapter 11 Optical Properties of GaN. *Semicond. Semimetals* **50**, 305–368 (1997).
165. Gong, J. *et al.* Study on the band alignment of GaN/CH<sub>3</sub>NH<sub>3</sub>PbBr<sub>3</sub> heterojunction by x-ray photoelectron spectroscopy. *Appl. Phys. Lett.* **111**, 122103 (2017).
166. Jain, S. C., Willander, M., Narayan, J. & Van Overstraeten, R. III-nitrides: Growth, characterization, and properties. *Journal of Applied Physics* **87**, 965–1006 (2000).
167. Li, G. *et al.* Nature and elimination of yellow-band luminescence and donor-acceptor emission of undoped GaN. *Appl. Phys. Lett* **74**, 2821 (1999).
168. Reshchikov, M. A. & Morkoç, H. Luminescence properties of defects in GaN. *J. Appl. Phys.* **97**, 61301 (2005).
169. Gil, B. Group III nitride semiconductor compounds. (Clarendon Press, 2008).
170. Woolfson, M. M. An Introduction to X-ray Crystallography. (Cambridge University Press, 1997).
171. Watt, I. M. The Principles and Practice of Electron Microscopy. (Cambridge

- University Press, 1997).
172. Goldstein, J. I., Yakowitz, H. & Newbury, D. E. Introduction. *Practical Scanning Electron Microscopy* 1–19 (Springer US, 1975).
173. Swinehart, D. F. The Beer-Lambert law. *Journal of Chemical Education* **39**, 333–335 (1962).
174. Loiudice, A., Saris, S., Oveisi, E., Alexander, D. T. L. & Buonsanti, R. CsPbBr<sub>3</sub> QD/AlO<sub>x</sub> Inorganic Nanocomposites with Exceptional Stability in Water, Light, and Heat. *Angew. Chemie Int. Ed.* **56**, 10696–10701 (2017).
175. Rubino, A., Calìo, L., García-Bennett, A., Calvo, M. E. & Míguez, H. Mesoporous Matrices as Hosts for Metal Halide Perovskite Nanocrystals. *Adv. Opt. Mater.* **8**, 1901868 (2020).
176. Neugebauer, J. & Van de Walle, C. G. Gallium vacancies and the yellow luminescence in GaN. *Appl. Phys. Lett.* **69**, 503–505 (1996).
177. Sánchez, F. J. *et al.* Yellow luminescence in Mg-doped GaN. *MRS Internet J. Nitride Semicond. Res.* **2**, (1997).
178. Yan-Ping, S. *et al.* Mechanism of Yellow Luminescence in GaN Related content Effect of Mg Doping on the Photoluminescence of GaN:Mg Films by Radio-Frequency Plasma-Assisted Molecular Beam Epitaxy Defect-related luminescence of Mg-doped n-GaN grown by hydride vapour-phase epitaxy-Cathodoluminescence of Yellow and Blue Luminescence in Undoped Semi-insulating. *Japanese Journal of Applied Physics To* **19**, (1980).
179. Ogino, T. & Aoki, M. Mechanism of yellow luminescence in GaN. *Jpn. J. Appl. Phys.* **19**, 2395–2405 (1980).
180. Julkarnain, M., Kamata, N., Fukuda, T. & Arakawa, Y. Yellow luminescence band in undoped GaN revealed by two-wavelength excited photoluminescence.

- Opt. Mater. (Amst)*. **60**, 481–486 (2016).
181. Yan, K. *et al.* Hybrid Halide Perovskite Solar Cell Precursors: Colloidal Chemistry and Coordination Engineering behind Device Processing for High Efficiency. *J. Am. Chem. Soc.* **137**, 4460–4468 (2015).
182. Shallcross, R. C., Olthof, S., Meerholz, K. & Armstrong, N. R. Impact of Titanium Dioxide Surface Defects on the Interfacial Composition and Energetics of Evaporated Perovskite Active Layers. *ACS Appl. Mater. Interfaces* **11**, 16 (2019).
183. Sun, C. *et al.* Efficient and Stable White LEDs with Silica-Coated Inorganic Perovskite Quantum Dots. *Adv. Mater.* **28**, 10088–10094 (2016).
184. Arranz, A. *et al.* Influence of surface hydroxylation on 3-aminopropyltriethoxysilane growth mode during chemical functionalization of GaN surfaces: An angle-resolved X-ray photoelectron spectroscopy study. *Langmuir* **24**, 8667–8671 (2008).
185. Baur, B. *et al.* Chemical functionalization of GaN and AlN surfaces. *Appl. Phys. Lett.* **87**, 1–3 (2005).
186. Isasi, J., Arévalo, P., Martín, E. & Martín-Hernández, F. Preparation and study of silica and APTES–silica-modified NiFe<sub>2</sub>O<sub>4</sub> nanocomposites for removal of Cu<sup>2+</sup> and Zn<sup>2+</sup> ions from aqueous solutions. *J. Sol-Gel Sci. Technol.* **91**, 596–610 (2019).
187. Luo, B. *et al.* Organolead Halide Perovskite Nanocrystals: Branched Capping Ligands Control Crystal Size and Stability. *Angew. Chemie Int. Ed.* **55**, 8864–8868 (2016).
188. Han, S. *et al.* Highly Efficient and Flexible Photosensors with GaN Nanowires Horizontally Embedded in a Graphene Sandwich Channel. *ACS Appl. Mater. Interfaces* **10**, 38173–38182 (2018).

189. DeQuilettes, D. W. *et al.* Photo-induced halide redistribution in organic-inorganic perovskite films. *Nat. Commun.* **7**, 1–9 (2016).
190. Anaya, M., Galisteo-López, J. F., Calvo, M. E., Espinós, J. P. & Míguez, H. Origin of Light-Induced Photophysical Effects in Organic Metal Halide Perovskites in the Presence of Oxygen. *J. Phys. Chem. Lett.* **9**, 3891–3896 (2018).
191. Anaya, M., Galisteo-López, J. F., Calvo, M. E., Espinós, J. P. & Míguez, H. Origin of Light-Induced Photophysical Effects in Organic Metal Halide Perovskites in the Presence of Oxygen. *J. Phys. Chem. Lett.* **9**, 3891–3896 (2018).
192. Huang, H. *et al.* Emulsion Synthesis of Size-Tunable CH<sub>3</sub>NH<sub>3</sub>PbBr<sub>3</sub> Quantum Dots: An Alternative Route toward Efficient Light-Emitting Diodes. *ACS Appl. Mater. Interfaces* **7**, 28128–28133 (2015).
193. Schmidt, L. C. *et al.* Nontemplate synthesis of CH<sub>3</sub>NH<sub>3</sub>PbBr<sub>3</sub> perovskite nanoparticles. *J. Am. Chem. Soc.* **136**, 850–853 (2014).
194. Niu, Y. *et al.* Aggregation-Induced Emission Features of Organometal Halide Perovskites and Their Fluorescence Probe Applications. *Adv. Opt. Mater.* **3**, 112–119 (2015).
195. Hassan, Y. *et al.* Structure-Tuned Lead Halide Perovskite Nanocrystals. *Adv. Mater.* **28**, 566–573 (2016).
196. Anaya, M. *et al.* Strong Quantum Confinement and Fast Photoemission Activation in CH<sub>3</sub>NH<sub>3</sub>PbI<sub>3</sub> Perovskite Nanocrystals Grown within Periodically Mesoporous Films. *Adv. Opt. Mater.* **5**, 1601087 (2017).
197. Lee, H. J. *et al.* A Facile Preparative Route of Nanoscale Perovskites over Mesoporous Metal Oxide Films and Their Applications to Photosensitizers and Light Emitters. *Adv. Funct. Mater.* **28**, 1803801 (2018).

198. Gong, J. *et al.* Study on the band alignment of GaN/CH<sub>3</sub>NH<sub>3</sub>PbBr<sub>3</sub> heterojunction by x-ray photoelectron spectroscopy. *Appl. Phys. Lett.* **111**, 122103 (2017).
199. Wang, Q. *et al.* Quantum confinement effect and exciton binding energy of layered perovskite nanoplatelets *Adv.* **8**, 25108 (2018).
200. Lim, K. T. P. *et al.* Encapsulation of methylammonium lead bromide perovskite in nanoporous GaN. *APL Mater.* **7**, 021107 (2019).
201. Stavrakas, C. *et al.* Visualizing Buried Local Carrier Diffusion in Halide Perovskite Crystals via Two-Photon Microscopy. *ACS Energy Lett.* **5**, 117–123 (2020).
202. Ravi, V. K., Swarnkar, A., Chakraborty, R. & Nag, A. Excellent green but less impressive blue luminescence from CsPbBr<sub>3</sub> perovskite nanocubes and nanoplatelets. *Nanotechnology* **27**, 325708 (2016).
203. Gonzalez-Carrero, S., Galian, R. E. & Pérez-Prieto, J. Maximizing the emissive properties of CH<sub>3</sub>NH<sub>3</sub>PbBr<sub>3</sub> perovskite nanoparticles. *J. Mater. Chem. A* **3**, 9187–9193 (2015).
204. Zheng, K. *et al.* Trap States and Their Dynamics in Organometal Halide Perovskite Nanoparticles and Bulk Crystals. *J. Phys. Chem. C* **120**, 3077–3084 (2016).
205. Schmidt, T., Lischka, K. & Zulehner, W. Excitation-power dependence of the near-band-edge photoluminescence of semiconductors. *PHYSICAL REVIEW* **8**, (1991).
206. Stoumpos, C. C. & Kanatzidis, M. G. The Renaissance of Halide Perovskites and Their Evolution as Emerging Semiconductors. *Acc. Chem. Res.* **48**, 2791–2802 (2015).

- 
207. Stranks, S. D. & Snaith, H. J. Metal-halide perovskites for photovoltaic and light-emitting devices. *Nature Nanotechnology* **10**, 391–402 (2015).
208. Xu, Z., Chen, M. & Liu, S. F. First-Principles Study of Enhanced Out-of-Plane Transport Properties and Stability in Dion–Jacobson Two-Dimensional Perovskite Semiconductors for High-Performance Solar Cell Applications. *J. Phys. Chem. Lett.* **10**, 3670–3675 (2019).
209. Mitzi, D. B., Chondroudis, K. & Kagan, C. R. Design, Structure, and Optical Properties of Organic–Inorganic Perovskites Containing an Oligothiophene Chromophore. *Inorg. Chem.* **38**, 6246–6256 (1999).
210. Mitzi, D. B., Dimitrakopoulos, C. D. & Kosbar, L. L. Structurally tailored organic-inorganic perovskites: Optical properties and solution-processed channel materials for thin-film transistors. *Chem. Mater.* **13**, 3728–3740 (2001).
211. Omary, M. A. & Patterson, H. H. Luminescence, Theory in Encyclopedia of Spectroscopy and Spectrometry 636–653 (Elsevier, 2016).
212. Du, K. *et al.* Two-Dimensional Lead(II) Halide-Based Hybrid Perovskites Templated by Acene Alkylamines: Crystal Structures, Optical Properties, and Piezoelectricity. *Inorg. Chem.* **56**, 9291–9302 (2017).
213. Dohner, E. R., Hoke, E. T. & Karunadasa, H. I. Self-assembly of broadband white-light emitters. *J. Am. Chem. Soc.* **136**, 1718–1721 (2014).
214. Dohner, E. R., Jaffe, A., Bradshaw, L. R. & Karunadasa, H. I. Intrinsic white-light emission from layered hybrid perovskites. *J. Am. Chem. Soc.* **136**, 13154–13157 (2014).
215. Mao, L., Wu, Y., Stoumpos, C. C., Wasielewski, M. R. & Kanatzidis, M. G. White-Light Emission and Structural Distortion in New Corrugated Two-Dimensional Lead Bromide Perovskites. *J. Am. Chem. Soc.* **139**, 5210–5215

(2017).